Multi-material processing of metallic components by direct additive manufacturing methods: technologies, scientific insights, and industrial applications

Multi-material processing of metallic components by direct additive manufacturing methods: technologies, scientific insights, and industrial applications

OPEN ACCESS
IMMT | IOP Publishing
International Journal of Extreme Manufacturing
Int. J. Extrem. Manuf. **8** (2026) 042004 (52pp)
https://doi.org/10.1088/2631-7990/ae5295

Topical Review

Multi-material processing of metallic components by direct additive manufacturing methods: technologies, scientific insights, and industrial applications

Reza Ghanavati[1,3], Mohammad Hossein Mosallanejad[1,3], Amir Behjat[1,3], Mohammad Taghian[1,3], Paolo Fino[2,3], Luca Iuliano[1,3] and Abdollah Saboori[1,3,*]

[1] Department of Management and Production Engineering (DIGEP), Politecnico di Torino, Corso Duca degli Abruzzi 24, 10129 Torino, Italy
[2] Department of Applied Science and Technology (DISAT), Politecnico di Torino, Corso Duca degli Abruzzi 24, 10129 Torino, Italy
[3] Integrated Additive Manufacturing Center (IAM@PoliTo), Politecnico di Torino, Corso Castelfidardo 51, 10129 Torino, Italy

E-mail: abdollah.saboori@polito.it

Received 8 July 2025, revised 16 October 2025
Accepted for publication 15 March 2026
Published 2 April 2026

Abstract

Inspired by the surrounding natural patterns, multi-material structures play a significant and integral role in contemporary life because of their multi-functionality and tailored site-specific properties for diverse service requirements. Although conventional manufacturing methods have brought the primary concept of multi-materials into the engineering world, additive manufacturing (AM) technology has overcome long-standing limitations and has significantly flourished in its research and development. Its layer-wise mechanism provides a unique opportunity to integrate highly flexible materials design and manufacturing of highly complex geometries. Over the past decade, many attempts have been made to develop multi-material additive manufacturing (MM-AM) as an innovative and reliable solution for critical materials. Therefore, this review comprehensively covers and criticizes recent advances in processing multi-material metallic components through direct AM technologies. By clarifying the dimensions of the multi-material concept, different direct metal AM processes for

* Author to whom any correspondence should be addressed.

multi-material fabrication are described in this context. Then, case studies on MM-AM are classified based on AM technology and discussed, focusing on the most recent and notable research. Furthermore, practical applications of MM-AM in various sectors, such as aerospace, automotive, biomedical, and electronics, are addressed. Lastly, a perspective and a summary are provided to offer insights into the current status and future directions of this field.

Keywords: multi-material, additive manufacturing, functionally graded materials, powder bed fusion, directed energy deposition

Abbreviations

MM	Multi-material
AM	Additive manufacturing
MM-AM	Multi-material additive manufacturing
DED	Directed energy deposition
PBF	Powder bed fusion
CAD	Computer-aided design
FGMs	Functionally graded materials
3D	Three-dimensional
2D	Two-dimensional
BJ	Binder jetting
ADAM	Atomic diffusion additive manufacturing
L-PBF	Laser powder bed fusion
EB-PBF	Electron beam powder bed fusion
L-DED	Laser directed energy deposition
EB-DED	Electron beam directed energy deposition
WA-DED	Wire arc directed energy deposition
IN718	Inconel 718
SS316L	Stainless steel 316L
IN625	Inconel 625
SS304L	Stainless steel 304L
CET	Columnar to equiaxed transition
HTs	Heat treatments
AB	As-built
TEM	Transmission electron microscopy
AD	As-deposited
DIC	Digital image correlation
UTS	Ultimate tensile strength
DAH	Direct age hardening
HF	Hydrofluoric acid
XRD	X-ray diffraction
FCC	Face-centered cubic
BCC	Body-centered cubic
EBSD	Electron backscatter diffraction
IMCs	Intermetallic compounds
IQ	Image quality
IPF	Inverse pole figure
KAM	Kernel average misorientation
RT	Room temperature
Q+T	Quenched and tempered
PHT	Post-heat treatment
LME	Liquid metal embrittlement
LPS	Liquid phase separation
EIS	Electrochemical impedance spectroscopy
MS	Maraging steel
XCT	X-ray computed tomography
BD	Building direction
FL	Fully lamellar
NL	Nearly lamellar
SEM	Scanning electron microscopy
EPMA	Electron probe microanalysis
HIP	Hot isostatic pressing
ODS	Oxide dispersion strengthened
NASA	National Aeronautics and Space Administration
ESA	European Space Agency
CTE	Coefficient of thermal expansion
IR	Infrared
CALPHAD	Calculation of phase diagram
ML	Machine learning
CBA	Cost–benefit Analysis
SPD	Selective powder deposition
TRL	Technology readiness level
ROI	Return on investment

1. Introduction

Multi-material (MM) components are composed of multiple materials that are physically distributed within the part to increase their functionality[1,2]. This approach integrates the structures, properties, and functions associated with various materials to achieve site-specific properties in a single component[3,4]. Moreover, the MM concept can be defined as an engineering response to the need for components with superior performance under working conditions requiring multiple properties. MM structures can offer end-users from different sectors, such as aerospace, biomedical, automotive, and moulding industries, innovative structures with improved performance[5]. For instance, MM structures can be tailored to provide high thermal resistance as well as acceptable mechanical properties at low temperatures, as required in aerospace[6]. Additionally, these structures can have applications in the medical sector[7], particularly where orthopaedic implants with stiffness comparable to that of human bones, as well as

superior wear and corrosion resistance, are required[8]. It is reported that metallic MM components with simple designs can be conventionally produced through various methods, such as powder metallurgy, rolling, welding, chemical vapour deposition, and diffusion bonding[9,10]. However, these conventional methods cannot be employed to manufacture MM structures with complex designs and geometries[8,11].

For this reason, advanced techniques such as additive manufacturing (AM) should be adopted to integrate multiple materials and functionalities into a single component with a complex design[9,10]. AM is a rapidly increasing manufacturing method described as the layer-wise manufacturing of components based on the computer-aided design (CAD) models, with its most prominent feature being the ability to produce highly complex geometries[12]. AM can also be used to process a wide range of materials, including ceramics, polymers, and metals[12–14]. In the case of metallic materials, AM methods cover a wide variety of compositions, including alloys of aluminum[15–17], steel[18–20], titanium[21–24], zirconium[25], zinc[26–28], superalloys, and their combination, increasing the flexibility of the method. Additionally, non-metallics can be added to metallic powder feedstock to produce metal matrix composites with specific properties via AM techniques[29,30]. Numerous researchers have attempted to further alleviate the limitations associated with processing single material components to enhance the capabilities of metal AM technologies in different industrial sectors[31–35]. These research lines are motivated by the need for products with desired functional properties in target regions while maintaining conventional, cost-effective production in other parts[7]. As a result, direct AM processes, which deal with part production through a single-step AM process, are utilized to physically deposit more than one type of metallic material on the building platform or onto a targeted area of a given component. This approach adds more complexity and functionality to already developed components and offers potential applications for the mentioned AM methods.

Compared with the previous literature, the current study provides a targeted and comparative investigation of the utilization of L-PBF and DED for multi-material metallic additive manufacturing and functionally graded structures. While Schneck et al. conducted an in-depth review of MM manufacturing limited to PBF processes, focusing on powder delivery mechanisms and process maturity levels, our review broadens this scope by systematically comparing PBF and DED approaches in terms of process flexibility, interface control, and industrial applicability[36]. Verma et al. provided a comprehensive and useful review of multiplicity in MM-AM, covering various materials (polymers, metals, ceramics) and hybrid AM processes; however, our work provides a deeper and more technical synthesis of metallic multi-material AM, emphasizing the unique process–structure–property relationships relevant to PBF and DED[37]. Furthermore, whereas Zheng et al. presented a conceptual vision of MM-AM's future, emphasizing multi-functional architectures and design opportunities, our review adds to this perspective by critically assessing the current technological state, practical challenges, failure mechanisms, and the relative readiness of PBF and DED for industrial adoption[38].

This review addresses the challenges and opportunities arising from integrating multiple materials in additive manufacturing, focusing on advancements in material science, design considerations, and manufacturing processes. Various forms of multi-material designs, such as functionally graded materials (FGMs), bimetal, layered, and crossed lamellar structures, along with different material combinations like metal–metal and ceramic–metal, are discussed in depth (Section 4). Additionally, the current state of multi-material processing in additive manufacturing and its potential impact on various industries, including aerospace, automotive, electronics, and healthcare, are critically analyzed (Section 5). This review also addresses the limitations and future research directions in the field, shedding light on the path forward for the development and widespread adoption of multi-material additive manufacturing technologies (Section 6).

2. Multi-materials

The natural world highlights highly efficient designs and principles that utilize specific combinations of materials and structures tailored for different purposes[39–43]. Three-dimensional, repeating microscale structures are common in nature, such as in the cellular arrays found in living tissue[44,45]. These structures can also be intentionally created in smart materials. Conversely, human-created objects often have simpler designs made from single materials and may not be fully customized for specific applications owing to traditional design and manufacturing limitations[41]. Moreover, there are multiple methods for achieving exceptional and adjustable mechanical properties, such as replicating the intricate structures found in natural materials. One approach involves creating micro-architected, multi-material structures with a unique microstructure, incorporating two or more material phases, and drawing inspiration from biological materials such as bone and nacre (Figure 1(a))[46]. Another method emulates biological materials through lattice materials, where the porosity distribution is engineered to achieve superior mechanical properties[47]. In terms of compositions, multi-materials can be categorized into various types, including metal−polymer composites, ceramic−polymer composites[47–49], and metal−ceramic composites[50–52]. Research has been devoted to various multi-material types with unique properties and applications based on their composition and structure. These works include the development of a platform designed to create MM structures for scaffolds and various other applications[45], the construction of a NiTi multi-material cascade electrocaloric cooling device (Figure 1(b))[53], the development of bioinspired functionally graded materials (FGMs) to investigate continuous and hard−soft composites deformation and fracture behaviours[54], and the fabrication of mechanically interlocked metal−organic microstructures (Figure 1(c))[55]. Other studies have also investigated nature-inspired multi-material fabrication concepts for applications such as 3D denture

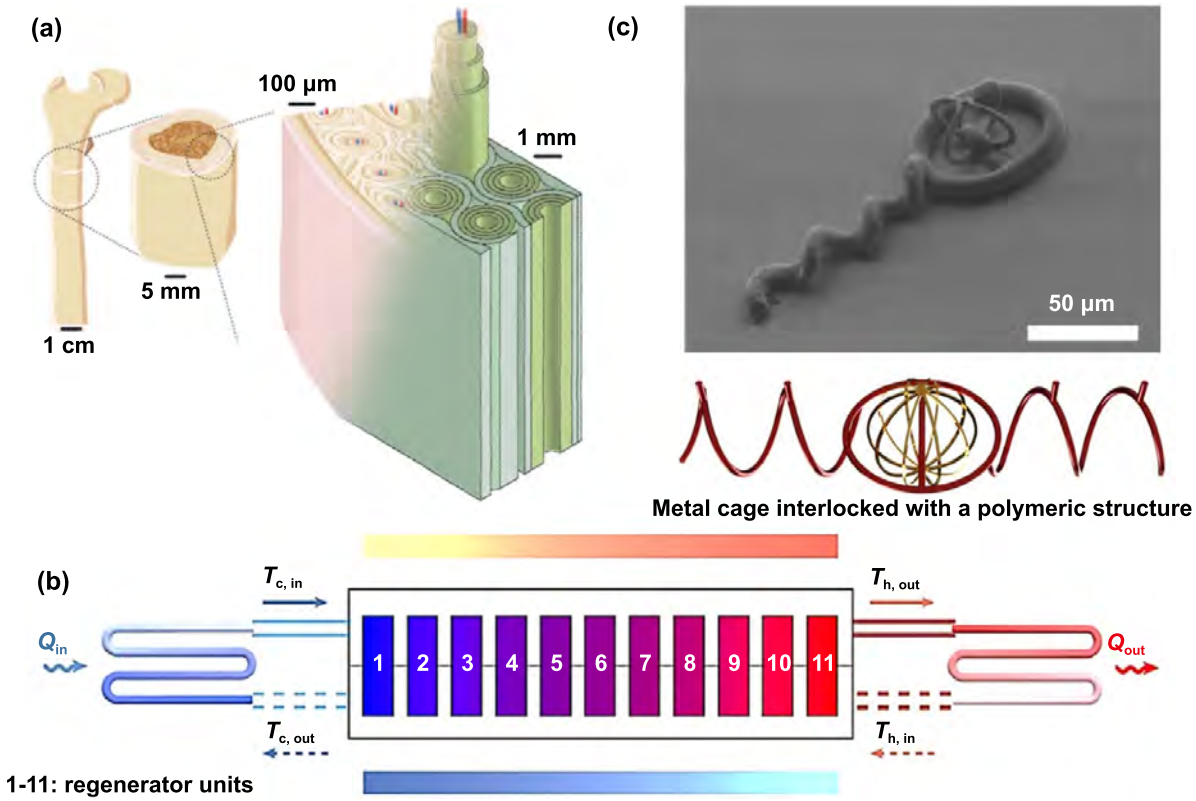

Figure 1. Examples of multi-material structures. (a) Hierarchical levels of bone showing a femur cross section compared with a bio-inspired carbon and glass fibers and epoxy resin composite. Reproduced from[46]. CC BY 4.0. (b) a multi-material regenerator consisting of 11 cascades of NiTi units with different phase transition temperatures. Reproduced from[53], with permission from Springer Nature. and (c) SEM and schematic illustration of 3D mechanically interlocked structures containing metallic Fe and PDMS components. Reproduced from[55]. CC BY 4.0.

printing[41], energy harvesting[56–58], sensors[59,60], and lightweight automotive parts[61,62].

Integrating multiple materials within a single manufacturing process is promising. However, this advantage is further pronounced when AM methods are employed to produce MM components. Consequently, the most profound advantage of MM-AM lies in its ability to generate property-specific regions within a single manufacturing operation. This capability eliminates the need for multiple manufacturing steps, thereby improving the production process and enhancing efficiency[38,63]. Therefore, the ability to tailor material properties at specific locations within a part via AM methods not only enhances the component performance but also opens new possibilities for designing and applying complex structures[64]. To achieve this goal, however, MM-AM strategically deposits different material components at specific locations to develop intentionally heterogeneous structures, unlike the conventional AM method, which mixes materials to create homogeneous composites. Considering this critical requirement, ensuring compatibility and effective bonding between these materials poses a significant challenge during the MM-AM process and subsequent post-processing steps. Additionally, optimizing material delivery and utilization efficiency throughout the entire process remains a critical issue[65,66].

3. Metal additive manufacturing

Metal AM, an emergent technology, has attracted substantial attention across various sectors, notably the automotive, aerospace, and biomedical industries[13]. In the broader context, metal AM processes can be classified into direct and indirect types. Direct AM produces a net-shaped component directly from a CAD model. Notably, in this category of AM technologies, both shaping and consolidation are conducted in a single step to obtain the highest achievable density in the as-built part. Conversely, indirect AM first fabricates an intermediate part from the CAD model, necessitating additional processing steps such as sintering to obtain a net-shaped final product. In these indirect AM processes, the AM concept is employed solely to shape the complex part, followed by a PHT for further consolidation and obtaining full density[67].

The two primary categories of direct AM are powder bed fusion (PBF) and directed energy deposition (DED), which involve the direct fusion of metal materials to create the final component[68]. PBF employs a high-energy laser or electron beam to selectively melt powder particles layer by layer (Figures 2(a) and (b)), often resulting in precise details and a superior surface finish[68]. Conversely, DED uses focused energy deposition to melt metal powder or wire, as it is

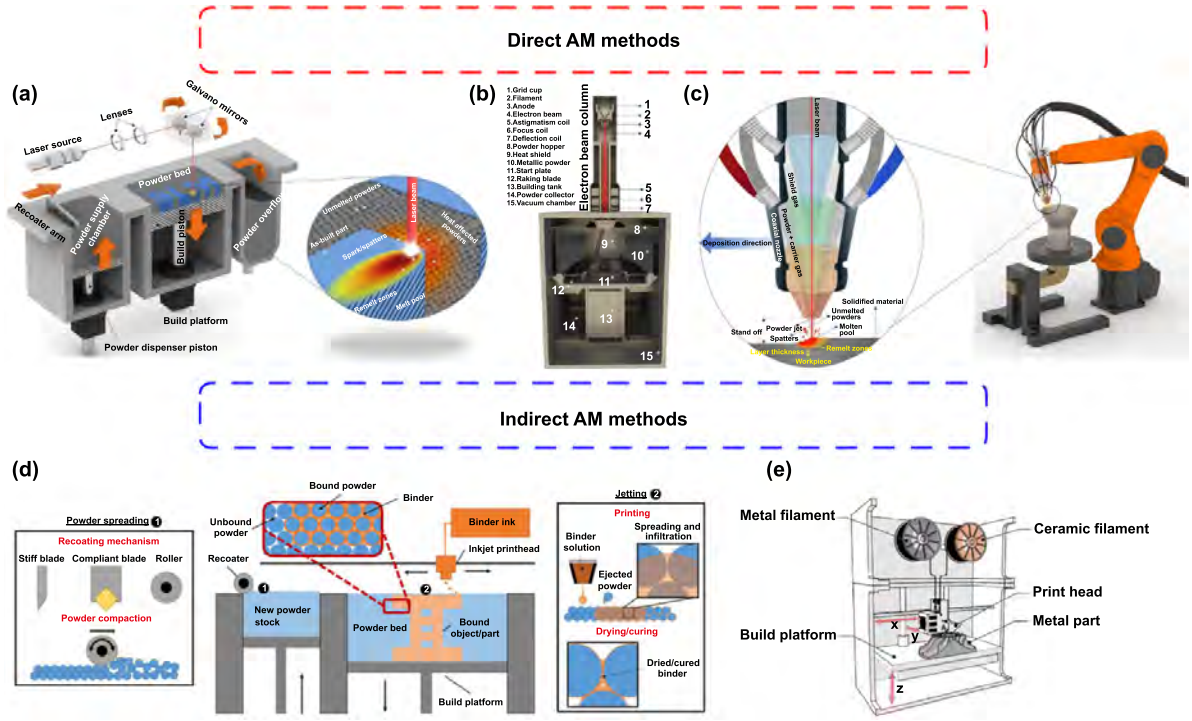

Figure 2. Schematic of AM processes. (a) L-PBF process. Reproduced from[69]. CC BY 4.0. (b) EB-PBF machine. Reproduced from[69]. CC BY 4.0. (c) L-DED technology. Reproduced from[69]. CC BY 4.0. (d) binder jet process. Reproduced from[70], with permission from Springer Nature. and (e) atomic diffusion additive manufacturing process. Reprinted from[71], with the permission of AIP Publishing.

continuously added to a substrate (Figure 2(c))[68]. These direct metal AM methods may be tailored to offer benefits in terms of accuracy, surface quality, and a diverse range of material choices[68]. They are particularly effective in producing complex shapes and are well-suited for applications requiring high precision and intricate features[69].

In contrast, indirect metal AM techniques such as binder jetting (BJ) and atomic diffusion additive manufacturing (ADAM) employ binding agents or polymer matrices to shape the metallic component, which is subsequently consolidated through a post-thermal treatment process. In BJ, as shown in Figure 2(d), a liquid binder is selectively deposited onto the metal powder bed to bind the metallic particles and shape a component called the green part. The green component subsequently undergoes post-processing procedures, such as debinding to eliminate the binder and sintering to melt the metal powder, thereby achieving densification[72]. On the other hand, ADAM involves fabricating components by utilizing metal powder bound within a polymer matrix, as depicted in Figure 2(e). The subsequent debinding and sintering stages facilitate atomic diffusion and densification of the metal powder. These indirect approaches offer benefits in terms of rapid production, reduced equipment expenses compared with direct methods, and suitability for manufacturing large components with intricate geometries[72].

Direct AM technologies present several notable advantages over indirect methods in terms of printing multi-material structures, particularly in terms of precision, integration, and design flexibility. One of the most significant benefits is the precision and control offered in the layer-by-layer deposition of materials. Direct AM allows for the exact placement of different materials, enabling designers to create tailored properties for specific regions of a part. This capability facilitates the development of components with graded properties—such as varying stiffness and thermal conductivity—within a single print. Such design freedom is invaluable in industries like aerospace and biomedical engineering, where complex geometries and integrated multi-material functionalities are essential for optimizing performance and achieving innovative designs.

In addition to enhanced design capabilities, direct AM also promotes resource efficiency and reduces material waste. By building parts additively, this technology minimizes excess material that often arises in subtractive manufacturing processes. The ability to utilize only the necessary amount of material for each layer not only conserves resources but also lowers production costs. Furthermore, direct AM can accommodate a broader range of materials, including metals, ceramics, and polymers, allowing for innovative combinations that leverage the unique properties of each material. This versatility is crucial for creating advanced multi-material structures that can meet specific application requirements. Coupled with faster prototyping and production times, direct AM enables manufacturers to respond more rapidly to design changes and market demands, making it a compelling choice for modern manufacturing challenges.

Notably, there are variations in post-processing requirements between direct and indirect metal AM techniques[73]. Direct metal AM processes typically involve fewer post-processing stages compared to indirect AM methods.

Following the printing phase, direct metal AM components may necessitate the removal of support structures and surface refinement[13,74]. Conversely, indirect metal AM methods often require additional post-thermal treatment processing procedures, such as debinding and sintering. These post-processing activities contribute to the overall processing duration and may introduce additional equipment or facility resources. While direct metal AM techniques can yield fully dense components with exceptional mechanical properties, indirect metal AM methods may exhibit marginally lower density and mechanical attributes[75]. Nevertheless, ongoing advancements in post-processing methodologies have enhanced the material characteristics of indirect metal AM components, rendering them suitable for a diverse range of applications.

In light of the central theme of this review regarding MM processing, a comprehensive summary will be presented on the prevalent use of direct metal AM methods for producing such materials.

3.1. Directed energy deposition methods

DED is recognized as a highly suitable method for metal MM-AM. The continuous delivery of material to the fusion zone is typically facilitated through independently controllable feeding units, with wire and powder being the predominant forms of feedstock. This capability allows for the adjustment of material feedstock during the process, which is integrated within a specific machine cycle[76].

Owing to the relatively rough surface characteristics of DED deposits, considerable resources are currently being allocated to machining processes to achieve the desired net geometry and material properties specified by designers. It is essential to address challenges such as residual stress in intricate applications to produce functional components. The advancement of DED platform technology is progressing rapidly, and the affordability of this technology is increasing as the cost per kilowatt of lasers decreases with the entry of new manufacturers into the market[77].

There are several variations of DED methods, including L-DED (laser directed energy deposition), EB-DED (electron beam directed energy deposition), and WA-DED (wire arc directed energy deposition)[78]. L-DED involves the utilization of a high-powered laser to melt the feedstock material, which is then solidified. In the L-DED process, the laser beam is precisely focused through optics and guided by a scanning system, enabling meticulous control over the deposition process[79]. The laser beam melts the metallic powder at the deposition location, generating a molten pool. Concurrently, a powder nozzle introduces the feedstock material into the molten pool. The molten material solidifies, adhering to the substrate or previous layers and shaping the intended component. L-DED facilitates the production of large, nearly finished parts and the restoration or addition of material to existing components[80]. It provides versatility in working with various material compositions, including metals, alloys, and even composites[78]. L-DED is applicable for tasks such as repair work, cladding, and developing nearly finished parts for sectors like aerospace, oil and gas, and tooling[80,81].

EB-DED is a manufacturing technique that utilizes an electron beam as the primary energy source for depositing material. An electron gun produces the electron beam, which is precisely regulated to selectively melt metallic materials[82]. The metal powder is melted by focusing the electron beam on the workpiece surface. Simultaneously, the starting material is introduced into the molten pool, typically through a powder nozzle. EB-DED presents several advantages, including deep penetration, high energy density, and the ability to process metals with high melting points and refractory compositions[78,83]. This method is particularly suitable for applications that necessitate precise management of heat input and material characteristics, such as those found in the aerospace, energy, and tooling sectors[84].

For the WA-DED process, a consumable metal wire electrode establishes an electric arc with the workpiece. This arc generates the necessary heat to melt the wire material, enabling its deposition onto the substrate or preceding layers. The molten material from the melted wire is continuously fed into the arc zone, ensuring the maintenance of a stable molten pool. Upon cooling and solidification, the material forms the desired component[85]. Compared with alternative DED techniques, WA-DED is distinguished by higher deposition rates, making it a preferred choice for applications requiring large-scale deposition, such as the fabrication and repair of large components in various industries like aerospace, automotive, and marine engineering[86,87].

In contrast to powder bed methods, this process imposes notable limitations, and the resolution is constrained by the standard track widths, which generally measure around 5–10 mm. Although there may be deficiencies in resolution and design flexibility, DED can achieve deposition rates of up to 1 000 $cm^3 \cdot h^{-1}$[88]. This highlights the potential for significant productivity advancements associated with these techniques in the future.

3.2. Powder bed fusion methods

Similar to DED and fused deposition modeling, powder bed techniques are not inherently conducive to multi-material applications. Nevertheless, given that powder bed methods are the most prevalent techniques utilized in industry, their integration of multi-material capabilities could yield substantial advantages, particularly in terms of dimensional accuracy and material variety. PBF provides high precision and controlled layer thickness, enabling the production of intricate geometries with tight tolerances that are essential for industries such as aerospace and medical devices. Additionally, it allows for the integration of various metal powders in a single build, offering flexibility in material choice and enabling the creation of functionally graded materials that optimize performance.

There are two main types of PBF methods: L-PBF and EB-PBF. In L-PBF, a high-power laser is utilized to selectively scan and melt metal powder within a bed to produce the desired components in a layer-wise manner. A scanning system, which

often employs mirrors, directs the laser beam to follow predetermined paths outlined by a digital model of the object. This process continues in a layer-by-layer manner until the entire component is constructed. L-PBF technology provides a high level of accuracy and the ability to manufacture intricate shapes[89] with superior surface quality[82]. This method enables the utilization of a range of metal materials, such as stainless steel[90,91], titanium alloys[68], copper alloys[92], superalloys[93], aluminum alloys[94], and zinc alloys[95]. It is well documented that L-PBF technology is well-suited for creating functional prototypes, limited production runs, and final metal components in high-tech sectors such as the aerospace, medical, and automotive industries[96].

On the other hand, EB-PBF is a manufacturing technique that utilizes an electron beam, rather than a laser, to selectively melt metal powder within a vacuum environment. The electron beam, produced by an electron gun, is meticulously controlled to scan and melt the powder bed, similar to the L-PBF process. EB-PBF has several advantages, including high energy density, minimal contamination due to the vacuum environment, and the ability to work with refractory compositions[97]. This method may also be suitable for producing components with intricate geometries, such as turbine blades[98,99], orthopedic implants[100], and other high-performance applications[101].

It is worth mentioning that there are several challenges that must be addressed in the application of PBF methods for metal MM-AM, such as powder spreading techniques, multi-material process design, and powder cross-contamination[77]. Among these challenges, the most important obstacle to implementation is the necessity for advanced powder deposition equipment that facilitates the deposition of multiple materials. Traditional powder bed methods typically employ a blade or roller to distribute a thin layer of powder over the build area. Recent advancements have led to the development of contactless designs that utilize gravity-assisted deposition for powder spreading. However, the selective placement of various powders across the build area necessitates an alternative approach.

Additionally, the absence of established guidelines for the design of multi-material processes presents another significant barrier to implementation. A pivotal challenge in this domain is the management of the material interface, often referred to as the transition zone. In multi-material PBF, it is imperative to adjust the parameters of the laser or electron beam not only in accordance with the geometry and positioning of the part but also in relation to the composition of the materials involved. Factors such as the development of compositional gradients at the interface, discrepancies in the coefficient of thermal expansion (CTE) between materials, substantial variations in melting temperatures, and fluctuations in the Marangoni number all significantly affect the parameters necessary for processing the interface[77].

Another obstacle to the successful implementation of multi-material PBF is the issue of powder cross-contamination. Regardless of the deposition technique employed, some degree of cross-contamination is nearly unavoidable. It is improbable that any apparatus designed for multi-material powder deposition can achieve a state of zero cross-contamination. Even minimal levels of cross-contamination between different powders can lead to the formation of undesirable phases, deterioration of mechanical properties, or defects at the interfaces of the materials, all of which can compromise the integrity and performance of the final product. Advancements in machine development, particularly in sensor technology for the detection of residual particles and contamination, may provide potential solutions to this challenge.

In summary, the selection between PBF and DED additive manufacturing processes is typically influenced by different factors, such as material specifications, component dimensions, deposition speeds, and economic factors. Each technique offers distinct benefits and finds application across diverse industrial sectors for particular AM needs.

4. Additive manufacturing of multi-materials

4.1. Directed energy deposition of multi-materials

DED is highly desirable because of its ability to manufacture large-scale components quickly and efficiently. Additionally, it is possible to have several or combined powder-feeding systems, which makes them highly flexible in controlling desirable material combinations during the fabrication of MM with complex compositional gradient design for original parts or even the repair of worn parts. Hence, numerous studies on MM regarding base material groups have been popularly implemented via DED[102–104].

The Fe−Ni family is one of the most extensively studied material groups in the literature[105]. It includes a wide range of parent alloys, designs, processes, and studied aspects. This group plays a crucial role in critical energy industries because it balances functional properties and cost-effectiveness[106,107]. In this regard, Kim et al.[108] examined L-DED-fabricated FGMs in 10 wt% steps ranging from pure Inconel 718 (IN718) to pure stainless steel 316 L (SS316L) and determined defective (cracked) compositional regions of 30 wt%−20 wt% SS316L, which deteriorate the mechanical properties. The thermodynamic calculations for equilibrium conditions in Figures 3(a) and (b) show phase fractions by temperature for a defective composition of 20 wt% SS316L and an overall compositional range of SS316L at 500−1 500 °C. The presence of Al_2O_3 and TiO_2 ceramic oxides, confirmed by transmission electron microscopy (TEM) resulting from oxidation at those temperatures, led to the initiation of defects, which then spread along the metal carbides and intermetallic compounds in that region. In addition, the columnar to equiaxed transition (CET) occurs due to increased supercooling, which aggravates the formation of defects by reducing the cohesion of the grain structure and concentrating thermal stresses at the grain boundaries, resulting in reduced structural integrity and loss of mechanical properties. The authors demonstrated that the deliberate and strategic removal of the defective region (Figure 3(c)) can lead to a reliable FGM. Furthermore, the microstructural evolution of the FGM

Table 1. Comparison of the room-temperature tensile properties of the SS316L/IN718 MMs fabricated via L-DED.

Design	PHT condition	UTS/MPa	Elongation/%	References
FGM (50 wt% mixed section between the terminal alloys)	AB	660	16	[109]
	0.5 h solutionizing at 980 °C, followed by 4 h aging at 720 °C (HT1)	668	19.5	
	0.5 h solutionizing at 1 080 °C, followed by 4 h aging at 720 °C (HT2)	666	21	
Bimetal (perpendicular interface to the loading direction)	AB	668 ± 16	26 ± 10	[110]
	8 h at 720 °C followed by furnace cooling + 8 h at 720 °C followed by air cooling	702 ± 6	33 ± 2	
Bimetal (parallel interface to the loading direction)	AB	793 ± 3	26 ± 1	
	8 h at 720 °C followed by furnace cooling + 8 h at 720 °C followed by air cooling	973 ± 27	14 ± 0.5	
Bimetal	AB	510 ± 15	48.5 ± 0.5	[114]
FGM (50 wt% mixed section between the terminal alloys)	AB	540 ± 10	52 ± 2	
FGM (25 wt% increment between the terminal alloys)	AB	420 ± 23	23.5 ± 3	

with only an intermediate mixed section between the terminal alloys influenced by various heat treatments (HT1, HT2: 980 and 1 080 °C, respectively, with 0.5 h of solutionizing, followed by 4 h of aging at 720 °C) was studied by Lu and Li[109]. As shown in Figure 3(d), HTs lead to finer equiaxed grains in the SS316L region caused by recrystallization and thinner interdendrites in the mixed region due to dissolution in the matrix compared to the as-built (AB) state. In addition, the continuous Laves phase in the IN718 region of the AB specimen, whose continuity can exacerbate hot crack susceptibility and adversely affect mechanical properties, is partially dissolved and transformed into a granular shape by HTs. As demonstrated via TEM, strengthening phases of the delta, gamma prime, and gamma double prime were reprecipitated at the grain boundaries in this region. This microstructural evolution over the FGM regions resulted in improved tensile properties and wear resistance, especially when the samples were solutionized at 1 080 °C (HT2). Another study investigated the effect of the interface orientation in the IN718/SS316L bimetal for as-deposited (AD) and HT conditions on the tensile behaviour and fracture mechanism[110]. As the non-contact digital image correlation (DIC) analysis using benchmarked tensile samples and image acquisition by a high-frame camera in Figure 3(e) shows, strains in the ZYX-oriented specimen with a perpendicular interface to the loading direction were localized within the SS316L region away from the interface until final fracture, regardless of post-treatment conditions. This resulted in a tensile behaviour similar to that of the weaker alloy, i.e., SS316L. In contrast, deformation in the YZX-oriented specimen remained uniform until the ultimate tensile strength (UTS) and then began to localize within the IN718 region by crack initiation and subsequently propagation through the SS316L region to the final fracture. Hence, the YZX-oriented specimen effectively benefits from the strengths of both alloys, achieving significant tensile properties of (973 ± 27) MPa UTS and (14 ± 1)% elongation after heat treatment. The latter result confirms the enhanced mechanical properties of the correctly designed FGM under PHT conditions (Table 1) due to partial dissolution of the low-melting and brittle Laves phase and instead the distribution of stable strengthening phases.

In addition to the SS316L/IN718 MM, other terminal alloys in the Fe−Ni material group have attracted the attention of researchers. For example, Jeong et al.[111] studied a novel ultrasonic-assisted WA-DED of SS308L/IN718 FGM and found enhanced mechanical properties, such as the hardness distribution in Figure 3(f), with ultrasonic treatment offering equiaxed grains refinement and improved homogeneity. Elsewhere, the corrosion behaviour of SS316L/IN625 MM with direct and graded transition designs in a hydrofluoric acid (HF) environment was investigated. Regardless of the design, the MM corrosion rate in the partial immersion test was less than 1 $mm \cdot y^{-1}$. However, localized macro-galvanic corrosion was observed at the interface of the direct design (Figure 3(g)), which was effectively eliminated in the graded sample (Figure 3(h)) because of the reduced galvanic effect resulting from the gradual increase in Ni[112]. In another research, Nie et al.[113] studied the relationship between the microstructure and wear properties of SS316/NiTi FGM ultra-thick coatings fabricated via L-DED. Compared

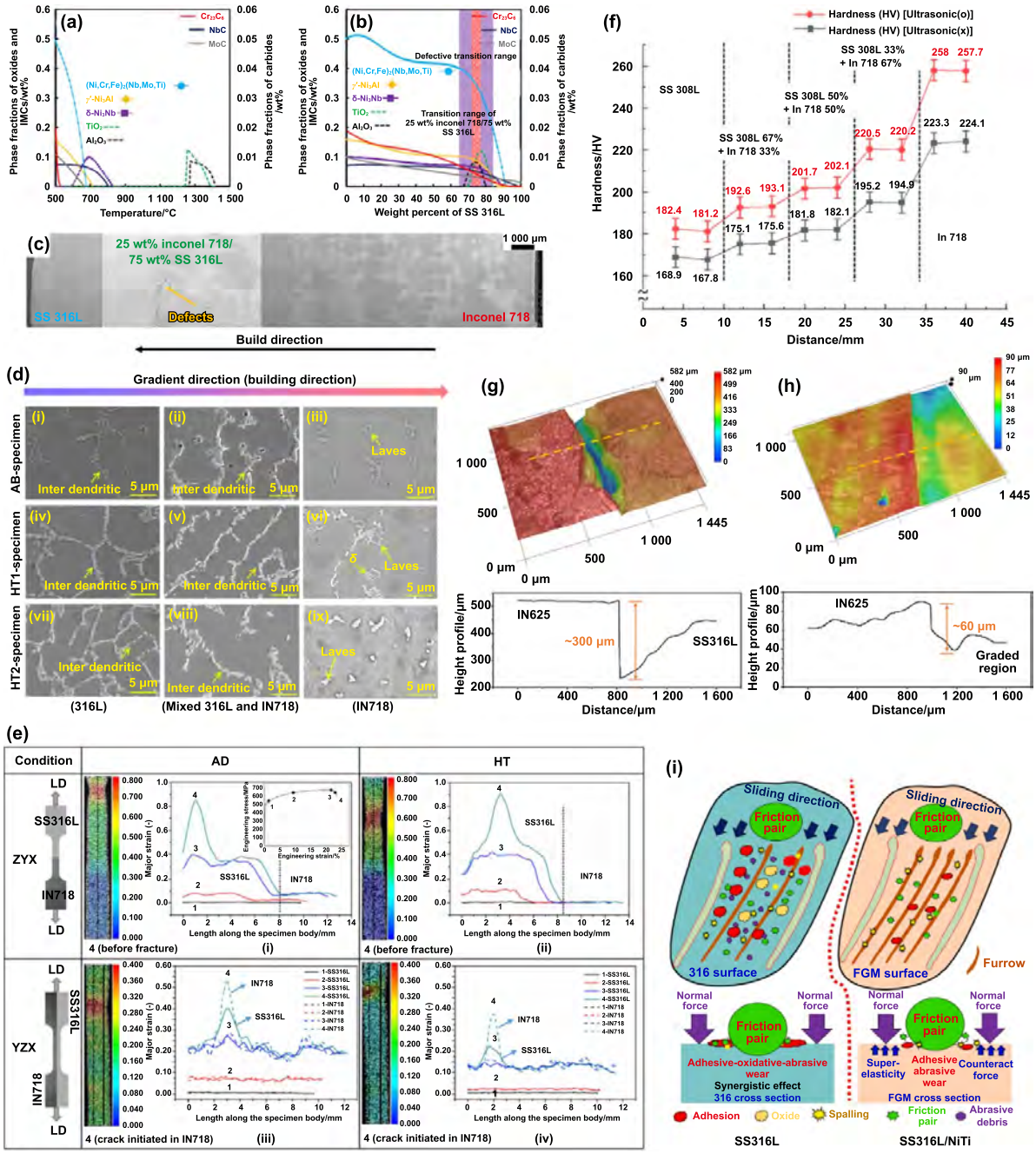

Figure 3. Design–structure–property relationships for MMs made from Fe–Ni material group. (a) and (b) Equilibrium phase fractions by temperature for the crack-prone composition and SS316L weight percent, respectively. (c) Macrograph demonstrating the cracked region (20 wt% SS316L). Reprinted from[108], Copyright (2021), with permission from Elsevier. (d) Microstructure of different areas in the AB, HT1, and HT2 specimens. Reprinted from[109], Copyright (2023), with permission from Elsevier. (e) Local strain distribution at the selected stages (1–4) during tensile test respecting the interface orientation and post-treatment conditions[110] of SS316L/IN718 MM. Reprinted from[110], Copyright (2024), with permission from Elsevier. (f) Hardness distribution of the SS308L/IN718 MM with and without ultrasonic treatment. Reprinted from[111], Copyright (2024), with permission from Elsevier. (g) and (h) 3D surface morphologies and height profiles of the HF-attacked interface of the direct and graded transition of SS316L/IN625 MM. Reprinted from[112], Copyright (2024), with permission from Elsevier. (i) Schematic of the wear mechanisms in the SS316 vs. SS316/NiTi MM cross-sections. Reprinted from[113], Copyright (2023), with permission from Elsevier.

with that of SS316, the wear resistance of the FGM structure increases when the contribution of NiTi increases, regardless of the friction speed. This occurs due to the superplasticity effect, the increased hardness resulting from solid-solution strengthening, and the formation of Fe_2Ti and Ni_3Ti intermetallic compounds. These factors lead to less oxidative and abrasive wear, as illustrated in Figure 3(i).

Despite the high metallurgical incompatibility in the Fe−Ti material group, several promising attempts have been made regarding the design and fabrication of MM structures,

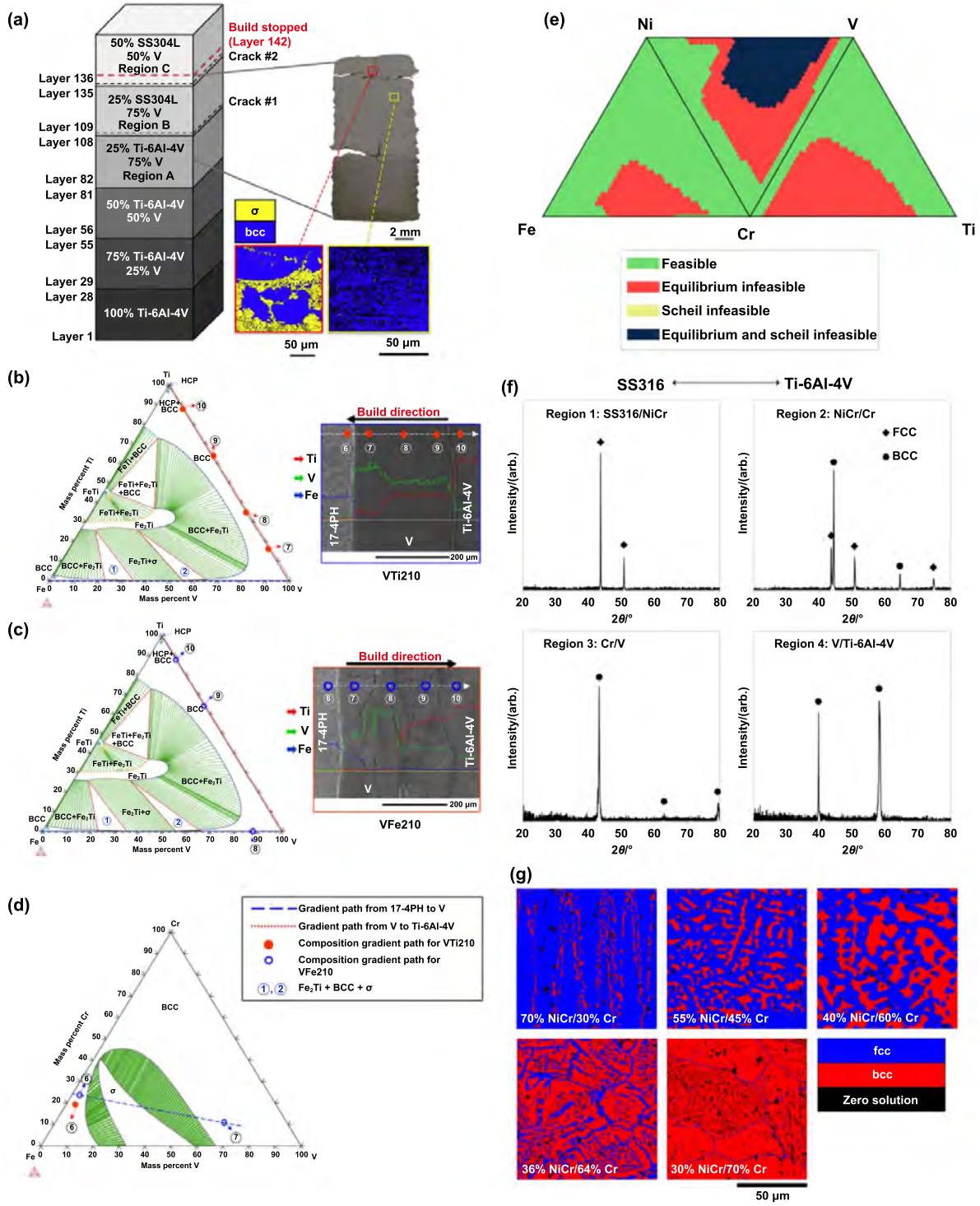

Figure 4. Design–structure–property relationships for MMs made from Fe–Ti material group. (a) Structural design of the Ti6Al4V/V/SS304L MM and cracks location (determined in the regions containing SS304L) beside the sample cross-section and EBSD phase maps from areas shown on it. Reprinted from[115], Copyright (2018), with permission from Elsevier. Ternary phase diagrams of the (b) and (c) Fe–Ti–V and (d) Fe–Cr–V systems at 850 °C and EDS line analysis illustrating composition gradient paths for the Ti6Al4V/V/SS17-4 PH MM respecting the build direction. Reprinted from[116], Copyright (2022), with permission from Elsevier. (e) Ternary feasibility diagrams based on equilibrium and Scheil calculations representing the designable pathway, (f) XRD analysis of gradient regions, and (g) EBSD phase maps of NiCr/Cr region in SS316/NiCr/Cr/V/Ti6Al4V MM. Reprinted from[117], Copyright (2022), with permission from Elsevier.

particularly for their important applications in high-tech industries such as aerospace. As illustrated in Figure 4(a), Bobbio et al.[115] proposed a Ti6Al4V/SS304L FGM structure through intermediate incorporation of V to avoid the formation of Fe−Ti brittle phases in the direct joining of terminal alloys. However, the transition from 25/75 to 50/50 of the SS304L/V

vol% ratios resulted in severe cracking due to the formation of a σ-FeV brittle phase, and the fabrication process was halted before reaching 100 vol% SS304L. Adomako et al.[116] investigated the sequential deposition of V, then SS17-4 PH on Ti6Al4V (VTi), and then Ti6Al4V on SS17-4 PH (VFe) using different laser powers to determine their effects on the deposition of the V interlayer. The VTi structure produced by laser powers of 180 W and 210 W (VTi180 and VTi210) was found to be crack-free throughout its length, whereas several cracks were observed in VFe180 and VFe210 near the interface of V/SS17-4 PH. Following the gradient paths of VTi210 (solid circles) and VFe210 (hollow circles) on the equilibrium ternary phase diagrams of Fe–Ti–V and Fe–Cr–V in Figures 4(b)–(d), it is evident that the microstructure of VTi210 is mainly composed of a BCC solid solution. However, the transition from Zone 6 to Zone 7 in VFe210 indicates the presence of the brittle σ phase, which is predicted to be caused by a higher Fe incorporation in the V interlayer compared to VTi210. The formation of the σ phase was confirmed through advanced microstructural analyses, identifying it as the cause of cracking in the VFe structure. Therefore, the V interlayer should be avoided in the Fe–V–Ti sequence, and the highest tensile strength could be achieved by the VTi210 structure, which has an exceptional value of 700 MPa.

In another study by Bobbio et al.[117], equilibrium thermodynamic calculations and Scheil−Gulliver solidification simulations were combined to create ternary feasibility diagrams (Figure 4(e)) for the informed design and fabrication of an SS316/Ni-20Cr/Cr/V/Ti6Al4V FGM without detrimental phases and risk of cracking. Figure 4(f) shows the X-ray diffraction (XRD) analysis results obtained from the four gradient regions of the FGM. The transitions from the FCC single phase (Region 1) to the FCC/BCC mixture phases (Region 2) to the BCC single phase (Regions 3 and 4) experimentally demonstrated the viability of the pathway designed through feasibility diagrams without any deleterious phases. Moreover, the electron backscatter diffraction (EBSD) phase maps in Figure 4(g) from the five locations of Region 2 (CrNi/Cr), which are consistent with the XRD observations, validated the prediction of phase compositions within this region as the transformation from FCC-rich to equiaxed BCC-rich structures caused by elemental segregation. It was also noted that the zero solution areas were, in fact, the BCC Cr-rich particles. This promising result demonstrates thermodynamic calculations (esp. considering non-equilibrium conditions) as a useful and reliable method to feasibly design gradient paths between incompatible terminal alloys without the risk of detrimental phases and cracking. Nevertheless, this method still suffers from the limited thermodynamic database for multi-component and new alloy systems, although it is progressing.

Moving forward to another material group, Ni−Ti MMs are highly desirable for providing high tensile and fatigue strengths, excellent corrosion and oxidation resistance, and being lightweight in a single part, making them suitable for aerospace and biomedical applications. For instance, Huang et al.[118] examined Ti6Al4V/IN625 FGM manufactured by controlling the filling ratio of base alloy wires and using a pulsed alternating current in the WA-DED process. As the microstructure of the gradient layers in Figure 5(a) shows, in accordance with the increasing IN625 contribution according to the numbered Ni elemental contents in the Ti−Ni phase diagram in Figure 5(b), the Ti_2Ni fraction phase increases via eutectic and eutectoid reactions (compositions 1 and 2) and further via pre-eutectic formation (compositions 3 and 4), whereas the α-Ti and β-Ti phases decrease. Moreover, the TiNi phase precipitates via the peritectic reaction in composition 5, although it also exists in composition 4 due to the non-equilibrium condition. It was reported that the hardness, compressive strength, and wear resistance improved with increasing Ti_2Ni content and the presence of TiNi in the top layers, whereas the plasticity decreased.

Park et al.[119] employed V/Cr/Ni multi-interlayers to develop a robust joint between Ti6Al4V and IN718, thereby avoiding brittle intermetallic compounds (IMCs) and encouraging crack formation. Figures 5(c) and (d) show the fabricated Ti6Al4V/V/Cr/Ni/IN718 MM and its corresponding cross-sectional macrograph, respectively, indicating successful crack-free bonding over the structure. The EBSD results in Figure 5(e), including the image quality (IQ), inverse pole figure (IPF), phase map, and kernel average misorientation (KAM) figures from every individual interface, demonstrated the ability of the developed pathway to form IMC-free solid solutions between the terminal alloys. Furthermore, the minimum misorientation of the grains in the deposited regions, as indicated by the quantitative finite element analysis in Figure 5(f), suggests a moderate residual stress distribution throughout the MM. These structural features resulted in a considerable tensile strength of 210 MPa in the as-built state and 250 MPa in the stress-relieved state. Elsewhere, a novel approach of follow-up ultrasonic-assisted L-DED (Figure 5(g)) was used to regulate the morphology and distribution of the Ti_2Ni intermetallic phase in Ti6Al4V/IN718 MM to improve mechanical properties. As depicted schematically in Figure 5(h), the subsequent ultrasonic treatment refined and fragmented the coarse, chain-like Ti_2Ni intermetallic into a granular form through cavitation effects. In addition, the intermetallic phase fraction decreased by alleviating nickel element segregation and restricting the β-Ti transformation to Ti_2Ni due to the acoustic streaming effect and increased cooling rate caused by the promoted thermal convection, respectively. This microstructure control improved the flexural strength from 805 MPa to 1 047 MPa with 1 200 W of ultrasonication[120]. As a critical view of these summarized studies on Ni−Ti MM-AM, it can be concluded that the formation of intermetallic compounds in direct transition between the two terminals is thermodynamically inevitable, and their high fractions lead to structural brittleness and loss of tensile properties. Therefore, modifying the transition path, i.e., using interlayers compatible with terminal alloys or employing assisting techniques to modify the microstructure and finely distribute the Ti−Ni stoichiometric compounds, are practical solutions to realize sound structures made of this material group.

Metal-ceramic MM encompasses a substantial group of extreme environments. The processing of these materials by

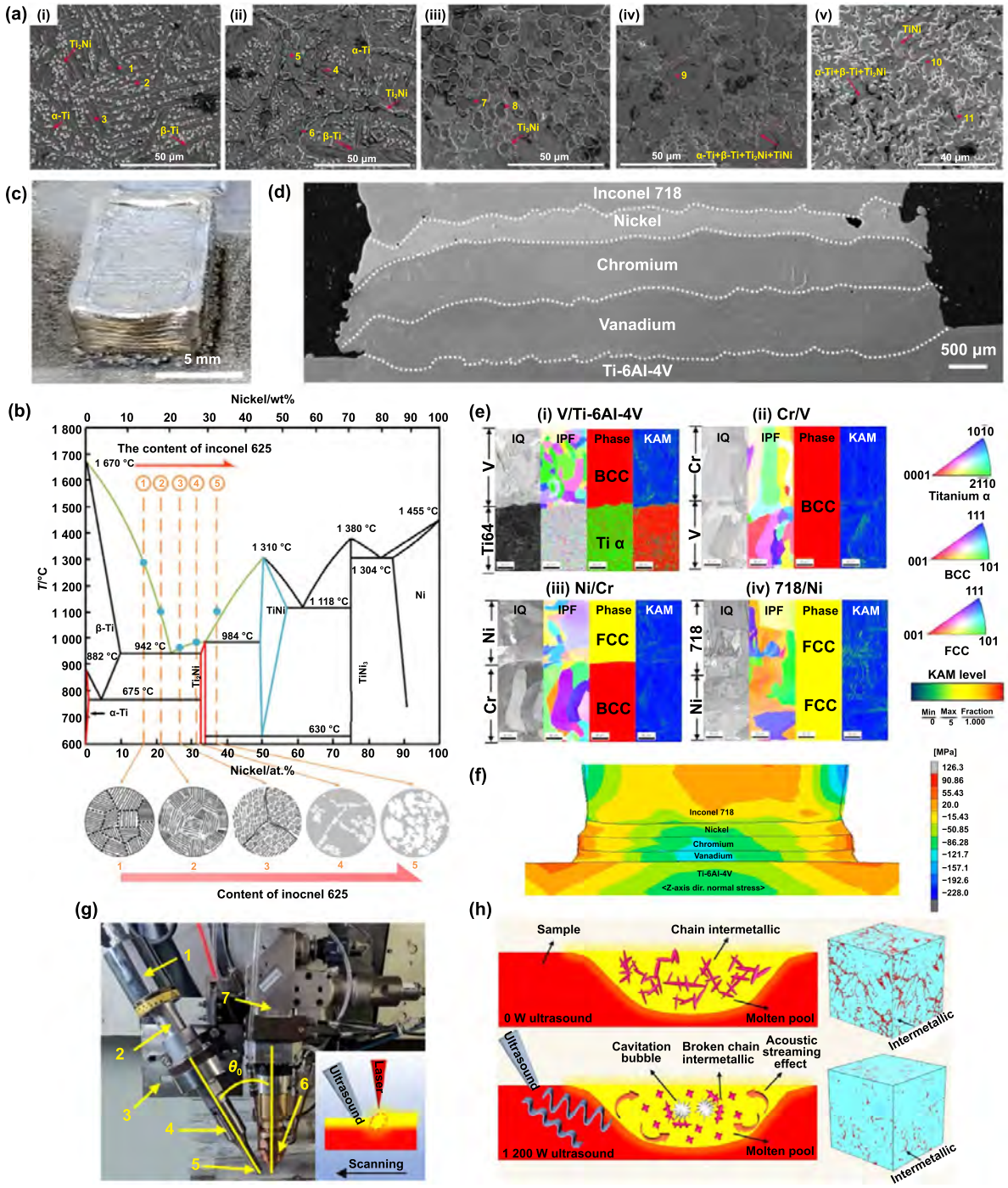

Figure 5. Design–structure–property relationships for MMs made from Ni–Ti material group. (a) The microstructure of gradient layers and (b) corresponding Ni elemental contents schematically shown on the Ti–Ni phase diagram for Ti6Al4V/IN625 MM. Reprinted from[118], Copyright (2022), with permission from Elsevier. (c) Fabricated sample, (d) cross-sectional macrograph, (e) EBSD results from the interfaces, and (f) residual stress (σ_z) distribution in the cross-section of Ti6Al4V/V/Cr/Ni/IN718 MM. Reproduced from[119]. CC BY 4.0. (g) Ultrasonic-assisted L-DED equipment and (h) mechanism of microstructure modification utilizing ultrasound in the L-DED of Ti6Al4V/IN718 MM. Reprinted from[120], Copyright (2022), with permission from Elsevier.

DED is of great interest because of the wide variety of parent materials, particularly in gradient designs. This serves largely different properties while avoiding delamination, cracking, and premature failure arising from thermal mismatch stresses. As an inspiring work, Zhang and Bandyopadhyay[121] developed a Ti6Al4V/Al_2O_3 FGM via laser-engineered net shaping (LENS $\sim$ L-DED), as shown in Figure 6(a). They reported some pores, unmelted ceramic particles, and micro-cracks within the Ti6Al4V + Al_2O_3 mixed section. In contrast, the pure Al_2O_3 section was fully dense and defect-free, with the highest average hardness of 2 365.5 $HV_{0.3}$. An optimal energy density (combination of laser

power and scanning speed) and ceramic powder feed rate could potentially result in complete fusion/dissolution/mixing of the particles in the melt pool with minimal thermal stresses and consequently eliminate those defects in the mixed section. However, some issues may remain due to significant inherent differences between parent materials, such as highly different melting temperature ranges and thermal expansion coefficients. In another work, researchers realized a compositional gradient structure from 100% metal to 100% ceramic in SS304/VC FGM (Figure 6(b))[122]. Despite some porosities over the gradient layers and additional microcracks in the 100% VC, the hardness distribution profile in Figure 6(c) exhibits a gradual variation, indicating viable interfacial strength and a low probability of delamination. Additionally, the wear rate of the SS304 substrate decreased by 95% in the pure VC outer layer against the abrasive water jet. Moreover, it was reported that performing a laser pass could improve both the hardness and wear resistance of the FGM, owing to better densification and more homogeneous VC dispersion.

The hypothesis that a gradient design could help reach a higher ceramic content in the L-DED of metal-ceramic MM was also demonstrated by Ostolaza et al.[123] for Stellite 6/WC FGM coatings on AISI H13 tool steel by preventing surface cracks during the process. Furthermore, a comparison of the tribological behaviour at room temperature (RT) and 400 °C via optical profilometry of the wear traces in Figure 6(d) indicated that the quenched and tempered (Q + T) AISI H13 had better RT wear performance owing to the higher integrity of the hot-rolled condition. The samples coated with Stellite 6, Stellite 6/WC mono-composition (5% WC MONO), and Stellite 6/WC FGM (5% and 10% WC FGMs) exhibited improved wear resistance, especially when the WC content was increased to 10% (due to the FGM design) at 400 °C. This shift was from abrasive wear at room temperature to an oxidative wear mechanism. Zhang et al.[124] studied the microstructure evolution in L-DED fabrication of Ti6Al4V/TiC FGM with up to 50 wt% TiC. The microstructural morphologies of the FGM in Figure 6(e) demonstrated that the fraction and size of the unmelted TiC particles gradually increased with increasing incorporation of TiC. This increase is attributed to a reduction in TiC dissolution through diffusion in the carbon-rich melt pool, leading to a decrease in the concentration gradient. In addition, the chain-like and granular TiC phases formed by the eutectic reaction were gradually substituted with the granular and dendritic primary TiC phases by increasing the carbon content in the melt pool, as determined schematically in the phase diagram in Figure 6(f). A further increase in carbon content due to TiC incorporation resulted in coarser secondary phases and finer equiaxed β-Ti matrix phases caused by higher constitutional supercooling, leading to a deterioration in tensile properties. At the end of the current sub-section, the studies on multi-material DED are classified in Table 2, along with a summary of the features addressed.

An important factor often overlooked is the deposition sequence, i.e., which material is deposited first, as it can dramatically affect the interface microstructure and integrity. Multiple studies on DED and PBF have demonstrated that reversing the build sequence can lead to distinctly different interfacial conditions due to changes in thermal history and dilution[182]. For example, Wang et al. compared two deposition orders for an IN718/CuSn10 bimetal fabricated by L-DED: when Inconel 718 was deposited first, followed by the CuSn10 alloy, the interface exhibited excellent bonding with minimal cracking, yielding an ultimate tensile strength (∼566 MPa) between those of the constituent alloys. In this sequence, only a small amount of Cu diffused into the IN718, avoiding brittle Cu-rich phases and instead promoting equiaxed grain formation at the interface (mitigating intergranular cracks). In contrast, depositing CuSn10 first and IN718 on top led to significant Cu penetration into the initial IN718 track, causing pronounced Cu segregation in the dendrites and a steep compositional gradient. This made the IN718-rich interface highly crack susceptible due to the large mismatch in thermal conductivity/expansion, and extensive cracking was indeed observed in this reverse sequence[183]. These findings underscore that the build order (e.g., “A on B” vs. “B on A”) alters the solidification conditions and element diffusion at the junction, often determining whether a sound metallurgical bond or defects, such as interfacial cracks and brittle phases, will form. Similar trends have been reported in other material systems. Iams et al. found that for a GRCop-42 (Cu–Cr–Nb alloy) and Alloy 718 bimetal (DED-built), the precipitate morphology and phase composition in the copper alloy near the interface varied significantly with deposition order. The deposition of Alloy 718 first caused more Ni/Fe to mix into the Cu-alloy, forming undesirable Laves (C14) and α-Cr phases, whereas the reverse sequence (Cu-alloy first) resulted in the expected C15 Cr_2Nb precipitates and a different microstructure[184]. Similarly, Chang et al. reported in a WA-DED study that an aluminum bronze–Inconel 718 bimetal exhibited heterogeneous interface behaviour, depending on whether the steel or bronze was laid down first, further evidencing that the deposition sequence must be optimized to avoid cracks and brittle intermetallics[185]. In summary, the stacking order in multi-material AM (both in DED and PBF contexts) critically influences dilution, residual stress distribution, and interfacial phase formation, and thus should be carefully chosen or engineered (sometimes using intermediate transition layers) to ensure robust bi-material joints[183].

In addition to process parameters, several post-processing and design strategies have been developed to improve the performance of the multi-material interface. One approach is to introduce mechanical interlocks or geometric features at the interface to augment metallurgical bonding with mechanical engagement. Instead of a simple planar interface, a deliberately interlocked geometry can deflect or arrest cracks, thereby increasing load transfer across the interface. For instance, Liu et al. designed a hierarchical interlocking interface in a multi-material LPBF build, which effectively deflected the fracture path along the junction, resulting in improved toughness[186]. Similarly, Squires et al. demonstrated a radial bimetallic WA-DED configuration (308L stainless steel core inside a mild steel shell) that inherently provides in situ mechanical interlocking throughout the build height. The concentric “casing” architecture, combined with a slight mismatch in thermal

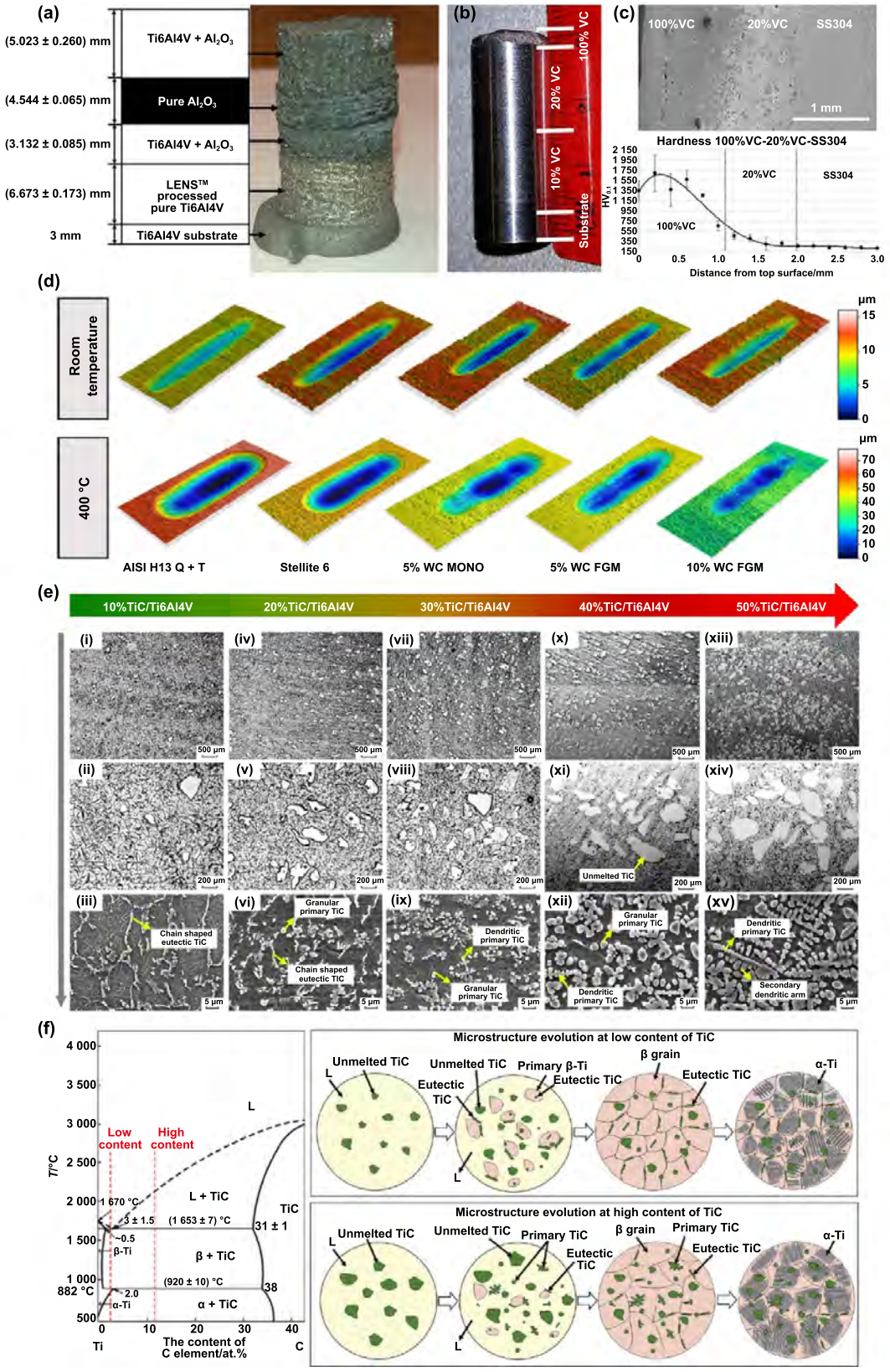

Figure 6. Design–structure–property relationships for various metal–ceramic MMs. (a) Schematic and cylindrical structure of Ti6Al4V/Al_2O_3 MM. Reprinted from[121], Copyright (2018), with permission from Elsevier. (b) Machined gradient cylinder and (c) hardness profile with the cross-sectional microstructure of SS304/VC MM. Reprinted from[122], Copyright (2018), with permission from Elsevier. (d) Wear profilometry of AISI H13 Q + T, Stellite 6, and Stellite 6/WC MM specimens tested at different temperatures. Reproduced from[123]. CC BY 4.0. (e) Microstructure of the graded compositions and (f) Ti–C phase diagram with schematic of microstructure evolution at high and low contents of TiC in Ti6Al4V/TiC MM. Reprinted from[124], Copyright (2024), with permission from Elsevier.

Table 2. Summarized features of selected studies on multi-material DED additive manufacturing.

Material groups	Parent materials	Designs	Processes[a]	Reported defects	Studied properties	References
Fe-Ni	SS316L/IN718	Layered	L-DED	Porosity, lack of fusion, unmelted particles	Tensile & fracture toughness	Melzer et al.[125]
		FGM	L-DED	Porosity	Hardness	Ghanavati et al.[126]
		FGM	L-DED	Porosity, cracking, oxidation	Hardness	Kim et al.[108]
		FGM	L-DED (PHT)	Porosity	Hardness	Li et al.[127]
		FGM	L-DED (PHT)	None	Hot corrosion	Xu et al.[128]
		FGM	L-DED (PHT)	Porosity	Wear & tensile	Lu and Li[109]
		Bimetal	L-DED (PHT)	None	Room and high-temperature tensile & creep	Li et al.[110]
	SS316L/IN625	FGM	L-DED	None	Hardness & tensile	Tong et al.[129]
		Crossed-lamellar	L-DED	Cracking	Hardness & tensile	Li et al.[130]
		Bimetal & FGM	L-DED	None	Corrosion	Zhang et al.[112]
	SS304L/IN625	FGM	L-DED (PHT)	Cracking	Hardness	Fan et al.[131]
	SS904L/Hastelloy C-276	Bimetal	WA-DED	None	Tensile & fatigue	Rajesh Kannan et al.[132]
	SS413/IN625	FGM	L-DED (PHT)	Cracking & oxidation	Hardness	Ferreira et al.[133]
	SS316L/IN825	FGM	WA-DED	None	Hardness & tensile	Senthil et al.[134]
	SS304L/Ni-20Cr	FGM	L-DED	None	Hardness & tensile	Bobbio et al.[135]
	SS420/IN718	Mixed compositions	L-DED	None	Hardness & tensile	Aydogan et al.[136]
	SS304/IN738LC	Bimetal	L-DED	Crystal defects (e.g., misfit dislocation arrays, stacking fault, etc.)	Hardness & tensile	Dang et al.[137]
	SS308L/IN625	FGM	WA-DED	Cracking	Tensile	Li et al.[138]
	SS308L/IN718	FGM	Ultrasonic-assisted WA-DED	None	Hardness & tensile	Jeong et al.[111]
	18Ni300 maraging steel/IN625	FGM	L-DED	Porosity	Hardness, wear, compressive	Zhang et al.[139]
	SS316/NiTi	FGM	L-DED	None	Hardness & wear	Nie et al.[113]

(Continued.)

Table 2. (Continued.)

Material groups	Parent materials	Designs	Processes[a]	Reported defects	Studied properties	References
Fe-Ti	SS304L/V/Ti6Al4V	FGM	L-DED	Cracking	Hardness	Bobbio et al.[115]
	SS316/Fe/Cr/V/Ti6Al4V	Interlayer	L-DED	Porosity	Hardness	Li et al.[140]
	SS316L/Ni20Cr/Cr/V/Ti6Al4V	FGM	L-DED	Porosity	Hardness	Bobbio et al.[117]
	SS17-4 PH/V/Ti6Al4V	Interlayer	L-DED	Porosity, incomplete melting, cracking, delamination, residual stress	Hardness & tensile	Adomako et al.[116]
	SS316L/Ti6Al4V	FGM	L-DED	Porosity & cracking	Hardness & tensile	Xu et al.[141]
		FGM	L-DED	None	Hardness, wear, tensile	Xu et al.[142]
Fe-Cu	SS316L/Nickel-aluminum bronze	Bimetal	WA-DED	Cracking	Hardness	Dharmendra et al.[143]
	SS321/C11000 Cu alloy	Layered	EB-DED	Heterogeneous distribution of materials at the interfacial zones	Hardness, tensile, thermal expansion coefficient	Osipovich et al.[144]
	SS316L/Cu	Bimetal & interlayer (IN718)	L-DED	Residual stress	Hardness, tensile, thermal conductivity, thermal diffusivity	Zhang et al.[145]
		Bimetal	WA-DED	None	Hardness, tensile, impact	Tomar and Shiva[146]
	H13 tool steel/Deloro 22/Cu	Bimetal & interlayer	L-DED	Cracking	Hardness, tensile, Thermal conductivity	Zhang et al.[147]
	Invar/MnCu	FGM	L-DED	None	Hardness & tensile	Fan et al.[148]
Fe-based	SS316L/SS431	FGM	L-DED	None	Hardness & corrosion	Nie et al.[149]
	SS316L/C300 maraging steel	FGM	L-DED (PHT)	None	Hardness & tensile	Ben-Artzy et al.[150]
	SS316L/M300 maraging steel	FGM	L-DED	None	Hardness	Oropeza et al.[151]
	SS316L/low carbon steel	FGM	L-DED	Porosity, keyhole, residual stress	Hardness, tensile, Thermal expansion coefficient	Shin et al.[152]
	SS316L/ER70S-6	Bimetal	WA-DED	Oxidation	Hardness & tensile	Zhai et al.[153]
	SAF 2507 duplex steel/SS15-5 PH	Bimetal	L-DED	None	Hardness, tensile, corrosion	Koukolíková et al.[154]

(Continued.)

Table 2. (Continued.)

Material groups	Parent materials	Designs	Processes[a]	Reported defects	Studied properties	References
Ni-Ti	IN625/Ti6Al4V	FGM	WA-DED	None	Hardness & compressive	Han et al.[155]
		FGM	WA-DED	None	Hardness, wear, Compressive	Huang et al.[118]
	Ti6Al4V/Monel 400/IN718	Interlayer	WA-DED	None	Hardness	Mishra et al.[156]
	IN718/Ni/Cr/V/Ti6Al4V	Interlayer	L-DED (PHT)	Porosity & unmelted particles	Hardness & tensile	Park et al.[119]
	IN718/Ti6Al4V	Mixed composition	Ultrasonic-assisted L-DED	None	Hardness & flexural	Wu et al.[120]
		Bimetal & interlayer (Ti-Nb-Cr-V-Ni HEA)	L-DED	Cracking & delamination	Hardness	Jeong et al.[157]
	Ti6Al4V/NiTi	FGM	L-DED	Cracking & delamination	Hardness & tensile	Li et al.[158]
Ni-Cu	IN718/GRCop-84 Cu alloy	Bimetal & FGM	L-DED	Porosity	Hardness & thermal diffusivity	Onuike et al.[159]
	IN718/CuSn10 bronze	Bimetal	L-DED	Porosity & cracking	Electrical resistivity, seebeck coefficient, hardness, compressive	Grandhi et al.[160]
	IN625/Cu	FGM	WA-DED	None	Hardness, tensile, corrosion	Wang et al.[161]
	GH4169 Ni alloy/C18150 Cu alloy	Bimetal	WA-DED	None	Hardness & tensile	Liu et al.[162]
Ti-Al	Ti6Al4V/AlSi10Mg	FGM	L-DED	Cracking	Hardness & tensile	Liu et al.[163]
	Ti/Al	FGM	WA-DED	None	Hardness, tensile, oxidation	Wang et al.[164]
	Ti6Al4V/TiAl	Bimetal & FGM	L-DED	Cracking	Tensile	Ma et al.[165]
	Ti6Al4V/Al2024	Bimetal	L-DED	Cracking & residual stress	Hardness	Zhang et al.[166]
		Bimetal & interweaving	L-DED	Porosity & cracking	Shear	Zhang et al.[167]
	Ti6Al4V/Al2219	FGM	L-DED	Unmelted particles & cracking	Coefficient of thermal expansion	Tonyali et al.[168]

(Continued.)

Table 2. (Continued.)

Material groups	Parent materials	Designs	Processes[a]	Reported defects	Studied properties	References
Metal-Ceramic	SS304/VC	FGM	L-DED	Porosity & cracking	Hardness & wear	Gualtieri and Bandyopadhyay[122]
	Ti6Al4V/Al_2O_3	FGM	L-DED	Porosity, unmelted particles, cracking, delamination	Hardness	Zhang and Bandyopadhyay[121]
	Ti6Al4V/Ti-Si-C	FGM	L-DED	Porosity	Hardness & flexural	Li et al.[169]
	NiCrAlY/Yttria-stabilized zirconia (YSZ)	FGM	L-DED	Delamination	Thermal conductivity, thermal expansion, thermal cycling	Savitha et al.[170]
	Ti6Al4V/Zirconia-toughened alumina (ZTA)	FGM	L-DED	None	Hardness & wear	Zheng et al.[171]
	Ti6Al4V/TiC	FGM	L-DED	Porosity	Hardness & tensile	Zhang et al.[124]
	Al5356/TiC-B_4C	FGM	Powder-fed WA-DED	Porosity & particle aggregation	Hardness, tensile, wear	Sun et al.[172]
	Al7075/Ti+B_4C	Homogeneous & FGM	L-DED	None	Hardness, flexural, wear	Wang et al.[173]
	Stellite 6/WC	FGM	L-DED	Cracking	Hardness & room and high-temperature wear	Ostolaza et al.[123]
Others	Ti6Al4V/Mo	FGM	L-DED	Unmelted particles	Hardness	Schneider-Maunoury et al.[174]
	Ti/Nb	FGM	L-DED	Unmelted particles	Hardness & tensile	Schneider-Maunoury et al.[175]
	Ti/Cr	FGM	L-DED	None	Hardness	Thomas et al.[176]
	IN718/Haynes 25	FGM	L-DED	None	Hot corrosion	Luo et al.[177]
	IN718/René41	FGM	L-DED (PHT)	Residual stress	None	Huang et al.[178]
	SS316L/Haynes 282	FGM	L-DED	Porosity & irregular layer thickness	Hardness & tensile	MacDonald et al.[179]
	SS316L/Tribaloy™ T800	Bimetal & FGM	L-DED	Cracking	Hardness & wear	Nandi et al.[180]
	SS316L/Al4043	Bimetal	WA-DED	Porosity & cracking	Hardness & tensile	Karim et al.[181]

[a] PHT: post-heat treatment.

expansion between the two steels, introduced beneficial compressive residual stresses at the interface, thereby enhancing strength. Compared with monolithic parts, the as-built bimetal showed a 33%–42% increase in compressive strength, confirming that biomimetic interfacial architecture can significantly improve joint performance[187]. Another technique to strengthen dissimilar interfaces is the use of intermediate layers or graded transitions. By adding a compatible interlayer material (or compositional gradient), the abrupt property mismatch can be mitigated. For example, researchers have successfully deposited a Ni-based intermediary alloy between copper and steel in a DED process, creating a gradual transition that prevents crack-prone binary phases and yields sound bonds. Wei et al. similarly bonded tungsten and copper by inserting a stainless-steel interlayer via DED, avoiding direct W–Cu contact (which tends to form brittle intermetallics)[188]. Such functionally graded or interlayer approaches can reduce thermal stress and inhibit the formation of harmful intermetallic compounds at the bimetal interface.

In addition to geometric and material modifications, post-process treatments such as laser shock peening (LSP) have been adopted to enhance interfacial properties, particularly in DED-fabricated components. LSP involves bombarding the surface with high-energy laser pulses to induce plastic deformation and compressive residual stresses in the near-surface layer. When applied between deposited layers (interlayer peening) or after build completion, LSP can relieve tensile residual stresses and close interfacial defects, thereby enhancing the fatigue performance and strength at the joint. Jing et al. reported notable success in performing in situ interlayer LSP during WA-DED of an Al–Cu alloy. In this research, each layer was peened before depositing, which reduced internal porosity by ∼74% and decreased pore area by ∼87% relative to those of the as-deposited samples. The LSP-treated build also exhibited significantly better mechanical properties; the ultimate tensile strength and yield strength increased by ∼20%, and elongation increased by ∼27%, indicating a simultaneous improvement in both strength and ductility[189]. These gains were attributed to the high dislocation density and compressive residual stress introduced by LSP, as well as localized microstructural refinement (even some recrystallization) at the layer interfaces. The compressive stresses counteract the tensile thermal stresses from deposition, and the plastic deformation "knits" the layers together more tightly, effectively healing or arresting defects at the interface. As a result, the subsequent layers form tighter metallurgical bonds around pore sites, leading to a more robust interface[189]. Although that study was on a single-alloy WA-DED, the same LSP concept has been extended to dissimilar-metal builds, e.g., Chang et al. applied laser shock peening at the interface of a dissimilar aluminum alloy WA-DED joint, achieving improved tensile strength and fatigue life by inducing a tailored stress state at the bimetal interface[190]. Overall, laser shock peening, shot peening, or other surface deformation techniques offer a promising route to enhance multi-material interfaces by imparting compressive stresses and refining the microstructure, thereby improving crack resistance at the joint.

4.2. Powder bed fusion of multi-materials

Despite the established position of DED in the realm of MM-AM, recently, increasing attention has been given to the potential capabilities of another AM method, i.e., PBF, for MM processing. Although PBF is not commonly considered as flexible as DED in terms of composition changes during the process, its unique features, such as higher resolution, tight dimensional tolerance, good surface finish, reduced material waste and contamination, and better performance, have led researchers to propose adaptive mechanisms enabling PBF to handle multiple materials. However, MM fabrication via PBF is still in its infancy and requires further research and development concerning the adaptive mechanisms and material groups to engage and extend[5,8,36,191]. Although electron beam powder bed fusion (EB-PBF) holds significant potential for multi-material additive manufacturing, its adoption lags behind L-PBF for key technical reasons. The required high vacuum complicates powder handling, in situ exchange, and part removal while increasing the risk of cross-contamination. This vacuum environment, along with complex beam control systems, makes EB-PBF machines more expensive and limits practical multi-hopper designs. Powder spreading is also more challenging with dissimilar materials because of altered flow and electrostatic charging. In addition, metallurgical challenges include vastly different beam−material interactions across alloys, preventing rapid parameter tuning. Vacuum can also cause volatile elements to evaporate, altering the local chemistry at material transitions. Finally, in situ monitoring under vacuum is less mature than optical methods in L-PBF, making defects at multi-material interfaces harder to detect. These collective constraints in equipment, handling, metallurgy, and monitoring make EB-PBF less flexible than the more established L-PBF workflows for multi-material applications.

Among the material groups addressed so far, Fe−Cu has the highest publication rate by the multi-material and PBF keywords, which may arise from its vital application in the power generation and conversion sectors, e.g., heat exchangers, thanks to integrating the good mechanical properties of the Fe side and excellent thermal and electrical conductivity of the Cu side in a single part. In this regard, Liu et al.[192] studied different building strategies of a CuSn10 alloy (CuA)/SS316L MM, as illustrated by CS, SC-1, and SC-2 schematics in Figure 7(a), using an L-PBF system equipped with separate powder hoppers and an in situ powder mixer (Figure 7(b)), in which powders volume ratios could be adjusted by controlling the rotation speed of the mixer blade and duration of powder flow. The macrostructure evaluation of the fabricated structures in Figure 7(c) revealed that the smooth gradient transition (SC-2) aggravated the interfacial cracking observed in SC-1. This was caused by liquid metal embrittlement induced by increased Cu penetration into the Fe grains, resulting in delamination similar to SC-1. In contrast, a wider diffusion zone and inhibited Cu-penetration cracks due to the enhanced fluid flow in the melt pool could lead to good metallurgical bonding with no delamination in the

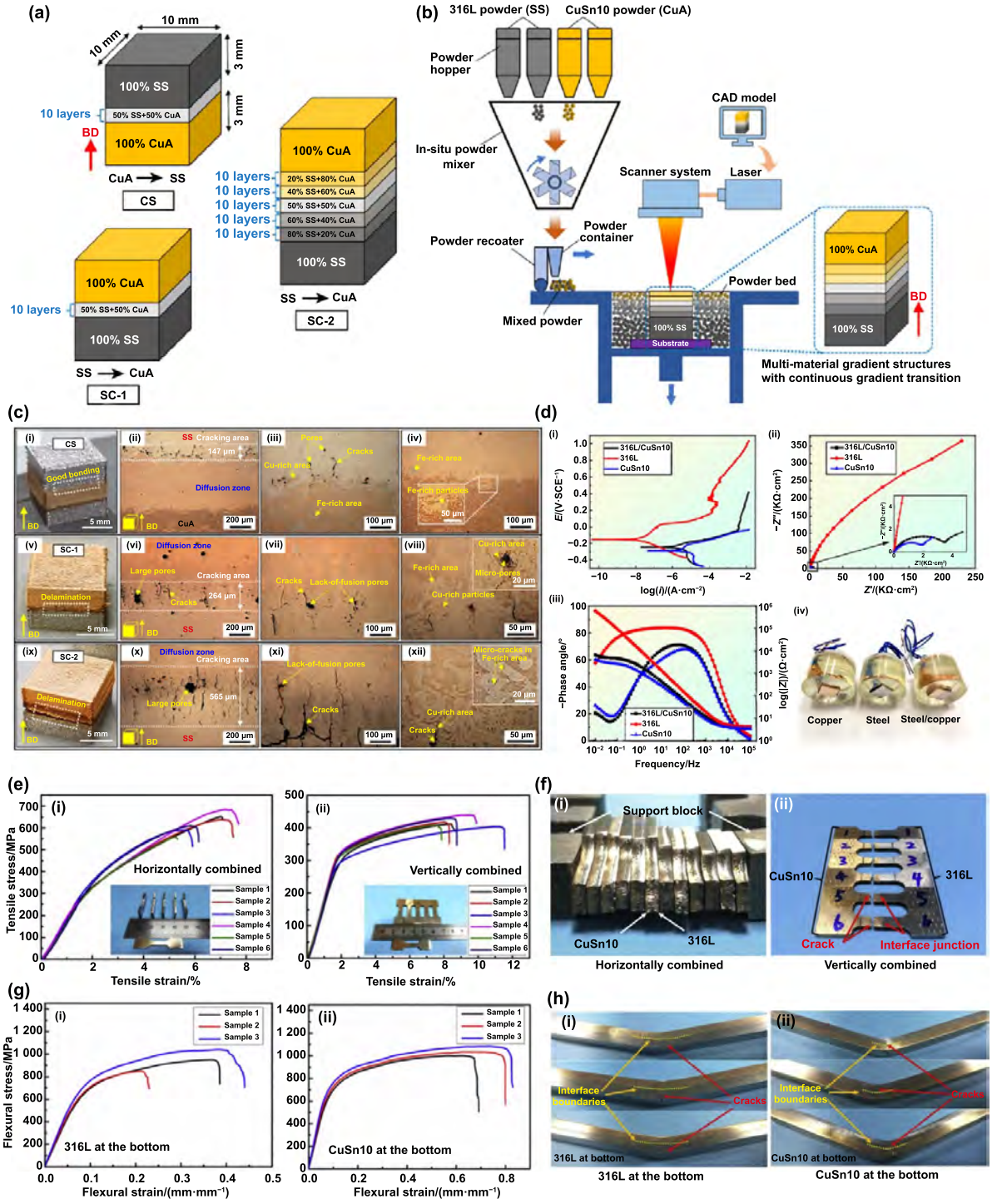

Figure 7. Process-structure-property in PBF of SS316L/CuSn10 MM. (a) Structural schematic and designation; (b) L-PBF system adapted to handle multi-materials; (c) fabricated parts in (a) and corresponding interfacial defects. Reprinted from[192], Copyright (2024), with permission from Elsevier. (d) EIS results of the base alloys and their bimetal combination. Reprinted from[193], Copyright (2024), with permission from Elsevier. (e) and (f) Tensile stress−strain curves of horizontal and vertical bimetals and fractured specimens, respectively; (g) and (h) flexural stress−strain curves of bimetals regarding alloys position and failed specimens, respectively. Reprinted from[194], Copyright (2020), with permission from Elsevier.

CS structure, although some interfacial cracks and porosities could still be observed, which were induced by the large difference in thermo-physical properties of the parent alloys.

Chen et al.[193] also confirmed the formation of liquid metal embrittlement (LME) microcracks in the L-PBF fabrication of a CuSn10/SS316L bimetal. They further found that exacerbated elemental segregation led to liquid phase separation (LPS) and a sudden change in the grain size because the high thermal conductivity of the Cu alloy aggravated the galvanic corrosion at the interfacial zone of the CuSn10/SS316L

bimetal. The Tafel, Nyquist, and Bode curves in Figure 7(d) from the electrochemical impedance spectroscopy (EIS) altogether display the reduced corrosion resistance of the CuSn10/SS316L bimetal compared to SS316L and close to CuSn10. In another study, researchers investigated the tensile and flexural behaviour of CuSn10/SS316L bimetal fabricated by L-PBF, considering its interfacial characteristics[194]. As shown in Figure 7(e), the UTS and elongation of the horizontally combined bimetals recorded higher values compared to the vertically combined ones with the fracture location on the weakest side, i.e., CuSn10, as determined in Figure 7(f). In contrast, the flexural strengths were similar regardless of which alloy was positioned at the bottom (Figure 7(g)). No macrocracks appeared along the interface of the failed bending specimens in Figure 7(h). Both mechanical behaviours indicated good interfacial bonding owing to desirable materials intermixing by an effective flow in the melt pools and refined grains by remelting and recrystallization.

Moreover, recent advancements in multi-material powder bed fusion via L-PBF have enabled the fabrication of compositionally heterogeneous metallic parts with voxel-wise material distribution across all three spatial dimensions (x, y, z). This capability represents a significant improvement in additive manufacturing, allowing the creation of FGMs with tailored local properties such as thermal conductivity, electrical conductivity, and mechanical strength within a single component. Novel systems, such as the selective powder deposition (SPD) recoater, facilitate the deposition of multiple powders in a single layer with a resolution as fine as 500 μm × 500 μm per voxel[195], enabling intricate material patterns without the need for assembly or joining processes.

Several material systems have been explored for voxel-based multi-material L-PBF, with 316L stainless steel and CuCrZr copper alloys being among the most prominently studied owing to their complementary properties: 316L offers high strength and corrosion resistance, whereas CuCrZr provides superior thermal and electrical conductivity[196]. Other combinations include 1.270 9 steel/CuCrZr, PA11/CuSn10[195], and M300 maraging steel/CuCrZr[197], each presenting unique interfacial characteristics and post-treatment responses. For instance, Meyer et al. indicated that direct age hardening (DAH) treatment at 500 °C for 1.5 hours increased the electrical conductivity of PBF-LB/M CuCrZr from ∼9.5 $MS{\cdot}m^{-1}$ to 33–35 $MS{\cdot}m^{-1}$ (∼250% improvement) and nearly doubled its hardness to ∼180 HV_{10}[196]. Significant differences arise depending on the build orientation: samples with 316L built on CuCrZr showed a thermal contact resistance as low as $\sim 5 \times 10^{-11}$ $m^2{\cdot}K{\cdot}W^{-1}$, indicating nearly ideal thermal bonding, whereas configurations with CuCrZr next to 316L exhibited higher resistance and more defects[196].

The family of ferrous alloys holds a distinguished reputation and plays an indispensable role in various industries because of their diverse mechanical properties. As a result, Fe-based MM structures are inevitable and have been highly esteemed in the literature. For instance, Bai et al.[198] studied the AM of maraging steel (MS1) on top of an as-cast CrMn steel, as shown in Figure 8(a), via the L-PBF process. According to Figure 8(b), the CrMn/MS1 MM showed higher tensile strength than cast CrMn steel and greater elongation than printed MS1. The final fracture occurred within the CrMn steel side, far away from the interface. The excellent mechanical performance of the hybrid MM structure was derived from strong metallurgical bonding with no defects, such as pores, inclusions, or cracks, as well as effective materials mixing under Marangoni convection at the interface zone. Errico et al.[19] expanded the capability of L-PBF to intralayer MM fabrication (i.e., two materials in a single layer), employing an ad-hoc planar divider into the powder platform to produce SS316L/18Ni (300) maraging steel bimetals, as presented in Figure 8(c). The EBSD characterizations from the interfacial region in Figure 8(d) indicate that this novel approach could affordably lead to a robust intralayer interface with an intermixing of the two-phase matrices instead of a distinct line between the two materials and no traces of porosity, cracks, or brittle intermetallic phases. This approach was further developed by Guo et al.[199] to produce intralayer FGM, as illustrated in Figure 8(k), featuring a powder hopper with a diagonal partitioner.

Recent research has expanded the application of MM-PBF beyond the primary Z-direction interfaces that were previously documented. Griffis et al. demonstrated that the build orientation and scan vector control in the LPBF of 904L/Bronze significantly affect the crack density and tensile strength at horizontal joints, with optimized hatching resulting in <0.2 mm^{-2} cracks and approximately 92% strength retention compared with those of bulk alloys[201]. Li et al. demonstrated that a 40–60 μm laser-offset strategy enabled strong in-plane bonding between Cu and Ni, achieving shear strengths of up to 185 MPa[202]. Guo et al. utilized an inclined dual-hopper recoater to produce continuous in-plane Invar36/316L FGM, resulting in less than 3% porosity throughout the lateral gradients[199]. The advancements from 2024 to 2025 built upon the previously discussed endeavors, demonstrating that MM-AM now encompasses vertical, horizontal, and hybrid interfaces, facilitated by auxiliary energy sources and adaptive powder delivery, which enables precise control of the structure and properties.

Elsewhere, an open-architecture L-PBF system utilizing two powder reservoirs with vibratory dosing units (Figure 8(e)) was employed to fabricate a multilayer SS316L/440C steel MM, as drawn in Figure 8(f). The 3D and cross-sectional 2D X-ray computed tomography (XCT) images in Figure 8(g) reveal the band structure (316L-rich in white and 440C-rich in blue) caused by their different Ni contents and defect morphologies, which represent a lack of fusion porosities, and numerous cracks mostly parallel to the building direction (BD), which were formed at the 440C/316L transitional (diluted) regions and propagated through the SS316L band, as specified by yellow rectangles. The hot cracking mechanism was demonstrated by identifying long-chain elemental segregations along the grain boundaries in those regions. This is consistent with a higher susceptibility to hot cracking within the 25 wt%–50 wt% 440C composition range. This range was predicted by mathematical models of the total shrinkage strain during solidification and

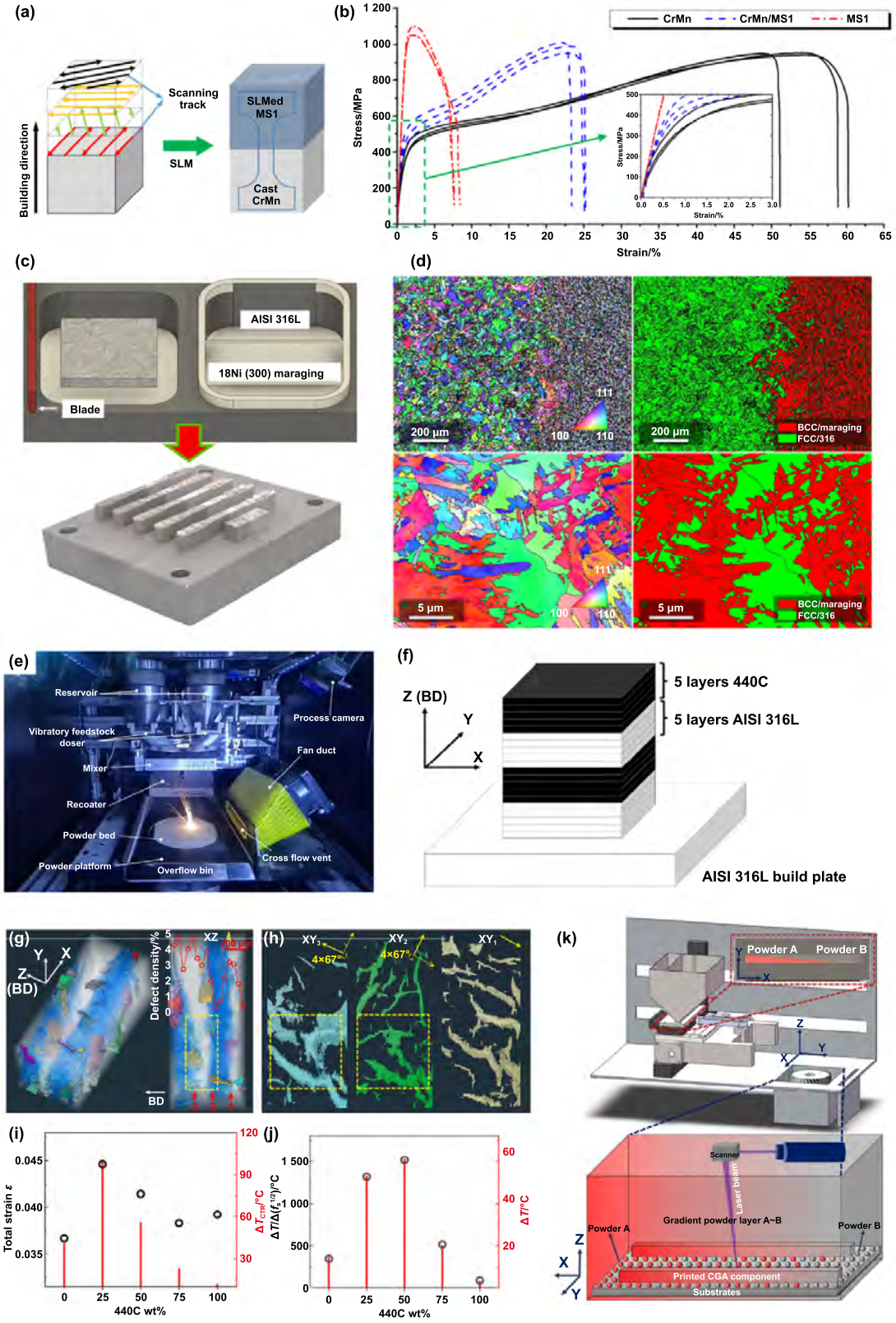

Figure 8. Process-structure-property in PBF of Fe-based MMs. (a) Schematic drawing of the scanning strategy and build-up MS1 on a CrMn steel substrate and (b) tensile test results of as-cast CrMn steel, as-printed MS1, and CrMn/MS1 MM. Reprinted from[198], Copyright (2021), with permission from Elsevier. (c) Implemented design on the L-PBF system to fabricate intralayer MM with realized parts and (d) IPF and phase maps from the interface of SS316L/18Ni (300) maraging steel MM. Reproduced from[19]. CC BY 4.0. (e) and (f) Chamber view of a customized MM L-PBF machine, and structure design; (g) and (h) XCT results revealing the band structure and internal defects; (i) and (j) total strain and hot cracking susceptibility for different compositions of SS316L/440C steel MM. Reproduced from[200]. CC BY 4.0. (k) Schematic of a newly developed L-PBF system providing printing intralayer continuous gradient MM. Reprinted from[199], Copyright (2024), with permission from Elsevier.

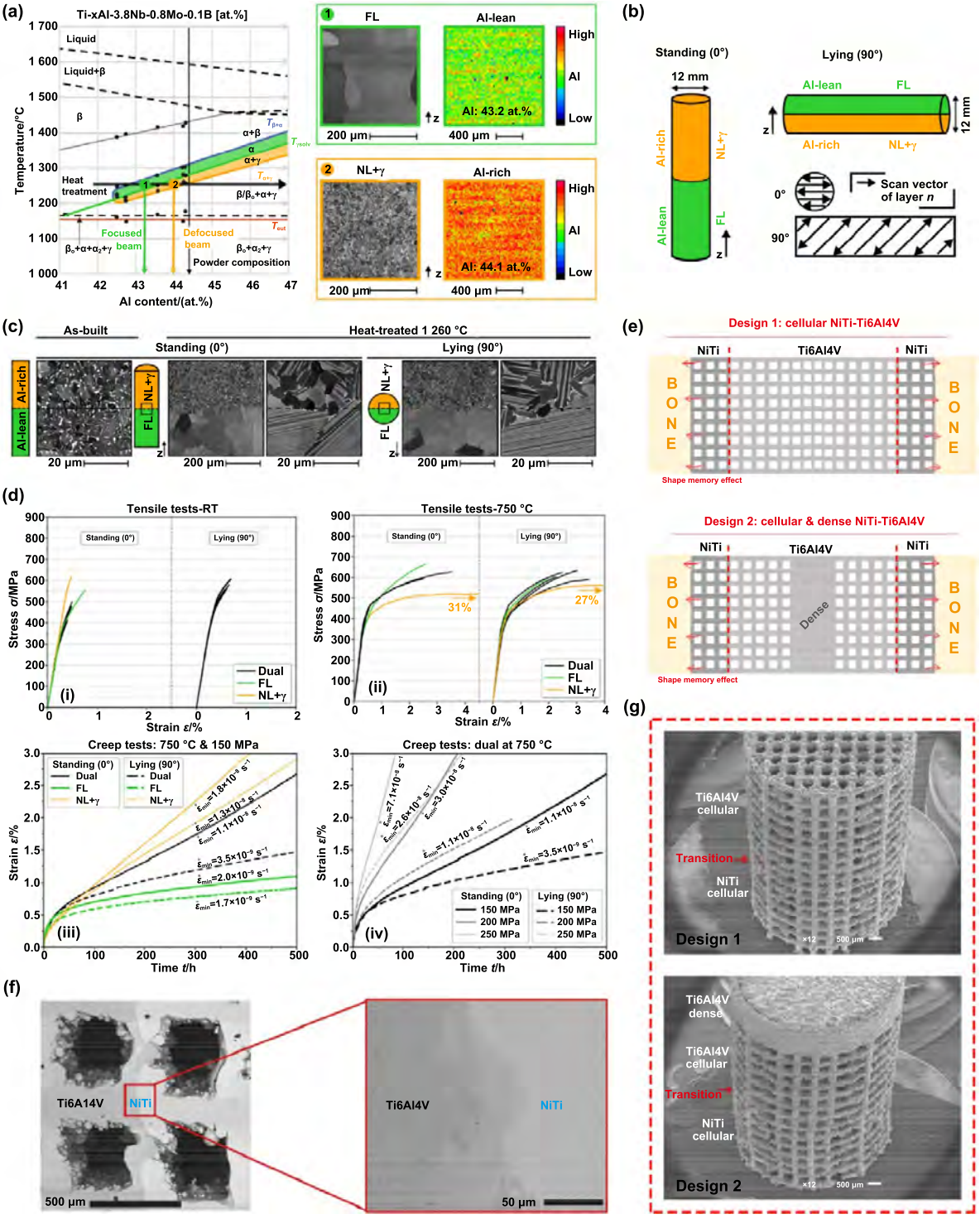

Figure 9. Process-structure-property in PBF of Ti-based MMs. (a) Phase diagram of the Ti-xAl-3.8Nb–0.8Mo-0.1B alloy system illustrating the dual microstructure concept using focused and defocused beams in EB-PBF process in addition to the SEM + EPMA results of the two microstructures after heat treatment, (b) build orientation and scanning strategy of the dual cylinders, (c) SEM images of the as-built and heat-treated dual microstructures in standing and laying orientations, and (d) creep test results of the dual and single microstructure specimens. Reprinted from[204], Copyright (2023), with permission from Elsevier. (e) Structural designs, (f) and (g) SEM images of the cross-section and geometry of L-PBF fabricated NiTi/Ti6Al4V MM. Reprinted from[205], Copyright (2020), with permission from Elsevier.

hot cracking susceptibility, as shown in Figures 8(i) and (j), respectively[200].

Last but not least, Ti-based alloys are of great interest for MM-AM owing to the design freedom provided by AM technology (especially PBF) and the outstanding properties of this material group, including excellent specific strength and high durability in harsh environments, which make together an ideal opportunity for further development

of high-performance, lightweight structures, particularly those demanded in aerospace and biomedical applications. Regarding aerospace applications, Knörlein et al.[203,204] developed a groundbreaking FGM processing route by integrating a dual microstructure and varying mechanical properties in a single part made of a 4th generation TiAl alloy via the EB-PBF process followed by heat treatment. Considering the experimental phase diagram of the Ti-xAl-3.8Nb–0.8Mo-0.1B alloy system (Figure 9(a)), the concept was implemented by adjusting the beam focus (energy density) in the melting step, resulting in a change in the localized Al content through evaporation during the EB-PBF process. Following heat treatment at 1 260 °C for 1 h, the as-built microstructure with two different Al contents transformed into fully lamellar (FL) and nearly lamellar (NL + γ) microstructures, as demonstrated individually by scanning electron microscopy and electron probe microanalysis (SEM + EPMA) in Figure 9(a). The cylindrical dual microstructure specimens with two building orientations (Figure 9(b)) were studied and compared with single microstructure ones. SEM micrographs from the dual microstructure interface in Figure 9(c) indicate no layering effect, and a fine and uniform NL + γ microstructure with the β_0 phase (white areas) in the as-built state and a sharp transition from the FL microstructure in the Al-lean region to the NL + γ microstructure in the Al-rich region can be observed in the heat-treated specimens, regardless of the building orientation. However, the discrete interface did not negatively affect the mechanical properties of the dual microstructure specimens. As shown in Figure 9(d), their tensile and creep properties under different test conditions (tensile tests at room temperature and 750 °C; creep tests at 750 °C and stresses of 150, 200, and 250 MPa) fell between the properties of single microstructure specimens. Additionally, their failure consistently occurred in the weaker microstructure (FL during tensile loading and NL + γ during creep)[204]. Therefore, this concept can effectively upgrade TiAl turbine blades with high-strength root and creep-resistant airfoil sections. For biomedical applications, Bartolomeu et al.[205] proposed a cellular design of the NiTi/Ti6Al4V MM (Figure 9(e)), aiming at a multi-functional hip implant with customized stiffness, high wear resistance, and controlled volume change. They adopted a manual powder replacement strategy in the L-PBF process to realize the designed structures, as displayed in Figure 9(g). The interface assessment in Figure 9(f) revealed successful and high-quality bonding between parent alloys, which resulted in an average shear strength of 33 MPa, more than NiTi and less than Ti6Al4V strengths (25 < 33 < 47 MPa). However, further investigation is needed on post-heat treatment to induce the martensite phase in the NiTi section and enhance its shape-memory properties. At the end of this subsection, Table 3 summarizes various features of the studies conducted on multi-material PBF additive manufacturing.

4.3. Critical comparison of the PBF and DED of MMs

4.3.1. Gradient resolution and interface quality. A primary difference between PBF and DED in multi-material metal printing is the gradient resolution attainable at material interfaces. PBF methods, such as L-PBF, utilize thin powder layers measuring tens of microns, facilitating remarkably abrupt transitions between materials, frequently resulting in a distinct interface within one or two layers[192]. The typical layer thickness in PBF is 30–60 μm, resulting in interface widths of approximately 50–150 μm[224,249]. Compared with DED, this method can yield a more refined interface between two metals, indicating that compositional alteration occurs across a minimal distance. Nonetheless, these abrupt interfaces in PBF might be a double-edged sword; although they provide high-resolution material patterning, they frequently experience significant property mismatches and stress concentrations[250]. Research on PBF-fabricated bimetals (e.g., Inconel 718 to bronze) indicates that while a robust metallurgical connection is achieved, the transition zone remains exceedingly small, leading to potential cracking at the interface due to abrupt variations in composition and properties[194]. The interfacial region within these PBF builds is generally comparable to the layer thickness (tens of microns), exhibiting minimal diffusion or mixing. This results in a high gradient resolution but also increases the risk of brittle intermetallic phases or hot cracking if the two materials lack inherent compatibility. In fact, the majority of multi-material PBF experiments have directly bonded two dissimilar metals with minimal or no compositional grading, hence intensifying the interfacial thermal stresses[5].

In contrast, DED techniques (laser/wire-fed deposition) inherently produce a larger melt pool and facilitate a more gradual integration of one material into another. L-DED typically achieves deposition rates of 5–25 $cm^3 \cdot h^{-1}$ with melt-pool depths of 0.5–2 mm, whereas PBF is usually 2–10 $cm^3 \cdot h^{-1}$[251–254]. Conventional DED multi-material constructions produce FGM transitions by depositing successive layers with steadily varying compositions instead of a sudden interface[255]. This results in an extensive compositional transition zone, often ranging from hundreds of microns to millimeters, depending upon the deposition method employed. The gradient thickness in L-DED is usually 0.5–2 mm, whereas it is <0.15 mm for PBF[256]. The enlarged melt pool in DED facilitates the mixing of the two materials, hence refining the gradient at the interface. Consequently, the interface quality of DED FGMs frequently exhibits superiority in terms of metallurgical continuity, as abrupt property transitions may be mitigated by compositional tapering. In an L-DED deposit joining stainless steel to Inconel, a deliberately graded intermediate layer created a seamless compositional transition (1–2 mm thick) and eliminated the abrupt interface observed in a similar PBF build[257].

The trade-off is that DED exhibits a lower resolution of compositional change, resulting in a transition that cannot be confined as narrowly as in PBF. The deposited beads in DED are relatively large, resulting in gradient increments that are coarser than a single 50 μm powder layer, even with incremental adjustments to the feedstock. In practice, DED produces interfaces that are characterized by a "saw-shaped" or interlocking configuration resulting from bead overlap. The wavy interface geometry is advantageous because it facilitates mechanical interlocking between materials, thereby

Table 3. Summarized features of studies on multi-material PBF additive manufacturing.

Material groups	Parent materials	Designs	Processes[a]	Adaptive mechanisms	Reported defects	Studied properties	Referencess
Fe-Cu	SS316L/CuSn10 bronze	Bimetal	L-PBF	Two powder feeders outside the building chamber with powder flow regulators	Unmelted particles & cracking	Hardness, tensile, flexural	Chen et al.[206]
		Bimetal	L-PBF	Not mentioned	Porosity, unmelted particles, cracking	Hardness, tensile, flexural	Chen et al.[194]
		Bimetal	L-PBF	Two powder feeders outside the building chamber with powder flow regulators	Unmelted particles, liquid phase separation, liquid metal embrittlement, cracking	Hardness, tensile, corrosion	Chen et al.[193]
		FGM	L-PBF	Powder hoppers and an in situ powder mixer featuring rotating blades	Porosity, lack of fusion, liquid phase separation, liquid metal embrittlement, cracking, delamination	Hardness & shear	Liu et al.[192]
	SS316L/CuCrZr	Bimetal	L-PBF	Manual powder replacement	Unmelted particles & cracking	Hardness & tensile	Mao et al.[207]
		Bimetal	L-PBF	Printing CuCrZr powder on SS316L substrate	Porosity & cracking	Hardness & tensile	Kuai et al.[208]
		Bimetal	L-PBF (HIP)	A dual-material recoating unit with two rotating drums	Porosity, unmelted particles, cracking	Hardness	Deillon et al.[209]
		Bimetal	L-PBF	Consecutive printing and cleaning	Porosity & cracking	None	Martendal et al.[210]
	SS316L/C18400 Cu alloy	Bimetal	L-PBF	Rotating powder chambers and a center separator in the recoater	Porosity, unmelted particles, cracking	Hardness & tensile	Liu et al.[211]
	SS316L/C52400 Cu alloy	Layered	L-PBF	Manual powder replacement	Porosity, oxidation, cracking	Hardness	Bai et al.[212]
	C300 maraging steel (MS)/T2 Cu alloy	Bimetal	L-PBF	Printing MS powder on Cu alloy substrate	Porosity, lack of fusion, cracking	Tensile, flexural, fatigue	Tan et al.[213]
	Invar36/Cu10Sn	Mixed compositions	L-PBF	An ultrasonic powder dispensing array	Porosity, lack of fusion, unmelted particles, cracking	None	Wei et al.[214]

(Continued.)

Table 3. (Continued.)

Material groups	Parent materials	Designs	Processes[a]	Adaptive mechanisms	Reported defects	Studied properties	Referencess
Fe-Ni	SS316L/IN718	Bimetal	EB-PBF	Printing SS316L powder on IN718 substrate, and vice versa	Porosity, unmelted particles, Cracking	Hardness	Hinojos et al.[215]
		Layered	L-PBF	Manual powder replacement	Porosity, unmelted particles, cracking	Hardness & tensile	Mei et al.[216]
		Bimetal	L-PBF	Printing IN718 powder on SS316L substrate	Keyhole porosity & cracking	Hardness	Chen et al.[217]
		Layered	L-PBF	A multiple powder dispensing and cleaning system	Lack of fusion	Hardness	Yusuf et al.[218]
		FGM	L-PBF (PHT)	In-process alternating material layers using a dual powder recoater	Porosity, lack of fusion, cracking	None	Wits and Amsterdam[219]
		Bimetal	L-PBF	Manual powder replacement	Lack of fusion & cracking	Hardness, tensile, fatigue	Duval-Chaneac et al.[220]
		FGM	L-PBF (PHT)	A custom blade-based gradient powder recoater	None	Hardness & tensile	Wen et al.[221]
		Bimetal	L-PBF	A partitioning blade in the powder chamber	Cracking	Hardness	Errico et al.[222]
		Bimetal & FGM	L-PBF	Standard L-PBF system loaded with inverse gradient powder	Porosity	Tensile	Ghanavati et al.[31,223]
	SS316L/Hastelloy X	Bimetal	L-PBF	Manual powder replacement	Porosity & inclusion	Tensile, flexural, roughness	Rankouhi et al.[224]
		Bimetal	L-PBF	Manual powder replacement	Porosity, lack of fusion, unmelted particles	Hardness & tensile	Fan et al.[131]

(Continued.)

Table 3. (Continued.)

Material groups	Parent materials	Designs	Processes[a]	Adaptive mechanisms	Reported defects	Studied properties	Referencess
Fe-based	SS316L/H13 tool steel	Layered	L-PBF	An inlay for the shaft recoater alternating inline material dispensing	Porosity & oxidation	Hardness & tensile	Hengsbach et al.[225]
	Maraging steel (MS1)/H13 tool steel	Bimetal	L-PBF (PHT)	Printing MS1 powder on H13 substrate	None	Hardness & tensile	Shakerin et al.[226]
	Maraging steel (MS1)/CrMn steel	Bimetal	L-PBF	Printing MS1 powder on CrMn steel substrate	None	Hardness & tensile	Bai et al.[198]
Fe-based	SS316L/Fe35Mn steel	FGM	L-PBF	A double hopper and a mixing chamber	Porosity & lack of Fusion	Hardness & tensile	Demir et al.[227]
	SS316L/18Ni (300) maraging steel	Bimetal	L-PBF	A planar divider into the powder chamber	None	Tensile	Errico et al.[19]
	SS316L/SS17-4 PH	Bimetal lattice	L-PBF (PHT)	A partitioning system within the powder supply	Porosity, lack of fusion, oxidation, surface roughness	Compressive & tensile	McDonnell et al.[228]
	Invar36/SS316L	FGM	L-PBF	A powder hopper with a partition along its longer diagonal serving individual spaces for filling powders	Porosity	Hardness, tensile, thermal expansion, corrosion	Guo et al.[199]
	SS316L/440C steel	Layered	L-PBF	Separate powder hoppers with two vibratory dosing units and a mixer	Lack of fusion & cracking	Hardness	Pan et al.[200]

(Continued.)

Table 3. (Continued.)

Material groups	Parent materials	Designs	Processes[a]	Adaptive mechanisms	Reported defects	Studied properties	Referencess
Ti-based	Ti6Al4V/TiB_2	Bimetal	L-PBF	An automatic system for powder delivery (no more details)	Porosity & cracking	Thermal behaviour	Chen et al.[229]
	NiTi/Ti6Al4V	Bimetal	L-PBF	Manual powder replacement	None	Hardness & shear	Bartolomeu et al.[205]
	Ti6Al4V/Ti2AlNb	Bimetal	L-PBF (PHT/HIP)	Manual powder replacement	Cracking	Hardness & tensile	Polozov et al.[230]
	Ti-xAl-3.8Nb-0.8Mo-0.1B ($TiAl_x$)	Bimetal	EB-PBF (PHT)	Controlling localized aluminum evaporation	Porosity & misconnection	Hardness, tensile, creep	Knörlein et al.[204]
	TiAl/Ti6Al4V	Layered	L-PBF	Two containers mounted on the build chamber to supply powders separately	Porosity & cracking	Tensile	Shi et al.[231]
(X)-Al	C18400 Cu alloy/AlSi10Mg	Bimetal	L-PBF	A hopper and a powder separator in the recoater	Porosity, unmelted particles, cracking	Hardness, tensile, flexural	Sing et al.[232]
	Fe/Al-12Si	FGM	L-PBF	A double-hopper and a mixing chamber	Porosity, lack of fusion, cracking	Hardness	Demir and Previtali[233]
	Ti6Al4V/AlSi10Mg	Bimetal	L-PBF	Manual powder replacement	Porosity, lack of fusion, cracking	Tensile	Wu et al.[234]
	Ti/Al6061	FGM	L-PBF	Two powder feeders and a mixing container	Balling, unmelted particles, lack of fusion, cracking	Hardness & tensile	Daram et al.[235]
	SS316L/AlSi10Mg	Bimetal	L-PBF	Rotating chambers in the multiple powder deliverer	Lack of fusion, keyhole porosity, cracking	Hardness & tensile	Miao et al.[236]
(X)-W	SS316L/W	Bimetal	L-PBF (PHT)	Not mentioned	Porosity, unmelted particles, cracking	Hardness & tensile	Zhou et al.[237]
	CuSn10 bronze/W	Bimetal, FGM, interlayer (SS316L)	L-PBF	An ultrasonic-assisted multi-material powder deposition device	Porosity, unmelted particles, cracking, delamination	Hardness	Wei et al.[188]
	Ti6Al4V/W	Bimetal	L-PBF	Manual powder replacement	Porosity, unmelted particles, cracking	Hardness, compressive, flexural	Wu et al.[238]
	ODS-SS316L/W	Bimetal	L-PBF	Manual powder replacement	Porosity, unmelted particles, cracking	Nanoindentation & tensile	Xie et al.[239]

(Continued.)

Table 3. (Continued.)

Material groups	Parent materials	Designs	Processes[a]	Adaptive mechanisms	Reported defects	Studied properties	Referencess
Others	Ti/Hydroxyapatite (HA)	FGM	L-PBF	Not mentioned	Porosity & cracking	Hardness, compressive, fracture toughness	Han et al.[240]
	Cu10Sn bronze/ Soda-lime glass	FGM	L-PBF	A powder-mixing and vibrant feeding system	Porosity & cracking	Hardness, tensile, shear	Zhang et al.[241]
	Mo/TiC	FGM	EB-PBF	Secondary material (Mo + TiC) feeding in a custom-built chamber	Porosity	None	Rock et al.[242]
	SS316L/Cu alloy/Ti6Al4V	Interlayer	L-PBF	Manual powder replacement	Porosity, cracking, delamination	Hardness & tensile	Tey et al.[243]
	SS316L/NiTi	Bimetal	L-PBF	Printing NiTi powder on SS316L substrate	Surface porosity and roughness, cracking	None	Ekoi et al.[244]
	SS316L/Ti	Mixed composition	L-PBF	Pre-mixed powder feedstock	Porosity	Nanoindentation & tensile	Xu et al.[245]
	Ti6Al4V/IN718	FGM	L-PBF	Double hopper and a mixing chamber	Lack of fusion & cracking	Hardness	Scaramuccia et al.[246]
	Ti6Al4V/Cu10Sn bronze	Bimetal & FGM	L-PBF	An ultrasonic-assisted multiple powder dispensing function	Porosity, unmelted particles, cracking, delamination	Hardness & shear	Wei et al.[247]
	Ni/Ti	FGM	L-PBF	Two powder hoppers and a mixing container	Cracking	Hardness	Daram et al.[248]

[a] PHT: post-heat treatment, HIP: hot isostatic pressing.

improving the interfacial strength[258]. Studies indicate that the interfacial macro-profile of DED, characterized by a comb-like morphology with layers of one material extending into another, enhances the shear strength at the bond by effectively interlocking the two materials[259]. Consequently, PBF provides a distinct, flat interface, whereas DED results in a non-uniform yet stronger metallurgical bond due to mixing and interlocking of the materials.

The differences in microstructure between rapid solidification in PBF and slower cooling in DED have a significant impact on interface quality. The typical cooling rates are 10^5–10^6 K·s^{-1} for PBF, 10^3–10^4 K·s^{-1} for L-DED, and $\sim 10^2$ K·s^{-1} for WA-DED[260–262]. The high cooling rates of PBF (10^5–10^6 K·s^{-1}) result in very fine microstructures at the interface, frequently exhibiting fine cellular or dendritic structures and occasionally leading to the formation of metastable phases[263]. DED, characterized by a larger melt pool (typically 0.5–3 mm wide), generally produces coarser grains—often columnar with widths of 50–200 μm and lengths up to 0.5–1 mm—growing through successive layers. In contrast, the finer melt pools of PBF (∼80–150 μm) yield equiaxed or cellular grains that were usually <10 μm[264,265]. In multi-material structures, this variation can be significant. In a hybrid deposition study, an L-DED functionally graded material zone displayed fine equiaxed dendrites at the interface. In contrast, a slower WA-DED region showed coarse columnar grains extending from the interface[257].

By extension, a PBF-built interface would be expected to have an even finer microstructure than L-DED, potentially enhancing hardness and strength locally. However, the fine microstructure of PBF is accompanied by increased residual stresses (due to rapid cooling) and often the formation of brittle intermetallic compounds at a sharp interface, which can reduce the overall interface toughness. The DED mixed interface may dilute such intermetallics but can also create a wider heat-affected zone where microstructural coarsening or secondary phase formation (e.g., eutectic mixtures) occurs[194]. The porosity levels are often <0.05% for optimized L-PBF builds, whereas well-controlled DED shows 0.2%–0.8% and WA-DED may exceed 1% if the shielding or feedstock quality is poor[266,267].

However, numerous studies have revealed that DED creates coarser as-built surfaces than PBF due to its bigger melt pool and thicker deposited tracks. L-DED and WA-DED typically have roughness of Ra ≈ 20–50 μm (and up to 200 μm for WA-DED), whereas optimized L-PBF typically achieves Ra ≈ 5–15 μm, with some reports as low as ∼3–6 μm after parameter tuning. DED's rougher topography frequently requires machining, grinding, or polishing to achieve functional surfaces or fatigue-critical finishes, whereas PBF parts can often meet moderate surface requirements directly, requiring only light blasting or chemical smoothing. Dimensional precision is another advantage of PBF[268].

It is worth noting that L-PBF maintains tolerances of ±0.05–0.15 mm for medium-sized components, with minimal feature sizes of ∼0.1–0.2 mm. The DED precision is limited to ±0.25–0.5 mm for L-DED and ±1 mm for WA-DED, depending on the part size and thermal distortion[269,270]. Even with process monitoring and path optimisation, DED cannot match PBF's fine detail or repeatability without substantial finish machining. This gap is particularly significant for thin-wall or lattice portions in multi-material structures, where geometric accuracy is crucial[271].

4.3.2. Material compatibility and residual stresses in dissimilar metals. The rapid melting and solidification of PBF, as well as its lack of in situ compositional blending, make it relatively less forgiving when working with highly dissimilar metals. In multi-material PBF builds, cracking at the interface is common when joining materials with mismatched thermal properties. For example, joining a high-temperature nickel superalloy to a copper alloy by PBF led to cracks propagating in the steel side of the interface, which was attributed to the high residual tensile stress in the rapidly cooled steel and the segregation of elements at the sharp interface. Indeed, analyses of L-PBF bimetallic samples (316L stainless steel to CuSn10 bronze, Inconel 718 to Cu alloy, etc.) have reported that cracks inevitably appear at abrupt interfaces owing to the significant differences in the thermophysical properties (thermal expansion and thermal conductivity) of the two alloys[194].

Recent studies on multi-material L-PBF have explored strategies to mitigate interfacial defects in dissimilar metal combinations. Fan et al. demonstrated that rapid cooling in L-PBF reduced element segregation, resulting in crack-free interfaces between 316L steel and Hastelloy X[131]. Liu et al. introduced a composition gradient at the interface between CuSn10 and 316L steel, which improved bonding by minimizing the stress concentration[192]. Mao et al. used finite element modeling and reported that higher scanning speeds led to increased residual stress at the CuCrZr/316L interfaces, causing cracks[272]. Liu et al. compared different building strategies for CuSn10/316L structures and reported that printing 316L on CuSn10 resulted in a wider diffusion zone and better bonding than the reverse order[273].

DED, in contrast, offers a greater number of strategies for managing incompatibilities. It is possible to deposit transition layers or compositionally graded interlayers specifically to ameliorate metallurgical incompatibility due to its capacity to modify feedstock composition on the fly. For instance, a DED process can initially deposit a thin layer of an intermediate alloy to act as a compatible bridge if the direct deposit of material A on material B would result in the formation of brittle intermetallics[79]. This methodology has demonstrated profound enhancements in the quality of dissimilar metal joints in experimental studies. By incorporating a functionally graded Fe–Ni buffer layer into the steel–Inconel DED construct, the tensile strength of the bimetal was enhanced by more than 50% in comparison to that of an acute interface without grading[194]. Another study utilized laser deposition and wire-arc AM to join stainless steel 304L to Inconel 625, utilizing a graded layer that was deposited via DED. The resulting bimetallic structure was robust and withstood tensile loading, with a strength that was approximately 8% greater than that of a control sample that lacked a graded layer[257]. Figure 10 clearly illustrates this

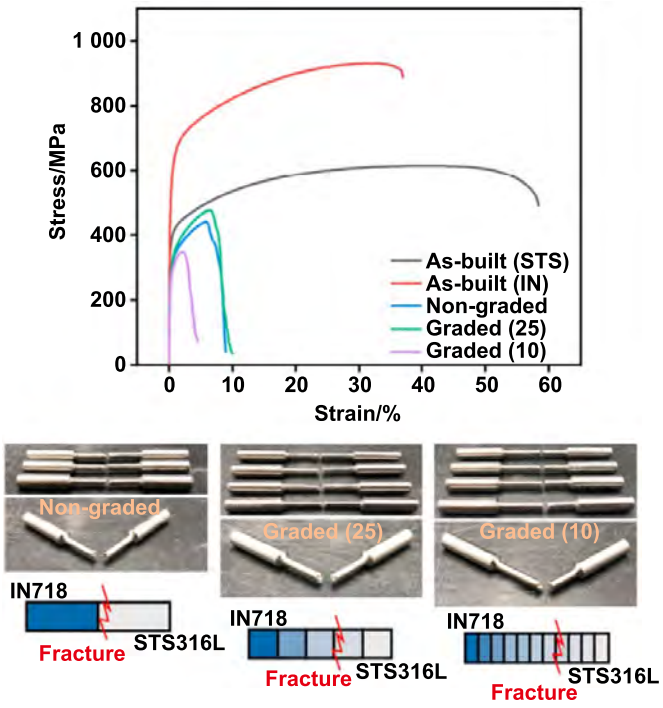

Figure 10. Comparison of tensile behaviour and fracture locations in DED-fabricated Inconel 718–316L stainless steel joints with and without a functionally graded Fe–Ni buffer layer. Reprinted from[274], Copyright (2022), with permission from Elsevier.

improvement. The stress−strain curves show that the non-graded interface failed prematurely at the joint, whereas both graded samples (with 10- and 25-layer transitions) exhibited significantly higher tensile strength and delayed fracture. The corresponding fracture locations indicate improved load distribution and enhanced interface toughness in the graded configurations.

L-DED provides significant compositional flexibility for graded interface design, whereas L-PBF facilitates interlayer and gradient transition strategies. Demir et al. demonstrated a smooth gradient structure in L-PBF by progressively altering the steel-Mn content in an AISI 316L/Fe-35Mn system, resulting in a diffusion zone of approximately 100–200 μm, which exhibited an enhanced hardness transition at the interface[227]. Griffis et al. demonstrated that build orientation has a significant influence on interfacial defect formation. In their study on MM-LPBF for 904L stainless steel and bronze, they found that orienting the interface plane relative to the powder recoater blade decreased the crack density by approximately 30%–50% and increased the interface strength[201]. Dzogbewu and de Beer examined powder delivery systems, including ultrasonic, blade, and mixed feeders, to address interlayer transitions and minimize defects in L-PBF multimaterial components[275]. The results indicate that while PBF gradients and interlayers typically exhibit limited thickness and require stricter control, they have been observed and can partially bridge the gap with L-DED in interface engineering.

Extremely dissimilar material combinations (e.g., combinations of metals far apart on the periodic table) remain challenging for both processes, but currently, DED has demonstrated success in some cases where PBF has yet to do so[251]. For instance, joining steel to aluminum in a single build is completely challenging in PBF; the two powders would contaminate each other, and the extreme differences in melting temperature and reactivity would cause severe defects[276]. DED, by contrast, has been used to directly deposit one metal onto another (steel or aluminum) in a controlled way, effectively combining traditional methods[181]. These dissimilar joints via DED are far from trivial—they often require precise process tuning or filler layers—but the fact that different feedstocks can be fed sequentially makes it feasible.

In summary, in regard to material compatibility, PBF requires either compatible material pairs or clever post-processing to succeed. In contrast, DED offers more process flexibility for grading or buffering dissimilar metals, albeit at the cost of potentially larger mixed zones and increased heat input. Each approach to multi-material joining must be tailored to the specific metal pair and use-case requirements (strength, corrosion, etc.), and often, the best results involve hybrid strategies (e.g., using DED to lay a graded layer that is then built upon by PBF, or vice versa).

While Sections 4.3.1 and 4.3.2 focused on PBF and DED as stand-alone routes, recent work has shown that combining the two processes in a single workflow can unlock unique advantages for MM fabrication.

Recent case studies illustrate the advantages of hybrid PBF–DED fabrication for MM metal structures. Bettencourt et al. demonstrated the production of bimetallic specimens by additively bonding Inconel 625 to a 316L stainless steel base, which was prefabricated via L-PBF. The hybrid-built components demonstrated tensile properties that surpassed those of individual materials. Specifically, the yield strength of the multi-material joint was greater than that of both monolithic 316L and IN625, whereas its UTS was comparable to that of a pure IN625 alloy. The interface design is critical: a direct transition from stainless steel to IN625 resulted in a ductile bond without interfacial cracking, whereas the introduction of a 50/50 mixed alloy intermediate layer (approximately 0.6 mm thick) caused brittle fracture at the joint. Microscopic analysis revealed microcracks within the mixed transitional layer, whereas the direct as-printed interface remained intact. The results indicate that optimized transition strategies, such as minimizing excessive dilution or oxides at the interface, are essential for achieving high-strength, reliable bonds in hybrid multi-material components[277].

In addition to improving mechanical strength, hybrid MM-AM can improve functional properties, including thermal performance. A recent multi-material study on stainless steel 316L and CuCrZr copper alloy demonstrated that building steel on top of a copper section resulted in a significantly lower thermal contact resistance at the interface than the reverse configuration. A 316L-on-Cu structure demonstrated superior heat transfer efficiency across the bimetallic junction compared to a Cu-on-316L structure. This finding suggests that the careful selection of material combinations and their sequences can improve the interface quality for thermal management. In a hybrid PBF–DED framework, one could utilize this approach

by, for instance, fabricating a complex copper heat exchanger core through PBF and subsequently employing DED to clad or attach it to a steel housing or support. The quantitative enhancement in thermal interface conductance, indicated by reduced contact resistance, observed in the 316L/CuCrZr case, highlights the ability of hybrid AM to produce MM components that are optimized for both structural and thermal performance, a feat that is frequently unachievable with a single-material approach[278].

Comparative studies demonstrate that hybrid PBF–DED strategies can surpass single-process multi-material builds in terms of interface integrity and overall performance. All-DED multi-metal builds, although advantageous for material mixing, typically necessitate functionally graded transitions to alleviate thermal stresses. However, despite the implementation of grading, they often exhibit interfacial cracking and mechanical properties inferior to those of monolithic alloys[182]. For instance, DED-fabricated 316L–Inconel samples exhibiting different compositional gradients did not attain tensile strengths exceeding those of single-material 316L and generally failed at elongations below 10%, in contrast to approximately 30% or more for wrought steel, which was attributed to brittle interface behaviour. The hybrid 316L/IN625 components demonstrated a joint strength exceeding that of the weaker base metal and an elongation comparable to that of the more ductile alloy, despite the abrupt material transition[277]. This hybrid synergy, which combines PBF's precision and material quality with DED's multi-material flexibility, presents distinct advantages over single-process methods. It facilitates the production of multi-material metal components that exhibit improved mechanical and functional performance, which is supported by measurable enhancements in the interface quality and overall part behaviour.

4.3.3. Material utilization, forming capabilities, and part complexity. In multi-material frameworks, the unused powder from PBF may typically be recycled; nevertheless, the combination of incompatible powders raises concerns. Cross-contamination across several powders may necessitate the disposal of unwanted material instead of recycling it[279]. Consequently, although single-material PBF typically attains high material utilization (approximately 95% efficiency in practice, compared with an idealized 100%), multi-material PBF generally exhibits less effective utilization because of the segregation or collection of mixed powders. Specialized methodologies, such as distinct powder compartments or sheet-based powder distribution systems, are being investigated to mitigate these issues and ensure material recycling[279]. The material consumption of DED fluctuates based on the type of feedstock. WA-DED exhibits remarkable efficiency, with approximately 100% of the wire being melted directly into the component, resulting in minimal waste[280]. In L-DED, there is material loss due to powder that fails to reach the melt pool, referred to as "overspray". Under optimal conditions, powder DED can achieve approximately 80% material utilization; however, in suboptimal scenarios, the catch efficiency may decline (for instance, high-speed powder DED has been reported to yield only 50%–70% efficiency owing to powder rebound and kinematic losses)[281]. Crucially, for MM-DED, the transition between materials can be achieved by either exchanging or blending feedstock in real-time, resulting in negligible transitional waste. DED is appealing for FGM fabrications as it may deposit costly or heterogeneous elements exclusively where required, hence optimizing material usage[282,283].

With respect to design freedom, PBF has exceptional geometric design flexibility within its build volume, allowing complex geometries and overhangs to be supported by the surrounding powder. Nonetheless, its capacity for formation in a multi-material context is limited by the process configuration[284]. In PBF, various ingredients must be either pre-mixed or supplied via several feed systems layer-by-layer, significantly limiting the introduction of a secondary material. Contemporary PBF machines necessitate customised adjustments (e.g., multiple hoppers or localized powder deposition mechanisms) to incorporate two alloys within a single layer or component; in the absence of such enhancements, material alterations can only occur at specified layers or locations[277]. This finding indicates that although PBF can produce high-precision multi-material components, the placement and alignment of different materials are restricted by the characteristics of the powder recoating process. PBF is constrained by a predetermined chamber size, rendering it incapable of accommodating excessively large or non-planar geometries. PBF offers significant geometric freedom for intricate designs, although it gives little operational flexibility for the arbitrary addition of materials during fabrication[285].

On the other hand, DED is distinguished by significant process flexibility, sometimes referred to as high forming freedom, which is particularly advantageous for MM-AM[286,287]. DED machines can interchange or combine materials on demand and deposit them onto pre-existing components, as the material is supplied through nozzles or wire feeders. This facilitates the construction of a variety of component sizes, including substantial elements, and in several orientations. For example, multi-axis DED machines can mount a deposition head on a robotic arm or gantry, allowing material to be laid on curved surfaces or repaired in situ on damaged components. This capability allows a DED process to incorporate a secondary alloy as a coating, internal layer, or graded transition at virtually any stage of a build. Furthermore, DED is not restricted to a defined space; the construction area is solely constrained by the motion mechanism, rendering it appropriate for extensive structures that exceed the built volume of PBF[277]. The trade-off is that DED typically cannot produce unsupported overhangs or intricate internal cavities as easily as PBF; without a powder bed, features such as fine internal channels or delicate thin walls are harder to form and often require support strategies. In summary, for MM-AM, DED offers greater freedom to place and transition materials throughout a part (and to do so on a larger scale), whereas PBF is more constrained in material placement but excels at intricate shape creation within a smaller envelope[186,275]. Figure 11 summaries

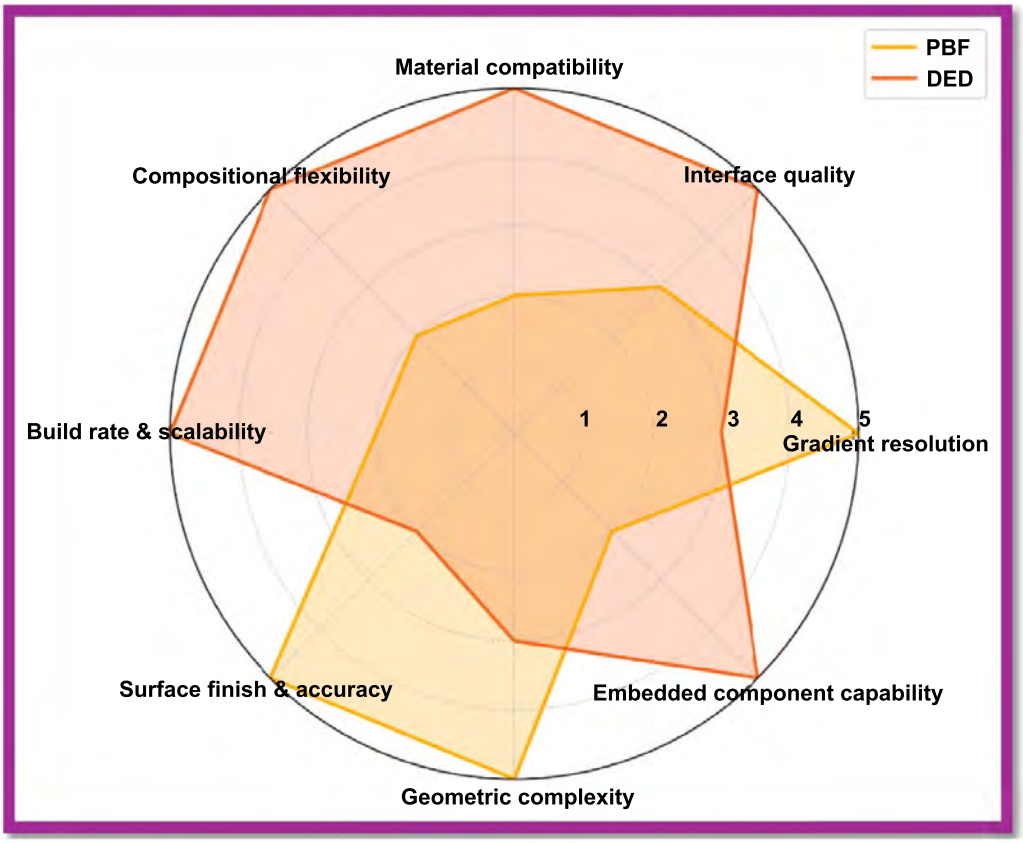

Figure 11. Radar chart comparing PBF and DED across eight key attributes relevant to MM-AM.

the comparative performance of PBF and DED across critical factors in multi-material AM.

4.4. Heat-treatment strategies for MM-AM components

The heat treatment of MM-AM parts is a critical and intricate process, as each alloy within a joint or gradient exhibits a distinct thermomechanical response. Various strategies have been proposed in the literature to address these requirements[288]. An initial strategy involves implementing a compromise (single-furnace) cycle that promotes strengthening in high-temperature alloys while preventing excessive softening or oxidation of the counterpart. Yan et al.[103] demonstrated that in SS316L/IN718 functionally graded materials produced by L-DED, solutionizing at 1 080 °C for 0.5 hours followed by aging at 720 °C for 4 hours resulted in finer equiaxed grains in SS316L and γ'/γ'' re-precipitation in IN718, leading to enhanced tensile strength and wear resistance compared with both the as-built condition and a milder heat treatment schedule[109]. In contrast, sharp PBF bimetals such as SS316L/CuSn10 are unable to endure elevated temperatures. Research indicates that intense thermal cycles exacerbate liquid−metal embrittlement and galvanic corrosion at the abrupt interface, thus restricting their application to low-temperature stress relief or mild HIP[193,289].

On the other hand, the sharp transition between dissimilar materials creates residual stresses from temperature gradients, leading to crack formation at the bonded interface[289]. While stress relief annealing at 400°C shows slight improvements in corrosion resistance of the 316L/CuSn10 systems, the treatment parameters require careful optimization to accommodate both materials simultaneously[290]. Similar challenges occur in IN718/CuSn10 joints, where significant differences in thermophysical properties inevitably produce interfacial cracks despite good metallurgical bonding, resulting in reduced elongation and interface-dominated fractures[291].

A secondary strategy involves sequential or zonal HT facilitated by interlayers. Park et al. incorporated V/Cr/Ni transition foils between Ti6Al4V and IN718, facilitating a two-stage treatment: stress relief for the titanium side and aging for the nickel-based superalloy. EBSD maps verified the absence of intermetallic compounds during bonding, and the tensile strength improved from approximately 210 MPa under the as-built condition to approximately 250 MPa following the tailored sequence[119]. Research on Fe–Ti routes emphasizes the importance of the deposition sequence and thermodynamic considerations. Applying vanadium to Ti6Al4V before steel prevents σ-phase formation, while reversing this order leads to brittle regions and subsequent cracking during post-heat treatment[116,119].

A third option integrates global densification with local enhancement. HIP eliminates porosity in PBF Fe–Cu or Ti–Al bimetals[292,293]. Subsequently, low-temperature aging or stress-relief can be selectively applied to the precipitation-hardening zones, thereby preventing grain growth in the softer regions[115]. This differs from as-built SS316L/440C

laminates, in which lack-of-fusion pores and BD-parallel cracks remain if HIP or region-specific thermal steps are not incorporated[200].

Localized control of the microstructure during or after deposition can effectively precondition the material for subsequent heat treatment. In Ti–Ni systems, ultrasonic-assisted L-DED fragmented coarse Ti_2Ni into granular particles, diminished Ni segregation, and increased the flexural strength from 805 MPa to 1 047 MPa[120]. Ultrasonic assistance in SS308L/IN718 FGMs resulted in refined grains and homogenized hardness before aging. In contrast, unassisted deposits frequently exhibit interdendritic segregation, which restricts a uniform response to a global aging cycle[294].

Thermodynamic and kinetic design can ensure that each layer is positioned within a stable phase field that is compatible with the standard HT. Bobbio et al. integrated equilibrium and Scheil simulations to develop an SS316/Ni-20Cr/Cr/V/Ti6Al4V FGM characterized by printed regions transitioning from FCC to FCC/BCC to BCC[117]. This FGM successfully withstood standard stress-relief processes without the formation of σ or intermetallic compounds (IMCs), in contrast to Ti–Fe paths constructed without guidance[115,116]. DED systems, with their larger melt pools and smoother composition gradients, can tolerate conventional solution-plus-aging schedules (e.g., 980 °C/1 h solution + 720 °C/8 h aging for IN718/steel joints)[119]. In contrast, PBF components typically require HIP in conjunction with localized or mild cycles because of their more pronounced interfaces and elevated residual stresses. For each alloy pair, it is essential to optimize densification, phase stability, and property objectives through one or more of the outlined strategies[200,295].

5. MM-AM applications

In this section, an overview of the promising applications facilitated by the emerging field of metal MM-AM is provided. The integration of metals and alloys with AM processes enables designers to customize and enhance the properties of the final product to meet specific requirements that were previously unattainable. The utilization of MM-AM typically relies on disparities in the thermal conductivity, thermal expansion coefficient, and corrosion resistance of materials[5,296]. MM-AM has seen significant advancements across various industries, with notable case studies highlighting its benefits. From the perspective of companies engaged in MM-AM, general electric (GE) aviation exemplifies the application of this technology by producing intricate turbine engine components. This approach effectively integrates diverse materials to improve performance while simultaneously reducing weight. Similarly, the National Aeronautics and Space Administration (NASA) has explored multi-material manufacturing for rocket components, optimizing strength and cost efficiency by combining lightweight materials and advanced alloys. Within the automotive industry, Volkswagen utilizes multi-material additive manufacturing techniques for rapid prototyping purposes, facilitating the evaluation of diverse design configurations and material options prior to mass production. Similarly, Lockheed Martin and Siemens applied this technology in the fabrication of essential defense and industrial components, respectively, with an emphasis on enhancing performance and minimizing material waste. Overall, the widespread adoption of MM-AM holds substantial promise in various industries, such as aerospace, automotive, biomedical, and electronics, where weight and cost considerations are of prime concern[8,297]. It is important to note that at the conclusion of each application section, we conduct an overview of the technology readiness level (TRL) assessments alongside a cost−benefit analysis (CBA) for one case study.

5.1. Aerospace and automotive sector

Metallic MM products created through AM are utilized in critical components in the aerospace sector, operating in highly challenging conditions. The aerospace sector exhibits a strong interest in these capabilities, as weight significantly influences fuel efficiency and, consequently, the operational costs associated with the asset. Engineering designs that prioritize the optimization of both weight and performance present potential opportunities for cost reduction. Some potential aerospace applications are shown in Figures 12(a)–(h). For example, the MM-AM process facilitates the fabrication of complicated fuel nozzles that incorporate cooling channels within their structure[298]. This is achieved by strategically combining materials with superior thermal conductivity for effective heat dissipation and corrosion resistance, ensuring compatibility with the delivered fuel. Consequently, these nozzles are able to dispense fuel while efficiently mitigating the potential for overheating issues. It is notable to highlight that propulsion plays a significant role in spacecraft development. Approximately 70% of the total cost and a substantial portion of the manufacturing timeline of a spacecraft are associated with its propulsion system. Therefore, optimizing the design and production of this system presents an opportunity to achieve substantial efficiencies in both time and cost during spacecraft manufacturing[299,300].

The National Aeronautics and Space Administration (NASA) has integrated L-PBF and L-DED techniques to fabricate the copper alloy liner and nickel alloy jacket components of the liquid rocket combustor[300]. Examples of component configurations using copper alloy-superalloy bimetallic AM interfaces are shown in Figure 12(a). The combustor exhibits higher thermal conductivity and operating temperature because of the combination of the two materials. This suggests that using multiple materials through AM techniques enables the creation of uninterrupted cooling channels connecting the chamber and the nozzle, thereby diminishing the weight of components through the strategic arrangement of materials[298]. Another example of combustion parts of multi-materials made of nickel-copper developed by Fraunhofer IGCV is shown in Figure 12(b)[301].

Ti alloys have a low Young's modulus, wear resistance, and thermal properties, and only work stably below 500 °C, which limits their broad applications. To overcome these limitations,

Figure 12. Examples of multi-material with potential applications in the aerospace and automotive sectors. (a) Examples of component configurations using Copper-Superalloy bimetallic AM. From[298]. Reprinted with permission from AAAS. (b) Nickel-Copper combustion chambers (Fraunhofer IGCV). Reproduced with permission from[301]. © Fraunhofer IGCV, Prof. Christian Seidel. (c) A one-piece rocket made of low-density Ti6Al4V and high-melting temperature refractory metal (Nb). Reproduced from[302], with permission from Springer Nature. (d) Ti48Al2Cr2Nb and Ti6Al4V bimetal component. Reprinted from[303], Copyright (2021), with permission from Elsevier. (e) L-PBF-manufactured AISI 316L-Cu10Sn for aircraft turbine disk. Reproduced from[284]. © 2020 The Author(s). Published by IOP Publishing Ltd on behalf of the IMMT. CC BY 3.0. (f) A286 SS to Invar36 gradient alloys for carbon fiber composite inserts. Reproduced with permission from[304]. CC BY-NC-ND 4.0. (g) Aerospace heat exchanger AM using stainless steel SS316 and Inconel 718. Reprinted from[219], Copyright (2021), with permission from Elsevier. (h) The fabrication of SS304L to IN625 automotive valve stems. Reproduced from[302], with permission from Springer Nature. (i) An injection nozzle for large bore engines, investigated in cooperation with MAN Energy Solutions SE (Prof. Christian Seidel (Munich University) Fraunhofer IGCV). Reproduced with permission from[301]. © Fraunhofer IGCV, Prof. Christian Seidel. (j) Multi-material heat sink additively manufactured in a copper alloy (inner core) and stainless steel (outer shell) investigated in Aerosint, worked with the Fraunhofer[305]. Reproduced with permission from[306]. © Schaeffler Aerosint SA.

numerous researchers are investigating the integration of Ti alloys with other materials possessing favorable properties at a lower cost[296,307]. Notably, there have been recent instances of utilizing AM technology to fabricate Ti-based MMs. To showcase the possible applications of compositionally graded metal alloys, a series of prototype components are manufactured via alloy combinations. A prototype gradient rocket nozzle, depicted in Figure 12(c), was created employing a gradient ranging from Ti6Al4V to the pure refractory metal niobium (Nb). This nozzle was specifically designed for areas subjected to significant heat loads, necessitating materials with high melting points[302].

Turbine engines with integrated sub-elements of different materials and structures represent a notable application of MM-AM, aimed at achieving distinctive and enhanced properties in the components[308]. Engine parts, such as turbine blades, can be manufactured via a combination of different materials, including high-strength alloys for the core (Ti6Al4V) and heat-resistant alloys for the leading edges (Ti48Al2Cr2Nb) (Figure 12(d))[303]. This method enhances the efficiency and durability of turbine blades, enabling them to endure elevated temperatures and pressures while preserving their structural soundness. L-PBF has also been utilized to explore the feasibility of producing turbine disks by using ultrasonic powder dispensers to produce MMs components with a spatial ring and blades made of Cu10Sn and AISI316L, respectively (Figure 12(e))[284,309].

Another study described the utilization of L-DED in the production of aerospace shaft sleeve components, as shown in Figure 12(f), where the radial composition transitions gradually from A286 stainless steel to Invar36. The radial shift was specifically engineered to leverage the variation in the coefficient of thermal expansion (CTE). This design results in a significantly reduced thermal expansion compared with that of pure stainless steel. An example highlighting the advantage of radially graded alloys over wrought alloys in terms of mechanical properties is the application of a carbon fiber inserted in low-temperature spacecraft panels. As depicted in Figure 12(f), the radial gradient was intentionally formulated with an inner core composed of A286 stainless steel, a material commonly utilized in spacecraft bolts. The exterior of the rod, transitioning to Invar 36, possesses a comparably low CTE to that of the carbon fiber panel. It can be deduced that using MMs can effectively mitigate abrupt CTE discrepancies between two or more dissimilar materials when they are gradually bonded together. This approach aims to prevent potentially catastrophic failures resulting from increased susceptibility to crack formation at interfaces with abrupt changes in material composition[304].

According to reports, introducing nickel into iron-based materials is advantageous because of the superior properties exhibited by nickel-containing alloys such as IN625 and IN718, including exceptional strength, corrosion resistance, and thermal shock resistance at elevated temperatures. This combination shows promise for advancing high-performance components in engines, such as valve stems, drive shafts, piston parts, and connecting elements. In an effort to merge the high-temperature capabilities of IN718 with the ductility and cost-effectiveness of AISI316L, multi-material heat exchangers have been produced by researchers at Wits and Amsterdam (Figure 12(g))[310].

MMs produced by AM have potential applications in the automotive sector, particularly for components such as automotive valve stems. An illustration in Figure 12(h) depicts a possible gradient from SS304L to IN625 in a valve stem produced through AM. In high-performance vehicles, valves are typically made from the high-temperature nickel alloy IN625 and are subsequently friction-welded to a stainless steel stem. However, these friction welds are susceptible to failure in such applications, primarily because of the abrupt transition present in the weld joint[302].

Wear- and heat-resistant steel can be integrated with a copper alloy that exhibits high thermal conductivity for applications involving large-bore engines. Figure 12(i) illustrates a case study of an injection nozzle collaboratively examined by Fraunhofer IGCV and MAN Energy Solutions SE[301]. The multi-material design incorporates a copper core within the region subjected to significant stress, resulting in improved temperature regulation of the injection nozzle and, consequently, enhanced engine performance.

As previously stated, to enhance the integration of various industries within the context of MM-AM, we investigated a framework that combines TRL evaluations and CBA based on their reports. TRL is a standardized metric employed to evaluate the maturity of a technology, ranging from initial conceptualization to a fully validated and operational system. This scale was originally established by NASA in the 1970s to facilitate the assessment of space-related technologies[311]. Subsequently, it has been embraced by various organizations, including the U.S. Department of Defense, the European Space Agency (ESA), and the European Commission, for the purposes of research and innovation initiatives. In the context of MM-AM, TRLs serve as a valuable framework for monitoring advancements, ranging from initial material compatibility assessments (TRL 3–4) to pilot production stages (TRL 6–7) and ultimately to comprehensive industrial implementation (TRL 9). This progression is frequently accompanied by cost–benefit analyses to ascertain both the technical feasibility and economic viability of the processes involved[311].

In the aerospace sector, MM-AM projects often involve collaborations between agencies such as NASA, the European Original Equipment Manufacturer (OEMs), and research institutes such as Fraunhofer, focusing on integrating high-conductivity copper alloys (e.g., CuCrZr) with high-temperature superalloys (e.g., Inconel 718) for rocket engine liners and cooling structures. TRL development typically starts at 3–4 with coupon-level metallurgy and bond integrity studies, advances to TRL 5–6 with subscale hot-fire testing in relevant environments, and reaches TRL 7–8 with qualification in flight-like conditions. Cost–benefit analyses show that while initial builds can cost 20%–25% more than single-alloy parts, lifecycle savings from reduced welds, simplified cooling systems, and improved thermal efficiency can yield return on investment (ROI) in under five years, alongside non-monetary gains such as weight reduction and mission performance improvements.

An industrial example that is released by Aerosint (now part of Desktop Metal) partnered with Fraunhofer IAPT, is a multimaterial heat sink that combined copper for high thermal conductivity with tool steel for structural strength (Figure 12(j))[305]. These advanced heat sinks offer effective solutions for challenging applications within the automotive and aerospace sectors, where efficient heat dissipation and space optimization are essential. For instance, they can enhance the performance and longevity of electronic components. Moreover, manufacturing this multi-functional component through a single process considerably shortens lead times and decreases production expenses. The project progressed through the TRL stages, starting with lab-scale proof-of-concept (TRL 3–4) to demonstrate metallurgical bonding, moving to component validation (TRL 5) with small prototypes, and then to pilot-scale production (TRL 6–7), where full-size heat sinks were tested in aerospace cooling systems. By TRL 8, the design was optimized for manufacturability and certification, and at TRL 9, the heat sinks were deployed in operational aerospace electronics, proving their long-term stability and performance.

In parallel, a cost–benefit analysis (CBA) was conducted at each stage, following an aerospace-style approach. While initial production costs were approximately 20% higher than those of conventional copper heat sinks due to dual-material handling, lifecycle savings came from partial consolidation, reduced assembly steps, and extended service life. The performance gains included a 30% improvement in heat transfer, enabling lighter, more compact cooling systems—a major advantage in aerospace, where weight reduction translates to fuel savings.

5.2. Biomedical sector

Metals and alloys have been essential materials for medical devices for more than a hundred years. Currently, around 70%–80% of bio-implants consist of metals and alloys because of their remarkable durability and long-lasting properties[312]. Nevertheless, bio-implants must exhibit supplementary attributes to guarantee optimal performance, including lightweight construction, non-toxicity, corrosion resistance, and biocompatibility. The integration of ductile alloys with wear-resistant material systems facilitates more precise customization of the final properties of the implants[82].

The utilization of MM-AM is significantly transforming the biomedical sector. The AM industry dedicated to biomedical purposes is anticipated to achieve a market value of $3.7 billion by 2026[313]. This growth is attributed to the substantial market opportunities presented by MM-AM technology. Various biomedical applications have been developed by utilizing MM-AM, facilitating prosthetic fabrication with multi-material compositions and customized designs that incorporate specific material attributes. Moreover, as already stated in Section 2, MM-AM allows for the integration of biocompatible metals, polymers, and ceramics to fabricate structures that closely resemble the properties of natural tissues. Manufacturers can develop prosthetics that offer enhanced comfort, functionality, and aesthetic appeal by combining materials with diverse flexibility, strength, and weight properties. From a long-term perspective, it may be feasible to produce metal implants that possess customized biocompatibility, such as those utilizing resorbable materials, or that incorporate integrated sensors designed for the in vivo detection of early-stage inflammations[314].

An illustration of this concept is the application of gradient structures in bio-implants, which can improve their durability and decrease the risk of implant failure. The biomechanical incompatibility arising from a disparity in the Young's modulus between the bio-implants and adjacent tissues may lead to stress shielding and issues such as implant loosening and necrosis of bone cells. Figure 13(a) shows a printed NiTi/Ti6Al4V multi-material hip implant composed of two distinct materials: a Ti6Al4V inner region known for its superior mechanical properties, such as strength and stiffness, and a NiTi outer region designed to undergo controlled volume expansion through shape memory activation. This unique design aims to enhance bone-implant contact and stimulate bone ingrowth for improved implant stability and integration within the body[205]. An additional illustration involves the production of Ti-based MMs with a stiffness gradient, as depicted in Figure 13(b). In this context, a bi-directionally graded metamaterial composed of titanium-niobium-zirconium with five distinct regions was created. The central region consisted of commercially pure titanium with a higher elastic modulus of 110 GPa to enhance mechanical toughness, whereas regions 1 and 5 at the periphery exhibited a lower elastic modulus of 75 GPa to align with the mechanical characteristics of bones. These metamaterials with a stiffness gradient exhibit suitable performance for orthopedic implant applications[315]. Currently, new elements such as Mo, as non-toxic elements, can stabilize the β-phase of Ti, and reducing the elastic modulus of titanium has been used to design new alloys in the biomedical sector. Schneider-Maunoury et al.[174] successfully prepared Ti6Al4V/Mo with good metallurgical bonding (Figure 13(c)). The Ti6Al4V/Mo multi-material has great potential for biomedical applications, such as trauma surgery or orthopedic implants. Moreover, the gradient porosity configuration of Ti6Al4V hip implants has been found to improve the balance between strength and ductility while also promoting enhanced fluid permeability at the interface with tissue, thereby facilitating cell proliferation (Figure 13(d)). Wu et al.[316] used EBM to prepare a variety of porous Ti6Al4V (Figure 13(e)). The porosity gradient with a thickness of 4–8 mm led to the best compressive strength. This has the potential to address the challenge of inadequate integration between bones and implant materials[317].

From the biomedical sector, an industrial collaboration point of view, MM-AM is driven by partnerships between medical device OEMs, universities, and regulatory bodies to produce implants that combine metals such as Ti-6Al-4V for structural strength with tantalum or NiTi for enhanced osseointegration and corrosion resistance[185]. TRL progression often begins at 3–4 with mechanical and biocompatibility testing, moves to TRL 5–6 with cadaveric or animal trials, and reaches TRL 7–8 with limited clinical use

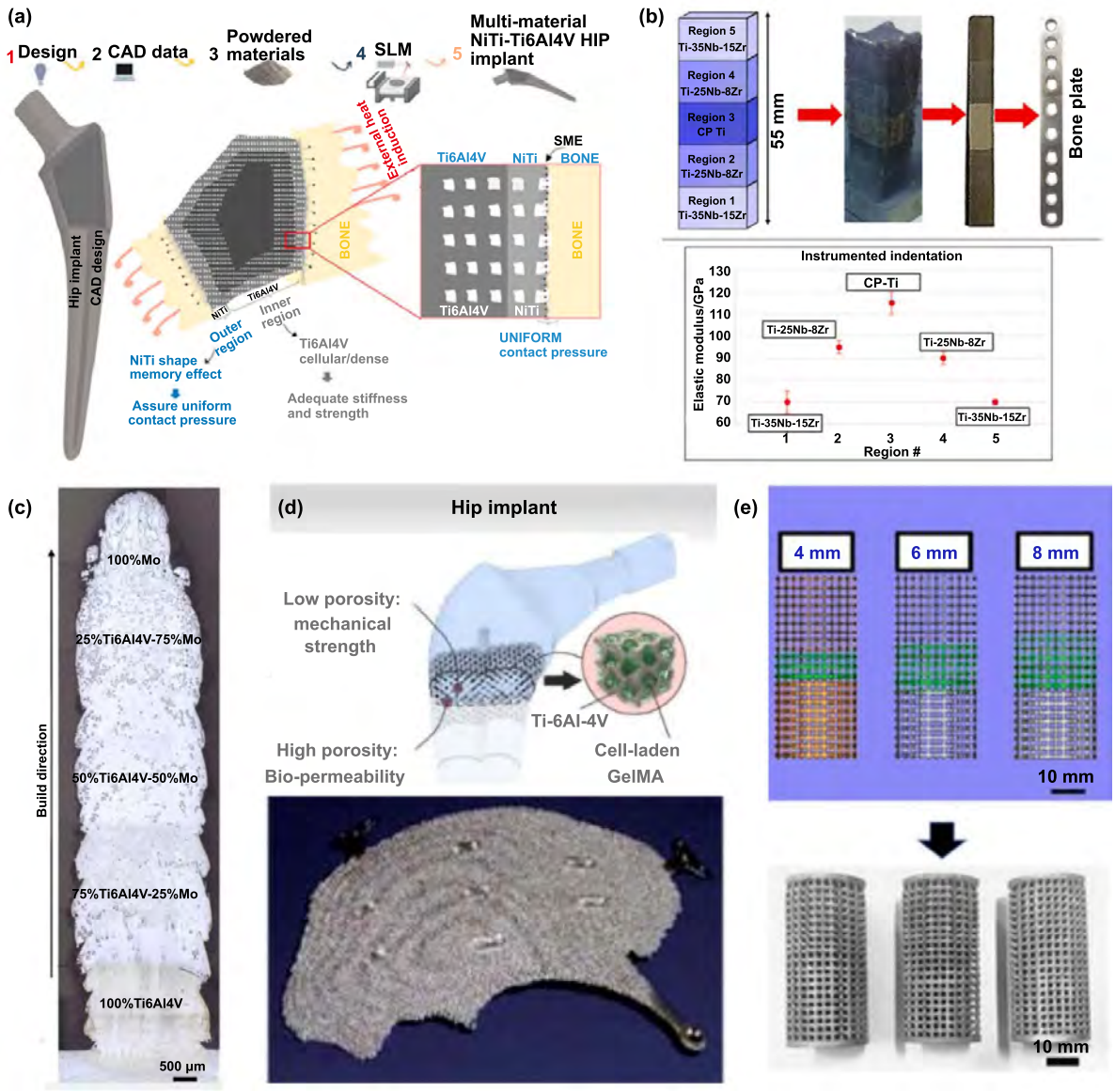

Figure 13. Examples of multi-material with potential applications in the biomedical sector. (a) Design concept of a NiTi/Ti6Al4V multi-material hip implant. Reprinted from[205], Copyright (2020), with permission from Elsevier. (b) Ti-based MM with a stiffness gradient. Reprinted from[315], Copyright (2017), with permission from Elsevier. (c) Cross-sectional structure of a Ti6Al4V/Mo. Reprinted from[174], Copyright (2017), with permission from Elsevier. (d) Porous titanium craniofacial part with a graded porosity and density. Reproduced from[317]. CC BY 4.0. (e) Schematic diagram and actual printing samples of a variety of porous Ti6Al4V. Reprinted from[316], Copyright (2018), with permission from Elsevier.

under regulatory oversight. Cost–benefit analyses reveal that although production costs can be 30% higher than those of conventional implants, improved patient outcomes, reduced revision surgeries, and faster recovery times deliver strong long-term value, with non-monetary benefits, including competitive differentiation and enhanced patient quality of life.

5.3. *Electronic sector*

The utilization of MM-AM is essential in the production of electronic components, as it facilitates the incorporation of various alloys within intricate structures. This capability enables the customization of magnetic field shapes, leading to increased efficiency and reduced costs in the production of electric motors. Rotary electrical machines, encompassing motors and generators, have emerged as principal prime movers in contemporary society, whereas static electrical machines, such as transformers, have become integral components of the future global energy infrastructure[318]. Confronted with emerging design and performance demands, the community promptly embraced MM-AM. Figure 14(a) displays a prototype of an AMed electric motor stator and a conceptual design of a spherical reluctance electric motor developed utilizing a computational engineering model authored by LEAP 71. The motor components were fabricated from steel and copper materials via the experimental MM-AM

manufacturing process established by the Fraunhofer IGCV and produced via a Nikon SLM solution printer[319].

Efficient thermal management in electronic devices relies on the utilization of heat sinks and cooling systems, which can be enhanced through the application of MM-AM to achieve optimized designs. By integrating materials with superior thermal conductivity for effective heat dissipation and incorporating lightweight alloys to decrease weight, manufacturers can develop heat sinks that efficiently dissipate heat while simultaneously reducing the overall weight and dimensions of electronic systems[309]. The L-PBF fabrication process of the MM heat exchanger offers a cost-efficient alternative to conventional welding techniques. Figure 14(b) shows a tubular heat exchanger composed of CuCrZr/AISI316L materials featuring a complex curved configuration fabricated by Aerosint SA[305]. Within this heat exchanger, the copper tube serves as one of the conduits enclosed by the AISI 316L channel. The design rationale revolves around utilizing copper for the inner tubes to optimize the thermal conductivity while employing stainless steel for the outer shell to ensure structural integrity and chemical inertness.

AM has also exhibited the ability to integrate electronic components, such as sensors, into printed objects within the specified dimensions. By embedding sensors into the printed part during a fabrication pause, AM presents the potential for the complete encapsulation of sensors for operation in challenging environments or within the human body. For example, the non-intrusive integration of sensors or strain gauges into the bodies of components, such as engine blocks (Figure 14(c)), via AM technology could create a dynamic system that continuously offers feedback on structural integrity, thereby enhancing the life span and versatility of components[3,4]. Additionally, by embedding inductors into implants during laser beam melting fabrication, researchers have continuously monitored interactions between the implant and surrounding tissue to assess infection risks and stress levels for real-time performance evaluation (Figure 14(d))[321].

Additionally, using MMs through AM technology presents a novel opportunity to incorporate security elements in hard-to-reach areas of AM components, such as the inner surface of a hollow turbine blade, during the manufacturing process. This technology could also be leveraged to integrate anti-counterfeiting measures into traditional manufacturing processes and high-value metal components. Furthermore, it has the potential to be combined with blockchain technology to verify the authenticity of produced items. These security features could also be utilized to document the complete life cycle of a part, encompassing its manufacturing, inspection, maintenance, and recycling stages. Variations in material density result in the detection of embedded security codes through X-ray and infrared (IR) imaging, as illustrated in Figure 14(e)[322].

From an electrical and electronics industry collaboration point of view, MM-AM collaborations link machine OEMs (e.g., prima additive), research institutes, and aerospace/automotive suppliers to develop copper–aluminum hybrid busbars, motor stators, and thermal management components. TRL advancement typically starts at 3–4 with metallurgical bonding and conductivity tests, progresses to TRL 5–6 with functional prototypes undergoing thermal cycling and electrical resistance evaluation, and reaches TRL 7 with pilot-line production in relevant environments. Cost–benefit analyses show that while raw material and process costs are higher than those for conventionally machined parts, weight reductions of up to 35%, improved conductivity in critical zones, and smaller cooling system requirements can produce ROI in 2–3 years, with added strategic benefits in high-performance aerospace and electric vehicle markets. An illustrative industrial case within the FORNEXTGEN program involves the Fraunhofer IGCV's development of electric motor stators and rotors. These components incorporate copper windings and steel laminations fabricated concurrently through a single additive manufacturing process, thereby eliminating the need for separate winding and assembly stages[266]. The work began at TRL 3–4 with metallurgical bonding and conductivity tests, progressed to TRL 5–6 with functional prototypes, and reached TRL 7 with pilot-line production for e-e-mobility demonstrators. Although AM process costs were higher than conventional manufacturing, the CBA showed that weight reduction, improved electrical efficiency, and shorter production cycles could deliver ROI in as little as 2–3 years for high-performance electric drivetrains.

5.4. Other application functionalities

Table 4 summarizes the characteristics and applications of different MM-AM materials. In addition to the mentioned applications, there is ongoing progress in creating MMs with gradient structures or modified chemical compositions through AM techniques. Further research and advancements are necessary to fully exploit their capabilities and facilitate wider industrial integration. For example, these materials can enhance the radiation tolerance of nuclear reactor components and fortify armor against diverse sources of damage. In injection molding applications, the integration of abrasion-resistant tool steel with a copper alloy exhibiting high thermal conductivity can substantially decrease cycle times during the production of plastic components characterized by high aspect ratios. Furthermore, the utilization of aluminum and copper alloy combinations presents potential cost reduction opportunities in the manufacturing of electric motors. Furthermore, MMs are being explored to create damping mechanisms that can absorb mechanical energy under stress or vibration conditions.

6. Perspective

A general overview of the state of the art in MM-AM indicates that direct metal AM technologies have made unprecedented growth in the research and development of MM products in various sectors. Nevertheless, some issues and challenges in different stages, from design to market, have held back MM-AM from its real potential, which should be considered high-priority future work directions as follows:

- On the top, the lack of a reliable MM design framework for each AM process has led to arbitrary methodologies for

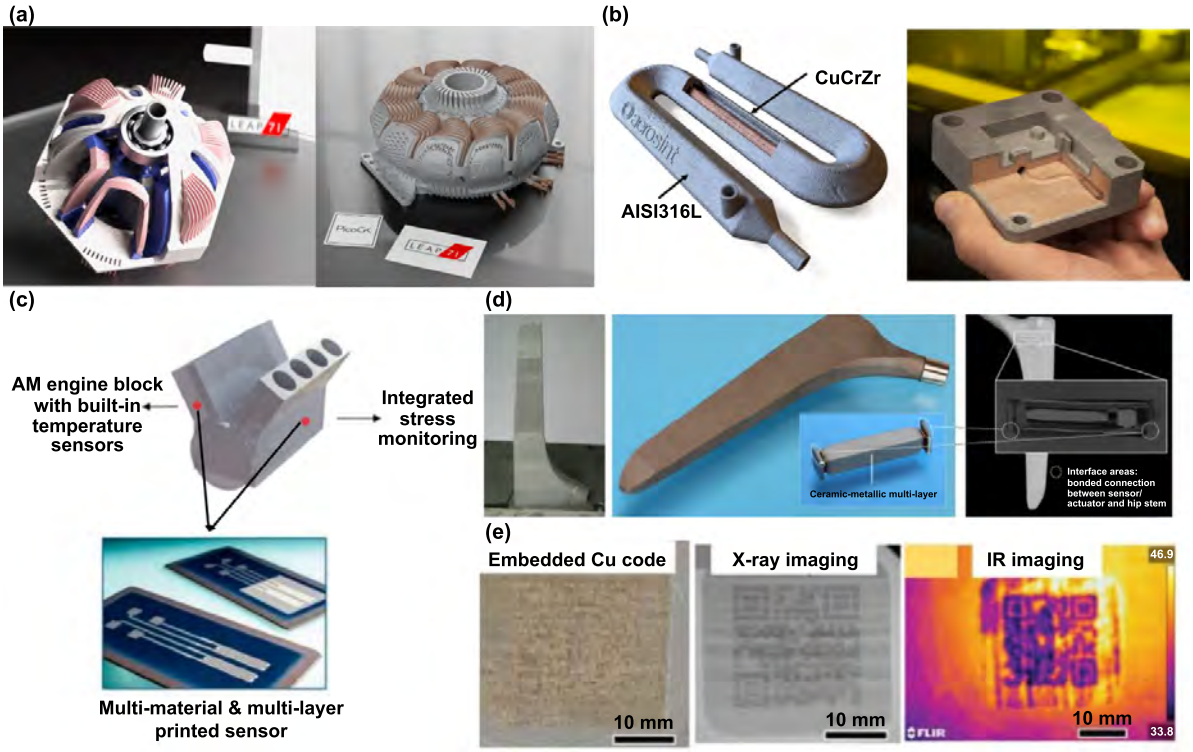

Figure 14. Examples of multi-material with potential applications in the electronics sector. (a) Electric motor stator and spherical reluctance electric motor (LEAP 71/Fraunhofer IGCV). Reproduced with permission from[319]. ©LEAP 71/Fraunhofer IGCV. (b) CuCrZr/AISI316L multi-material heat exchanger (courtesy of Aerosint.com)[305]. Reproduced with permission from[306]. © Schaeffler Aerosint SA. (c) Temperature sensor structures on a stainless-steel substrate. Reprinted from[320], with the permission of AIP Publishing. (d) Smart femoral hip stem with an embedded sensor. Reproduced from[321], with permission from Springer Nature. (e) The copper QR code embedded in stainless steel components and its X-ray image and IR image. Reprinted from[322], Copyright (2018), with permission from Elsevier.

developing efficient MMs in a costly and time-consuming manner. In addition to service requirements, to address this, we emphasize metallurgical compatibility between terminal materials as the first step and propose an integrated framework that combines thermodynamic and kinetic modeling (e.g., CALPHAD) with machine learning methods to predict transition-zone phases and process windows, standardized material–compatibility testing (minimal test matrix of thermal cycles, interdiffusion couples, microstructure mapping, and mechanical tests), common interface-characterization protocols (microscopy, EBSD, TEM, compositional line-scans), and process–structure–property maps for each AM route. Moreover, the steps can be followed by prioritized post-processing strategies for the AMed metallic multi-materials, as well as shared open databases and multiscale modeling workflows, to accelerate the future design and production of metallic multi-materials.

- Macro- to micro-scale simulations (e.g., finite volume/element to cellular automata and phase-field methods) of the process not only could result in a better understanding of the interaction between the process and materials and complex phenomena (such as melt pool dynamics, thermal stresses, defects formation, solidification structure, and grain evolution) but also, as practical tools besides real-time monitoring systems and experiments, could generate comprehensive datasets suitable for machine learning algorithms to achieve optimal processing parameters for every material composition. Additionally, improving CAD software packages specialized for MMs in which users are able to define materials distribution and properties, not just geometries, could offer more intelligent and integrated design and manufacturing.
- The PBF adaptive mechanisms to handle multiple materials have been associated mainly with the laser-based process (L-PBF) and the simplest MM design, i.e., bimetal. It is highly encouraged to establish a cost-effective solution with minimal cross-contamination of powders, as well as higher production efficiency in PBF processes, to reliably and reproducibly realize more complex MM designs, especially in EB-PBF, thereby releasing its unique capabilities of MM-AM. Overcoming this technological challenge paves the way toward the commercialization of PBF machines dedicated to MM processing. Although DED processes are undoubtedly more flexible in composition manipulation during fabrication, they require further improvements in surface quality and dimensional accuracy of the MM parts, utilizing precise systems for monitoring and controlling the melt pool characteristics.
- Very limited information is available on post-processing surface/bulk treatments of additively manufactured MM parts, which are usually needed to achieve the expected performance. Non-homogeneous structures result in different

Table 4. A summary of the properties and applications of MMs fabricated by AM.

Materials	Applications	Key properties	Industry	Processing technologies	References
Copper-stainless steel	Automatic cooling control instrument/turbine disk/bimetal porous energy-absorbing structure/anti-counterfeiting	Enhance thermal conductivity/improve structural strength/impact on distinct optical, thermal signatures	Aerospace/electrics/ mold industry	L-DED, L-PBF, WA-DED	[309,323]
Copper-aluminum	Solar energy collectors or lightweight electric motors and actuators/heat exchangers/aerospace thermal structures.	Light weight/cost savings/boosts heat or electrical transfer	Electrics/Automotive	L-DED, L-PBF, WA-DED	[324]
Invar-stainless steel	Radially graded MM inserts used on carbon fiber composite components	Low cost/excellent oxidation resistance	Aerospace	L-DED, L-PBF, WA-DED	[304]
Copper-nickel alloy	Liquid rocket combustor comprised of a copper alloy liner and a nickel alloy jacket	Increase thermal conductivity, diffusivity, light weight	Aerospace	L-DED, L-PBF,	[298,300]
Stainless steel-nickel alloy	Nuclear reactor components used in the nuclear power plant or the miniature nuclear/electricity energy conversion system for space exploration/automotive valve stems	Low cost/corrosion resistance at high temperatures/improved hardness and wear resistance	Nuclear/electrics /automotive	L-DED, L-PBF, EB-PBF	[215,302]
Titanium-titanium	Turbine blades/fracture fixation plate/orthopedic implants	Improve biocompatibility/enhanced abrasion resistance	Aerospace/biomedical	L-DED, L-PBF, EB-PBF	[205,303,315]
Titanium-copper	Metal extraction/energy production/the repair of metallic components	Improved corrosion resistance/cost savings	Aerospace	L-DED, L-PBF, EB-PBF	[2,308]

responses to a certain post-treatment operation over compositional regions, making them more complicated than single-material cases. Therefore, post-treatment variables should be accurately adjusted considering the entire MM structure to avoid undesired changes in every compositional region unless the highly contrasting nature of the parent materials dictates stepwise post-treatments with respect to the characteristics of each composition.

- While the technical issues of MM-AM (materials, compatibility, and geometry) have received significant attention, the economic implications are equally vital. In MM-PBF, the cost increases because of specialized powder handling, multiple feeders, contamination mitigation, and reduced powder reutilization rates (Khanna et al. reported that PBF is approximately five times more costly than DED for similar components[268]). In L-DED-based MM, models show that material and machine costs together may account for ∼90% of the total cost, with DED often achieving substantially lower unit costs when the geometry and accuracy requirements are relaxed[325]. Activity-based costing in PBF indicated that post-processing, component geometry, and the build rate substantially affect overall costs, frequently adding 20%–40% overhead to the base build expenses[325]. Accordingly, future MM-AM economic strategies must incorporate hybrid process approaches, powder recycling and segregation management, as well as cost models that link parameters (rate, utilization, post-machining) to the final unit cost.
- The majority of the literature has focused on the overall basic properties of AM-produced MM parts. In contrast, multi-objective performance analysis concerning real-life applications should be performed via localized and in situ characterization techniques to provide more details on the behaviour of every compositional region under simulated working conditions, figure out failure mechanisms and weaknesses of present MMs, and develop more efficient ones. Meanwhile, further development of MM-AM requires standardization of testing methods to ensure the quality of the MM product through repeatable and comparable results.

7. Summary

Multi-material structures, inspired by natural patterns, have become integral to modern life because of their multi-functionality and superior performance across various applications. Traditional manufacturing methods introduced multi-materials into engineering, but additive manufacturing has significantly accelerated their development owing to its layer-wise mechanism, allowing for the integration of flexible material designs and complex geometries. Consequently, multi-material additive manufacturing enables designers to customize and enhance the properties of final products to meet specific requirements that were previously unattainable. This review highlights recent progress in multi-material additive manufacturing, focusing on processing multi-material metallic components, case studies, and practical applications in sectors such as aerospace, automotive, biomedical, and electronics.

Over the past decade, multi-material additive manufacturing—particularly direct metal AM methods such as DED and PBF—has advanced substantially, broadening material and process choices to meet critical engineering needs. These processes enable a range of metal compositions, including aluminum, steel, titanium, superalloys, and metal–nonmetal composites. DED is prized for efficient fabrication of large components and flexible material combinations, whereas PBF, although less adaptable to mid-process composition changes, provides higher resolution, tighter dimensional tolerances, superior surface finish, reduced waste, and better part performance. Researchers continue to address single-material limitations to produce multi-material metal AM parts with targeted functional properties.

The Fe–Ni family is the most studied for its balance of properties and cost, while Fe–Cu systems combine Fe strength with Cu thermal and electrical conductivity; Ti alloys serve as terminal materials for biomedical and aerospace MM–AM, and composites, ceramics, and intermetallics are also reported, with many studies examining the properties and formation of detrimental phases and defects across composition gradients. Multi-material AM enables scaffolds, energy harvesters, soft sensors, lightweight automotive parts, and 3D-printed dentures, offering advantages for aerospace, automotive, biomedical, and electronics. EB-PBF, which operates hot and in vacuum, already processes many metals and is well positioned to expand multi-material capability, but progress requires integrated, process-specific MM design frameworks, improved CAD and simulation tools, adaptive PBF control, robust post-processing, and standardized qualification to avoid harmful phases and cracking.

Improved simulation tools and CAD software specialized for multi-materials can offer more intelligent and integrated design and manufacturing solutions. In parallel, data-driven methods, particularly machine learning (ML) models, can significantly enhance MM-AM development and scalability by optimizing process parameters, enabling real-time monitoring, facilitating material design, and promoting discovery, among other applications. Additionally, cost-effective solutions for PBF processes, effective post-processing treatments, and standardized testing methods are essential for the commercialization and widespread adoption of MM-AM.

Data availability statement

No data was used for the research described in the article.

Conflict of interest

The authors declare that they have no known competing financial interests or personal relationships that could have appeared to influence the work reported in this paper.

ORCID iD

Abdollah Saboori 0000-0001-7135-1316

References

[1] Chen A N et al. 2024. Multimaterial 3D and 4D bioprinting of heterogenous constructs for tissue engineering. *Adv. Mater.* **36**, 2307686.
[2] Terrazas C A, Gaytan S M, Rodriguez E, Espalin D, Murr L E, Medina F and Wicker R B. 2014. Multi-material metallic structure fabrication using electron beam melting. *Int. J. Adv. Manuf. Technol.* **71**, 33–45.
[3] Gu D D, Shi X Y, Poprawe R, Bourell D L, Setchi R and Zhu J H. 2021. Material-structure-performance integrated laser-metal additive manufacturing. *Science* **372**, eabg1487.
[4] Bandyopadhyay A and Heer B. 2018. Additive manufacturing of multi-material structures. *Mater. Sci. Eng. R* **129**, 1–16.
[5] Wei C and Li L. 2021. Recent progress and scientific challenges in multi-material additive manufacturing via laser-based powder bed fusion. *Virtual Phys. Prototyp.* **16**, 347–371.
[6] Nguyen N, Park J G, Zhang S L and Liang R. 2018. Recent advances on 3D printing technique for thermal-related applications. *Adv. Eng. Mater.* **20**, 1700876.
[7] Sakundarini N, Taha Z, Abdul-Rashid S H and Ghazila R A R. 2013. Optimal multi-material selection for lightweight design of automotive body assembly incorporating recyclability. *Mater. Des.* **50**, 846–857.
[8] Wang D et al. 2022. Recent progress on additive manufacturing of multi-material structures with laser powder bed fusion. *Virtual Phys. Prototyp.* **17**, 329–365.
[9] Hasanov S, Gupta A, Nasirov A and Fidan I. 2020. Mechanical characterization of functionally graded materials produced by the fused filament fabrication process. *J. Manuf. Process.* **58**, 923–935.
[10] Chastel Y and Passemard L. 2014. Joining technologies for future automobile multi-material modules. *Proc. Eng.* **81**, 2104–2110.
[11] Ghanavati R and Naffakh-Moosavy H. 2021. Additive manufacturing of functionally graded metallic materials: a review of experimental and numerical studies. *J. Mater. Res. Technol.* **13**, 1628–1664.
[12] Sames W J, List F A, Pannala S, Dehoff R R and Babu S S. 2016. The metallurgy and processing science of metal additive manufacturing. *Int. Mater. Rev.* **61**, 315–360.
[13] Mosallanejad M H, Ghanavati R, Behjat A, Taghian M, Saboori A and Iuliano L. 2024. Untapped opportunities in additive manufacturing with metals: from new and graded materials to post-processing. *Metals* **14**, 425.

[14] Dadkhah M, Tulliani J M, Saboori A and Iuliano L. 2023. Additive manufacturing of ceramics: advances, challenges, and outlook. *J. Eur. Ceram. Soc.* **43**, 6635–6664.
[15] Wang P, Deng L, Prashanth K G, Pauly S, Eckert J and Scudino S. 2018. Microstructure and mechanical properties of Al-Cu alloys fabricated by selective laser melting of powder mixtures. *J. Alloys Compd.* **735**, 2263–2266.
[16] Lin T C, Cao C Z, Sokoluk M, Jiang L, Wang X, Schoenung J M, Lavernia E J and Li X C. 2019. Aluminum with dispersed nanoparticles by laser additive manufacturing. *Nat. Commun.* **10**, 4124.
[17] Martin J H, Yahata B D, Hundley J M, Mayer J A, Schaedler T A and Pollock T M. 2017. 3D printing of high-strength aluminium alloys. *Nature* **549**, 365–369.
[18] Kürnsteiner P, Wilms M B, Weisheit A, Gault B, Jägle E A and Raabe D. 2020. High-strength Damascus steel by additive manufacturing. *Nature* **582**, 515–519.
[19] Errico V, Posa P, Liang L, Maurizi M, Wan D, Angelastro A, Gao C, Campanelli S L and Berto F. 2023. Layer-level AISI 316L-18Ni (300) Maraging multi-material fabrication via Laser-Powder Bed Fusion. *Mater. Sci. Eng. A* **886**, 145731.
[20] Wang J, Jeong S G, Kim E S, Kim H S and Lee B J. 2023. Material-agnostic machine learning approach enables high relative density in powder bed fusion products. *Nat. Commun.* **14**, 6557.
[21] Liu Y G et al. 2021. Additive manufacturing of high strength copper alloy with heterogeneous grain structure through laser powder bed fusion. *Acta Mater.* **220**, 117311.
[22] Zhang D Y, Qiu D, Gibson M A, Zheng Y F, Fraser H L, StJohn D H and Easton M A. 2019. Additive manufacturing of ultrafine-grained high-strength titanium alloys. *Nature* **576**, 91–95.
[23] Huang S, Narayan R L, Tan J H K, Sing S L and Yeong W Y. 2021. Resolving the porosity-unmelted inclusion dilemma during *in-situ* alloying of Ti34Nb via laser powder bed fusion. *Acta Mater.* **204**, 116522.
[24] Barriobero-Vila P, Gussone J, Stark A, Schell N, Haubrich J and Requena G. 2018. Peritectic titanium alloys for 3D printing. *Nat. Commun.* **9**, 3426.
[25] Aristizabal M, Jamshidi P, Saboori A, Cox S C and Attallah M M. 2020. Laser powder bed fusion of a Zr-alloy: tensile properties and biocompatibility. *Mater. Lett.* **259**, 126897.
[26] Guaglione F, Caprio L, Previtali B and Demir A G. 2021. Single point exposure LPBF for the production of biodegradable Zn-alloy lattice structures. *Addit. Manuf.* **48**, 102426.
[27] Yang M L, Yang L Y M, Peng S P, Deng F, Li Y G, Yang Y W and Shuai C J. 2023. Laser additive manufacturing of zinc: formation quality, texture, and cell behavior. *Bio-Des. Manuf.* **6**, 103–120.
[28] Wen P, Voshage M, Jauer L, Chen Y Z, Qin Y, Poprawe R and Schleifenbaum J H. 2018. Laser additive manufacturing of Zn metal parts for biodegradable applications: processing, formation quality and mechanical properties. *Mater. Des.* **155**, 36–45.
[29] Dadkhah M, Mosallanejad M H, Iuliano L and Saboori A. 2021. A comprehensive overview on the latest progress in the additive manufacturing of metal matrix composites: potential, challenges, and feasible solutions. *Acta Metall. Sin. (Engl. Lett.)* **34**, 1173–1200.
[30] Gu D D, Meiners W, Wissenbach K and Poprawe R. 2012. Laser additive manufacturing of metallic components: materials, processes and mechanisms. *Int. Mater. Rev.* **57**, 133–164.
[31] Ghanavati R, Lannunziata E, Norouzi E, Bagherifard S, Iuliano L and Saboori A. 2023. Design and development of SS316L-IN718 functionally graded materials via laser powder bed fusion. *Mater. Lett.* **349**, 134793.
[32] Segovia-Guerrero L, Baladés N, Attard B, De Nicolás M, Scotti A, Zammit A and Sales D L. 2024. Multi-material stainless steel fabrication using plasma wire arc additive manufacturing. *J. Mater. Res. Technol.* **30**, 3996–4002.
[33] Sai M M K, Kumar S, Mandal A and Anand M. 2023. Sinterability of SS316, SiC, and TiN multi-material additive manufacturing via selective laser sintering. *Opt. Laser Technol.* **167**, 109686.
[34] Liu G et al. 2021. Additive manufacturing of structural materials. *Mater. Sci. Eng. R* **145**, 100596.
[35] Sun H W, Zou B, Wang X F, Chen W, Zhang G X, Quan T and Huang C Z. 2024. Advancements in multi-material additive manufacturing of advanced ceramics: a review of strategies, techniques and equipment. *Mater. Chem. Phys.* **319**, 129337.
[36] Schneck M, Horn M, Schmitt M, Seidel C, Schlick G and Reinhart G. 2021. Review on additive hybrid- and multi-material-manufacturing of metals by powder bed fusion: state of technology and development potential. *Prog. Addit. Manuf.* **6**, 881–894.
[37] Verma A, Kapil A, Klobčar D and Sharma A. 2023. A review on multiplicity in multi-material additive manufacturing: process, capability, scale, and structure. *Materials* **16**, 5246.
[38] Zheng X Y, Williams C, Spadaccini C M and Shea K. 2021. Perspectives on multi-material additive manufacturing. *J. Mater. Res.* **36**, 3549–3557.
[39] Katiyar N K, Goel G, Hawi S and Goel S. 2021. Nature-inspired materials: emerging trends and prospects. *NPG Asia Mater.* **13**, 56.
[40] Dao T D, Pham D D, Nguyen T A H, Tran T V H, Vu Hoang C and Pham T T. 2020. Bio-inspired broadband absorbers induced by copper nanostructures on natural leaves. *Sci. Rep.* **10**, 3243.
[41] Nazir A, Gokcekaya O, Md Masum Billah K, Ertugrul O, Jiang J C, Sun J Y and Hussain S. 2023. Multi-material additive manufacturing: a systematic review of design, properties, applications, challenges, and 3D printing of materials and cellular metamaterials. *Mater. Des.* **226**, 111661.
[42] Putra N E, Mirzaali M J, Apachitei I, Zhou J and Zadpoor A A. 2020. Multi-material additive manufacturing technologies for Ti-, Mg-, and Fe-based biomaterials for bone substitution. *Acta Biomater.* **109**, 1–20.
[43] Wang Y H et al. 2023. Nature-inspired micropatterns. *Nat. Rev. Meth. Primers* **3**, 68.
[44] Ji W M, Zhou R H, Vivegananthan P, See Wu M, Gao H J and Zhou K. 2023. Recent progress in gradient-structured metals and alloys. *Prog. Mater. Sci.* **140**, 101194.
[45] Yasuga H et al. 2021. Fluid interfacial energy drives the emergence of three-dimensional periodic structures in micropillar scaffolds. *Nat. Phys.* **17**, 794–800.
[46] Stagni A, Trevisan G, Vergani L and Libonati F. 2024. Bone osteon-like structures: a biomimetic approach towards multiscale fiber-reinforced composite structures. *Compos. Sci. Technol.* **254**, 110669.
[47] Nyabadza A, Kane J, Vázquez M, Sreenilayam S and Brabazon D. 2021. Multi-material production of 4D shape memory polymer composites. *Reference Module in Materials Science and Materials Engineering* (Elsevier). pp 879–894.
[48] Zhang Z Q, Huang Y J, Xie Q Y, Liu G J, Ma C F and Zhang G Z. 2024. Functional polymer–ceramic hybrid coatings: status, progress, and trend. *Prog. Polym. Sci.* **154**, 101840.

[49] Liu F, Wang Y R, Cao J, Chen J J, Luo T, Zhou C, Tang Y C and Xie H Q. 2024. A simple method for fabricating polymer/ceramic functionally graded material scaffold. *Ceram. Int.* **50**, 14497–14512.
[50] Wang R, Gu D D, Huang G J, Shi K Y, Yuan L H and Zhang H. 2023. Multilayered gradient titanium-matrix composites fabricated by multi-material laser powder bed fusion using metallized ceramic: forming characteristics, microstructure evolution, and multifunctional properties. *Addit. Manuf.* **62**, 103407.
[51] Blanco D, Rubio E M, Sáenz-Nuño M A and Lorente-Pedreille R M. 2022. Comparison of sustainable cooling systems used in the drilling repair of Mg-Al and Mg-Ti multi-material parts in the aeronautical industry. *Tribol. Int.* **175**, 107804.
[52] Veron F, Lanoue F, Baco-Carles V, Kiryukhina K, Vendier O and Tailhades P. 2022. Selective laser powder bed fusion for manufacturing of 3D metal-ceramic multi-materials assemblies. *Addit. Manuf.* **50**, 102550.
[53] Zhou G A, Li Z X, Wang Q H, Zhu Y X, Hua P, Yao S H and Sun Q P. 2024. A multi-material cascade elastocaloric cooling device for large temperature lift. *Nat. Energy* **9**, 862–870.
[54] Mirzaali M J et al. 2020. Mechanics of bioinspired functionally graded soft-hard composites made by multi-material 3D printing. *Compos. Struct.* **237**, 111867.
[55] Alcântara C C J, Landers F C, Kim S, De Marco C, Ahmed D, Nelson B J and Pané S. 2020. Mechanically interlocked 3D multi-material micromachines. *Nat. Commun.* **11**, 5957.
[56] Ingrole A, Aguirre T G, Fuller L and Donahue S W. 2021. Bioinspired energy absorbing material designs using additive manufacturing. *J. Mech. Behav. Biomed. Mater.* **119**, 104518.
[57] Cui Y X, Yang T, Luo H C, Li Z X and Jing X J. 2024. Jellyfish-inspired bistable piezoelectric-triboelectric hybrid generator for low-frequency vibration energy harvesting. *Int. J. Mech. Sci.* **279**, 109523.
[58] Wang M, Wang Y L, Han Y X, Dong H, Huo F and He H Y. 2024. Bio-inspired polyionic membrane for long-lasting and repeatable electricity harvesting from moisture. *Nano Energy* **123**, 109376.
[59] Emon O F, Alkadi F, Philip D G, Kim D H, Lee K C and Choi J W. 2019. Multi-material 3D printing of a soft pressure sensor. *Addit. Manuf.* **28**, 629–638.
[60] Khosravani M R and Reinicke T. 2020. 3D-printed sensors: current progress and future challenges. *Sens. Actuators A* **305**, 111916.
[61] Jaradat M, Soliman E and Reda Taha M. 2023. 3D-printed bio-inspired mechanically interlocked viscoelastic dampers for energy dissipation. *Mater. Des.* **228**, 111826.
[62] Mirhakimi A S, Dubey D and Elbestawi M A. 2024. Laser powder bed fusion of bio-inspired metamaterials for energy absorption applications: a review. *J. Mater. Res. Technol.* **31**, 2126–2155.
[63] Kumar R, Kumar M and Chohan J S. 2021. Material-specific properties and applications of additive manufacturing techniques: a comprehensive review. *Bull. Mater. Sci.* **44**, 181.
[64] Scheithauer U, Schwarzer-Fischer E, Sieder-Katzmann J, Propst M, Abel J, Gottlieb L, Weingarten S, Rebenklau L, Barth H and Bach C. 2024. Additive manufacturing of ceramic single and multi-material components–a groundbreaking innovation for space applications too? *Acta Astronaut.* **221**, 155–162.
[65] Rafiee M, Farahani R D and Therriault D. 2020. Multi-material 3D and 4D printing: a survey. *Adv. Sci.* **7**, 1902307.
[66] Zhu C, Gemeda H B, Duoss E B and Spadaccini C M. 2024. Toward multiscale, multimaterial 3D printing. *Adv. Mater.* **36**, 2314204.
[67] Lannunziata E, Mosallanejad M H, Galati M, Piscopo G and Saboori A. 2024. Analyzing the interplay of sintering conditions on microstructure and hardness in indirect additive manufacturing of 17-4PH stainless steel. *Acta Metall. Sin. (Engl. Lett.)* **37**, 1611–1620.
[68] Herzog D, Seyda V, Wycisk E and Emmelmann C. 2016. Additive manufacturing of metals. *Acta Mater.* **117**, 371–392.
[69] Mosallanejad M H, Abdi A, Karpasand F, Nassiri N, Iuliano L and Saboori A. 2023. Additive manufacturing of titanium alloys: processability, properties, and applications. *Adv. Eng. Mater.* **25**, 2301122.
[70] Oropeza D and Hart A J. 2021. A laboratory-scale binder jet additive manufacturing testbed for process exploration and material development. *Int. J. Adv. Manuf. Technol.* **114**, 3459–3473.
[71] Armstrong M, Mehrabi H A, Naveed N and Gregg C. 2023. Comparison analysis of energy consumption of atomic diffusion additive manufacturing with sand casting: towards a more sustainable future. *AIP Conf. Proc.* **2847**, 020001.
[72] Hu Y B and Cong W J. 2018. A review on laser deposition-additive manufacturing of ceramics and ceramic reinforced metal matrix composites. *Ceram. Int.* **44**, 20599–20612.
[73] Pragana J P M, Sampaio R F V, Bragança I M F, Silva C M A and Martins P A F. 2021. Hybrid metal additive manufacturing: a state–of–the-art review. *Adv. Ind. Manuf. Eng.* **2**, 100032.
[74] Maleki E, Bagherifard S, Bandini M and Guagliano M. 2021. Surface post-treatments for metal additive manufacturing: progress, challenges, and opportunities. *Addit. Manuf.* **37**, 101619.
[75] Mostafaei A, Elliott A M, Barnes J E, Li F Z, Tan W D, Cramer C L, Nandwana P and Chmielus M. 2021. Binder jet 3D printing—process parameters, materials, properties, modeling, and challenges. *Prog. Mater. Sci.* **119**, 100707.
[76] Sala V, Vandone A, Banfi M, Avram O, Mazzucato F, Baraldo S and Valente A. 2026. Layer-wise adaptive control of thin wall geometries in laser-powder direct energy deposition. *Addit. Manuf.* **115**, 105073.
[77] Clare A T, Woizeschke P, Rankouhi B, Pfefferkorn F E, Bartels D, Schmidt M and Wits W W. 2025. Metal multi-material additive manufacturing: overcoming barriers to implementation. *CIRP Ann.* **74**, 869–893.
[78] Svetlizky D, Das M, Zheng B L, Vyatskikh A L, Bose S, Bandyopadhyay A, Schoenung J M, Lavernia E J and Eliaz N. 2021. Directed energy deposition (DED) additive manufacturing: physical characteristics, defects, challenges and applications. *Mater. Today* **49**, 271–295.
[79] Dass A and Moridi A. 2019. State of the art in directed energy deposition: from additive manufacturing to materials design. *Coatings* **9**, 418.
[80] Saboori A, Aversa A, Marchese G, Biamino S, Lombardi M and Fino P. 2019. Application of directed energy deposition-based additive manufacturing in repair. *Appl. Sci.* **9**, 3316.
[81] Shamsaei N, Yadollahi A, Bian L K and Thompson S M. 2015. An overview of Direct Laser Deposition for additive manufacturing; Part II: mechanical behavior, process parameter optimization and control. *Addit. Manuf.* **8**, 12–35.
[82] Cui Y W, Wang L Q and Zhang L C. 2024. Towards load-bearing biomedical titanium-based alloys: from essential requirements to future developments. *Prog. Mater. Sci.* **144**, 101277.
[83] Zhang G D, Li N, Gao J S, Xiong H P, Yu H and Yuan H. 2022. Wire-fed electron beam directed energy deposition of Ti–6Al–2Zr–1Mo–1V alloy and the effect of annealing on the microstructure, texture, and anisotropy of tensile properties. *Addit. Manuf.* **49**, 102511.

[84] Yao M X, Yao Z J, Tao X W and Moliar O. 2020. Effect of deposition modes on electron beam directed energy deposited inconel 718. *Mater. Sci. Technol.* **36**, 1556–1565.
[85] Özel T, Shokri H and Loizeau R. 2023. A review on wire-fed directed energy deposition based metal additive manufacturing. *J. Manuf. Mater. Process.* **7**, 45.
[86] Ahn D G. 2021. Directed energy deposition (DED) process: state of the art. *Int. J. Precis. Eng. Manuf. Green Technol.* **8**, 703–742.
[87] Li K, Chen W, Gong N, Pu H Y, Luo J, Zhang D Z and Murr L E. 2023. A critical review on wire-arc directed energy deposition of high-performance steels. *J. Mater. Res. Technol.* **24**, 9369–9412.
[88] Li Z, Sui S, Ma X, Tan H, Zhong C L, Bi G J, Clare A T, Gasser A and Chen J. 2022. High deposition rate powder- and wire-based laser directed energy deposition of metallic materials: a review. *Int. J. Mach. Tools Manuf.* **181**, 103942.
[89] Han C J, Wang Y H, Wang Z C, Dong Z, Li K, Song C H, Cai C, Yan X C, Yang Y Q and Wang D. 2024. Enhancing mechanical properties of additively manufactured voronoi-based architected metamaterials via a lattice-inspired design strategy. *Int. J. Mach. Tools Manuf.* **202**, 104199.
[90] Zitelli C, Folgarait P and Di Schino A. 2019. Laser powder bed fusion of stainless steel grades: a review. *Metals* **9**, 731.
[91] Behjat A, Shamanian M, Sadeghi F, Mosallanejad M H and Saboori A. 2025. Process-driven structural and property evolution in laser powder bed fusion of a newly developed AISI 316L stainless steel. *Materials* **18**, 3343.
[92] Jadhav S D, Goossens L R, Kinds Y, Van Hooreweder B and Vanmeensel K. 2021. Laser-based powder bed fusion additive manufacturing of pure copper. *Addit. Manuf.* **42**, 101990 .
[93] Volpato G M, Tetzlaff U and Fredel M C. 2022. A comprehensive literature review on laser powder bed fusion of Inconel superalloys. *Addit. Manuf.* **55**, 102871.
[94] Kotadia H R, Gibbons G, Das A and Howes P D. 2021. A review of laser powder bed fusion additive manufacturing of aluminium alloys: microstructure and properties. *Addit. Manuf.* **46**, 102155.
[95] Dong Z, Han C J, Zhao Y Z, Huang J M, Ling C R, Hu G L, Wang Y H, Wang D, Song C H and Yang Y Q. 2024. Role of heterogenous microstructure and deformation behavior in achieving superior strength-ductility synergy in zinc fabricated via laser powder bed fusion. *Int. J. Extrem. Manuf.* **6**, 045003.
[96] Behjat A, Shamanian M, Iuliano L and Saboori A. 2024. Laser powder bed fusion in situ alloying of AISI 316L-2.5%Cu alloy: microstructure and mechanical properties evolution. *Prog. Addit. Manuf.* **9**, 2031–2039.
[97] Murr L E, Gaytan S M, Ramirez D A, Martinez E, Hernandez J, Amato K N, Shindo P W, Medina F R and Wicker R B. 2012. Metal fabrication by additive manufacturing using laser and electron beam melting technologies. *J. Mater. Sci. Technol.* **28**, 1–14.
[98] Caiazzo F, Alfieri V, Corrado G and Argenio P. 2017. Laser powder-bed fusion of Inconel 718 to manufacture turbine blades. *Int. J. Adv. Manuf. Technol.* **93**, 4023–4031.
[99] Behjat A, Saboori A, Galati M and Iuliano L. 2024. The electrochemical behaviour of Ti-48Al-2Cr-2Nb produced by electron beam powder bed fusion process. *Intermetallics* **175**, 108472.
[100] Depboylu F N, Yasa E, Poyraz Ö, Minguella-Canela J, Korkusuz F and De Los Santos López M A. 2022. Titanium based bone implants production using laser powder bed fusion technology. *J. Mater. Res. Technol.* **17**, 1408–1426.
[101] Behjat A, Sanaei S, Mosallanejad M H, Atapour M, Sheikholeslam M, Saboori A and Iuliano L. 2024. A novel titanium alloy for load-bearing biomedical implants: evaluating the antibacterial and biocompatibility of Ti536 produced via electron beam powder bed fusion additive manufacturing process. *Biomater. Adv.* **163**, 213928.
[102] Saboori A, Aversa A, Marchese G, Biamino S, Lombardi M and Fino P. 2020. Microstructure and mechanical properties of AISI 316L produced by directed energy deposition-based additive manufacturing: a review. *Appl. Sci.* **10**, 3310.
[103] Yan L, Chen Y T and Liou F. 2020. Additive manufacturing of functionally graded metallic materials using laser metal deposition. *Addit. Manuf.* **31**, 100901.
[104] Feenstra D R, Banerjee R, Fraser H L, Huang A, Molotnikov A and Birbilis N. 2021. Critical review of the state of the art in multi-material fabrication via directed energy deposition. *Curr. Opin. Solid State Mater. Sci.* **25**, 100924.
[105] Singh Tanwar R and Jhavar S. 2024. A review on additive manufacturing of SS-Ni multi-material fabrication. *Mater. Today Proc.* **102**, 24–30.
[106] Shah K, Ul Haq I, Khan A, Shah S A, Khan M and Pinkerton A J. 2014. Parametric study of development of Inconel-steel functionally graded materials by laser direct metal deposition. *Mater. Des. (1980-2015)* **54**, 531–538.
[107] Sun C, Wang Y, McMurtrey M D, Jerred N D, Liou F and Li J. 2021. Additive manufacturing for energy: a review. *Appl. Energy* **282**, 116041.
[108] Kim S H, Lee H, Yeon S M, Aranas C, Choi K, Yoon J, Yang S W and Lee H. 2021. Selective compositional range exclusion via directed energy deposition to produce a defect-free Inconel 718/SS 316L functionally graded material. *Addit. Manuf.* **47**, 102288.
[109] Lu J Y and Li W Y. 2023. Improvement of tensile properties of laser directed energy deposited IN718/316L functionally graded material via different heat treatments. *Mater. Sci. Eng. A* **866**, 144694.
[110] Li Y, Koukolíková M, Džugan J and Brázda M. 2024. High temperature fracture behavior of 316L stainless steel-Inconel 718 functionally graded materials manufactured by directed energy deposition: role of interface orientation and heat treatment. *Mater. Sci. Eng. A* **898**, 146389.
[111] Jeong T W, Cho Y T, Lee C M and Kim D H. 2024. Effects of ultrasonic treatment on mechanical properties and microstructure of stainless steel 308L and Inconel 718 functionally graded materials fabricated via double-wire arc additive manufacturing. *Mater. Sci. Eng. A* **896**, 146298.
[112] Zhang S Y, Dai H L, Li Y J, Zhang Z, Chen S, He M, Zhang B, Ma Y S and Chen X. 2024. Additive manufactured corrosion-resistant SS316L/IN625 functionally graded multi-material in hydrofluoric acid (HF) environment. *Corros. Sci.* **230**, 111926.
[113] Nie M H, Jiang P F, Zhou Y X, Li Y L and Zhang Z H. 2023. Studies on the 316/NiTi functionally gradient ultra-thick coatings fabricated with directed energy deposition: microstructure, crystallography and wear mechanism. *Appl. Surf. Sci.* **630**, 157497.
[114] Ghanavati R, Naffakh-Moosavy H, Moradi M, Mazzucato F, Valente A, Bagherifard S and Saboori A. 2025. Design optimization for defect-free AISI 316 L/IN718 functionally graded materials produced by laser additive manufacturing. *Mater. Charact.* **220**, 114697.
[115] Bobbio L D, Bocklund B, Otis R, Borgonia J P, Dillon R P, Shapiro A A, Mcenerney B, Liu Z K and Beese A M. 2018. Characterization of a functionally graded material of Ti-6Al-4V to 304L stainless steel with an intermediate V section. *J. Alloys Compd.* **742**, 1031–1036.
[116] Adomako N K, Lewandowski J J, Arkhurst B M, Choi H, Chang H J and Kim J H. 2022. Microstructures and mechanical properties of multi-layered materials composed

of Ti-6Al-4V, vanadium, and 17-4PH stainless steel produced by directed energy deposition. *Addit. Manuf.* **59**, 103174.
[117] Bobbio L D, Bocklund B, Simsek E, Ott R T, Kramer M J, Liu Z K and Beese A M. 2022. Design of an additively manufactured functionally graded material of 316 stainless steel and Ti-6Al-4V with Ni-20Cr, Cr, and V intermediate compositions. *Addit. Manuf.* **51**, 102649.
[118] Huang J K, Liu G Y, Yu X Q, Guan Z C, Yu S R and Fan D. 2022. Characterization of nickel-titanium alloy graded materials using double wire alternating current cross arc additive manufacturing. *J. Alloys Compd.* **910**, 164912.
[119] Park C W, Hajra R N, Kim S H, Lee S H and Kim J H. 2023. Optimizing multi-interlayered additive manufacturing for high strength robust joints in Inconel 718 and Ti–6Al–4V alloys. *J. Mater. Res. Technol.* **25**, 855–872.
[120] Wu D J, Song C C, Di T D, Niu F Y and Ma G Y. 2022. Intermetallic regulation mechanism of inconel 718/Ti6Al4V composite by novel follow-up ultrasonic assisted laser additive manufacturing. *Composites B* **235**, 109736.
[121] Zhang Y N and Bandyopadhyay A. 2018. Direct fabrication of compositionally graded Ti-Al_2O_3 multi-material structures using Laser Engineered Net Shaping. *Addit. Manuf.* **21**, 104–111.
[122] Gualtieri T and Bandyopadhyay A. 2018. Additive manufacturing of compositionally gradient metal-ceramic structures: stainless steel to vanadium carbide. *Mater. Des.* **139**, 419–428.
[123] Ostolaza M, Zabala A, Arrizubieta J I, Llavori I, Otegi N and Lamikiz A. 2024. High-temperature tribological performance of functionally graded Stellite 6/WC metal matrix composite coatings manufactured by laser-directed energy deposition. *Friction* **12**, 522–538.
[124] Zhang J H, Wang L L, Zhao K, Qi C Q, Shi B W, Zhang Y X, Yuan S C and Zhan X H. 2024. Thermal analysis and microstructure evolution of TiC/Ti6Al4V functionally graded material by direct energy deposition. *Mater. Sci. Eng. A* **893**, 146136.
[125] Melzer D, Džugan J, Koukolíková M, Rzepa S and Vavřík J. 2021. Structural integrity and mechanical properties of the functionally graded material based on 316L/IN718 processed by DED technology. *Mater. Sci. Eng. A* **811**, 141038.
[126] Ghanavati R, Naffakh-Moosavy H and Moradi M. 2021. Additive manufacturing of thin-walled SS316L-IN718 functionally graded materials by direct laser metal deposition. *J. Mater. Res. Technol.* **15**, 2673–2685.
[127] Li K, Zhan J B, Zhang M, Ma R J, Tang Q, Zhang D Z, Murr L E and Cao H J. 2022. A functionally graded material design from stainless steel to Ni-based superalloy by laser metal deposition coupled with thermodynamic prediction. *Mater. Des.* **217**, 110612.
[128] Xu G, Wu R B, Luo K Y and Lu J Z. 2022. Effects of heat treatment on hot corrosion behavior of directed energy deposited In718/316L functionally graded material. *Corros. Sci.* **197**, 110068.
[129] Tong X Y, Lu C X, Huang Z F, Zhang C and Chen F. 2022. Microstructures and mechanical properties of crack-free 316L stainless steel and Inconel 625 joint by using Laser Engineered Net Shaping. *Opt. Laser Technol.* **155**, 108357.
[130] Li X R, Li Q, Nie M H, Kong D Y, Liu Z L and Zhang Z H. 2023. Evading the strength-ductility trade-off dilemma in steel-nickel heterostructured material by bionic crossed-lamellar structures. *Virtual Phys. Prototyp.* **18**, e2266640.
[131] Fan H Y, Shi Q M, Wang C C, Tian Y J, Zhou K and Yang S F. 2023. Laser powder bed fusion of bimetallic stainless steel/Nickel-based superalloy: interface and mechanical properties. *Mater. Sci. Eng. A* **877**, 145193.
[132] Rajesh Kannan A, Mohan Kumar S, Pravin Kumar N, Siva Shanmugam N, Vishnu A S and Palguna Y. 2020. Process-microstructural features for tailoring fatigue strength of wire arc additive manufactured functionally graded material of SS904L and Hastelloy C-276. *Mater. Lett.* **274**, 127968.
[133] Ferreira A A, Emadinia O, Cruz J M, Reis A R and Vieira M F. 2021. Inconel 625/AISI 413 stainless steel functionally graded material produced by direct laser deposition. *Materials* **14**, 5595.
[134] Senthil T S, Ramesh Babu S, Puviyarasan M and Dhinakaran V. 2021. Mechanical and microstructural characterization of functionally graded Inconel 825—SS316L fabricated using wire arc additive manufacturing. *J. Mater. Res. Technol.* **15**, 661–669.
[135] Bobbio L D, Bocklund B, Liu Z K and Beese A M. 2021. Tensile behavior of stainless steel 304L to Ni-20Cr functionally graded material: experimental characterization and computational simulations. *Materialia* **18**, 101151.
[136] Aydogan B, O'Neil A and Sahasrabudhe H. 2021. Microstructural and mechanical characterization of stainless steel 420 and Inconel 718 multi-material structures fabricated using laser directed energy deposition. *J. Manuf. Process.* **68**, 1224–1235.
[137] Dang X F, Li Y, Chen K, Luo S H, Liang X Q and He W F. 2022. Insight into the interfacial architecture of a hybrid additively- manufactured stainless steel/Ni-based superalloy bimetal. *Mater. Des.* **216**, 110595.
[138] Li T X, Wang Z J, Hu S S, Yang Z W and Wang Y. 2022. Hot cracking during the fabrication of Inconel 625/stainless steel 308 L functionally graded material by dual-wire arc additive manufacturing. *J. Manuf. Process.* **82**, 461–473.
[139] Zhang S P, Song Z M, Hu Y B, Yan Z P, Di R F and Lei J B. 2023. 18Ni300/Inconel 625 alloy gradient materials fabricated by directed energy deposition. *Mater. Today Commun.* **37**, 107185.
[140] Li W, Karnati S, Kriewall C, Liou F, Newkirk J, Brown Taminger K M and Seufzer W J. 2017. Fabrication and characterization of a functionally graded material from Ti-6Al-4V to SS316 by laser metal deposition. *Addit. Manuf.* **14**, 95–104.
[141] Xu G, Wu L J, Su Y Y, Wang Z F, Luo K Y and Lu J Z. 2022. Microstructure and mechanical properties of directed energy deposited 316L/Ti6Al4V functionally graded materials via constant/gradient power. *Mater. Sci. Eng. A* **839**, 142870.
[142] Xu G, Song C C, Zhang H M, Lu H F, Wu D J, Luo K Y and Lu J Z. 2022. Spatially heterogeneous microstructure in in-situ TiO-reinforced Ti6Al4V/316L functionally graded material fabricated via directed energy deposition. *Addit. Manuf.* **59**, 103178.
[143] Dharmendra C, Shakerin S, Ram G D J and Mohammadi M. 2020. Wire-arc additive manufacturing of nickel aluminum bronze/stainless steel hybrid parts—interfacial characterization, prospects, and problems. *Materialia* **13**, 100834.
[144] Osipovich K, Vorontsov A, Chumaevskii A, Gurianov D, Shamarin N, Savchenko N and Kolubaev E. 2021. Characterization of a bimetallic multilayered composite "stainless steel/copper" fabricated with wire-feed electron beam additive manufacturing. *Metals* **11**, 1151.
[145] Zhang X C, Li L and Liou F. 2021. Additive manufacturing of stainless steel—copper functionally graded materials via Inconel 718 interlayer. *J. Mater. Res. Technol.* **15**, 2045–2058.
[146] Tomar B and Shiva S. 2024. Microstructural and mechanical properties examination of SS316L-Cu functionally graded material fabricated by wire arc additive manufacturing. *CIRP J. Manuf. Sci. Technol.* **50**, 26–39.

[147] Zhang X C, Sun C, Pan T, Flood A, Zhang Y L, Li L and Liou F. 2020. Additive manufacturing of copper—H13 tool steel bi-metallic structures via Ni-based multi-interlayer. *Addit. Manuf.* **36**, 101474.
[148] Fan W, Zhang C, Tan H, Wang Y X, Peng Y J, Zhang F Y, Lin X and Huang W D. 2022. Microstructures and mechanical properties of Invar/MnCu functionally graded material fabricated by directed energy deposition. *Mater. Sci. Eng. A* **860**, 144332.
[149] Nie J J, Wei L, Li D L, Zhao L, Jiang Y and Li Q. 2020. High-throughput characterization of microstructure and corrosion behavior of additively manufactured SS316L-SS431 graded material. *Addit. Manuf.* **35**, 101295.
[150] Ben-Artzy A, Reichardt A, Borgonia J P, Dillon R P, McEnerney B, Shapiro A A and Hosemann P. 2021. Compositionally graded SS316 to C300 Maraging steel using additive manufacturing. *Mater. Des.* **201**, 109500.
[151] Oropeza D, Firdosy S and Hofmann D C. 2022. Development of in-plane SS316 to M300 maraging steel gradients via directed energy deposition. *Addit. Manuf. Lett.* **3**, 100078.
[152] Shin G et al. 2023. Microstructural evolution and mechanical properties of functionally graded austenitic–low-carbon steel produced via directed energy deposition. *Mater. Des.* **227**, 111681.
[153] Zhai W G, Aishwarya, Shandro R and Zhou W. 2024. Microstructure and mechanical properties of the wire arc additively manufactured 316L/ER70S-6 bimetal structure. *Virtual Phys. Prototyp.* **19**, e2375105.
[154] Koukolíková M, Podaný P, Rzepa S, Brázda M and Kocijan A. 2023. Additive manufacturing multi-material components of SAF 2507 duplex steel and 15-5 PH martensitic stainless steel. *J. Manuf. Process.* **102**, 330–339.
[155] Han J, Lu L Z, Xin Y, Chen X Y, Zhang G Y, Cai Y C and Tian Y B. 2022. Microstructure and mechanical properties of a novel functionally graded material from Ti6Al4V to Inconel 625 fabricated by dual wire + arc additive manufacturing. *J. Alloys Compd.* **903**, 163981.
[156] Mishra A, Raj Paul A, Sharma R, Mukherjee M and Kumar Singh R. 2023. Interfacial characteristics of Ti6Al4V-IN718 dissimilar structure developed by wire-arc additive manufacturing using Monel-400 as an interlayer. *Mater. Today: Proc.* **80**, 241–247.
[157] Jeong H I, Kim D H and Lee C M. 2024. Multi-material deposition of Inconel 718 and Ti–6Al–4V using the Ti–Nb–Cr–V–Ni high entropy alloy intermediate layer. *J. Mater. Res. Technol.* **29**, 3217–3227.
[158] Li X R, Li Q, Nie M H, Jiang P F, Yan S H, Jiang Y and Zhang Z H. 2025. Constructing the discrete gradient structure for enhancing interfacial bond strength of Ti6Al4V/NiTi heterostructured materials. *J. Mater. Sci. Technol.* **214**, 266–271.
[159] Onuike B, Heer B and Bandyopadhyay A. 2018. Additive manufacturing of Inconel 718—copper alloy bimetallic structure using laser engineered net shaping (LENS^{TM}). *Addit. Manuf.* **21**, 133–140.
[160] Grandhi M, Nguyen V, Liu Z C, Romo-de-la-cruz C O and Song X Y. 2023. Copper-nickel functionally magnetic gradient material fabricated via directed energy deposition. *J. Manuf. Process.* **100**, 47–54.
[161] Wang Y H, Konovalov S, Chen X Z, Singh R A and Jayalakshmi S. 2022. Research on plasma arc additive manufacturing of Inconel 625 Ni–Cu functionally graded materials. *Mater. Sci. Eng. A* **853**, 143796.
[162] Liu K, Yan Z Y, Pan R, Wang X W, Wang F D and Chen S J. 2024. Interfacial bonding and microstructural evolution in Inconel-copper bimetallic structures fabricated by directed energy deposition-arc. *Mater. Sci. Eng. A* **898**, 146381.
[163] Liu Y, Liu C, Liu W S, Ma Y Z, Zhang C, Cai Q S and Liu B. 2018. Microstructure and properties of Ti/Al lightweight graded material by direct laser deposition. *Mater. Sci. Technol.* **34**, 945–951.
[164] Wang J, Pan Z X, Ma Y, Lu Y, Shen C, Cuiuri D and Li H J. 2018. Characterization of wire arc additively manufactured titanium aluminide functionally graded material: microstructure, mechanical properties and oxidation behaviour. *Mater. Sci. Eng. A* **734**, 110–119.
[165] Ma R X, Liu Z Q, Wang W B, Xu G J and Wang W. 2020. Laser deposition melting of TC4/TiAl functionally graded material. *Vacuum* **177**, 109349.
[166] Zhang D Q, Du D, Pu Z, Xue S, Qi J J and Chang B H. 2023. Interfacial microstructure and stress characteristics of laser-directed energy deposited AA2024 on Ti6Al4V substrate. *Opt. Laser Technol.* **164**, 109521.
[167] Zhang D Q, Du D, Pu Z, Xue S, Qi J J and Chang B H. 2024. Laser-directed energy deposition of Ti6Al4V/AA2024 alloy component based on interweaving structure. *Mater. Lett.* **363**, 136275.
[168] Tonyali B, Sun H, Liu Z K, Keist J and Beese A M. 2024. Tailoring the coefficient of thermal expansion in a functionally graded material: al alloyed with Ti-6Al-4V using additive manufacturing. *J. Alloys Compd.* **1009**, 176971.
[169] Li N, Liu W, Xiong H P, Qin R Y, Huang S, Zhang G H and Gao C. 2019. In-situ reaction of Ti-Si-C composite powder and formation mechanism of laser deposited Ti6Al4V/($TiC+Ti_3SiC_2$) system functionally graded material. *Mater. Des.* **183**, 108155.
[170] Savitha U, Reddy G J, Singh V, Gokhale A A and Sundararaman M. 2020. Additive laser deposition of compositionally graded NiCrAlY-YSZ multi-materials on IN625-NiCrAlY substrate. *Mater. Charact.* **164**, 110317.
[171] Zheng W H, Zhang D B, Wu D S, Ma N S and Geng P H. 2023. Effects of ceramic material in laser-directed energy deposition of titanium/ceramic functionally graded materials. *J. Mater. Process. Technol.* **317**, 117992.
[172] Sun J X, Wang J, Zeng D X, Li W F, Jin S X, Qiu F and Shen P. 2024. Dual-gradient ceramic/aluminum composite structure fabricated by arc additive manufacturing with co-conveying of wire and powder. *Mater. Res. Lett.* **12**, 390–397.
[173] Wang Y, Li Y, Wang H Y, Yu W, He C, Xu G M, Li J D and Tang H Q. 2024. Composition design and mechanical properties of B_4C/Al-Zn-Mg-Cu functionally graded materials prepared by laser additive manufacturing. *J. Mater. Res. Technol.* **32**, 3620–3629.
[174] Schneider-Maunoury C, Weiss L, Acquier P, Boisselier D and Laheurte P. 2017. Functionally graded Ti6Al4V-Mo alloy manufactured with DED-CLAD® process. *Addit. Manuf.* **17**, 55–66.
[175] Schneider-Maunoury C, Weiss L, Perroud O, Joguet D, Boisselier D and Laheurte P. 2019. An application of differential injection to fabricate functionally graded Ti-Nb alloys using DED-CLAD® process. *J. Mater. Process. Technol.* **268**, 171–180.
[176] Thomas J, Mogonye J E, Mantri S A, Choudhuri D, Banerjee R and Scharf T W. 2020. Additive manufacturing of compositionally graded laser deposited titanium-chromium alloys. *Addit. Manuf.* **33**, 101132.
[177] Luo K Y, Li S H, Xu G, Hosseini S R E and Lu J Z. 2022. Hot corrosion behaviors of directed energy deposited Inconel 718/Haynes 25 functionally graded material at 700 °C and 900 °C. *Corros. Sci.* **197**, 110040.
[178] Huang S Y, Shen C, An K, Zhang Y X, Spinelli I, Brennan M and Yu D J. 2022. Residual stress and microstructure in IN718-René41 graded superalloy fabricated by laser blown directed energy deposition. *Front. Met. Alloys* **1**, 1070562.

[179] MacDonald B E, Zheng B L, Fields B, Wang X, Jiang S, Cao P H, Valdevit L, Lavernia E J and Schoenung J M. 2023. Influence of co-deposition strategy on the mechanical behavior of additively manufactured functionally integrated materials. *Addit. Manuf.* **61**, 103328.
[180] Nandi S K, Matthews A, Withers P J, Stermsek J, Fuchs C, Roy S and Manna I. 2024. Functionally graded Tribaloy^{TM} T800 and austenitic stainless steel by laser additive manufacturing. *Mater. Today Commun.* **39**, 109274.
[181] Karim A, Jadhav S, Kannan R, Pierce D, Lee Y, Nandwana P and Kim D B. 2024. Investigating stainless steel/aluminum bimetallic structures fabricated by cold metal transfer (CMT)-based wire-arc directed energy deposition. *Addit. Manuf.* **81**, 104015.
[182] Kim T G, Shin G Y and Shim D S. 2022. Study on the interfacial characteristics and crack propagation of 630 stainless steel fabricated by hybrid additive manufacturing (additional DED building on L-PBFed substrate). *Mater. Sci. Eng. A* **835**, 142657.
[183] Wang J H, Yuan D, Sun X J, Zhang Z, Yang Z L and Wei C. 2025. Effect of deposition sequence on interface characteristics of IN718/CuSn10 horizontal bimetallic structures via laser directed energy deposition. *Mater. Des.* **255**, 114085.
[184] Iams A D, Lienert T J, Otazu D A and Ramoni M. 2023. Effects of deposition sequence on microstructural evolution in additively manufactured Cu-Cr-Nb alloy/superalloy bimetallic structures. *Addit. Manuf. Lett.* **6**, 100151.
[185] Chang T X, Fang X W, Zhou Y, Zhang H K, Xi N Y, Ghafoor S and Huang K. 2025. Heterogeneous interfaces of aluminum bronze/Inconel 718 dissimilar alloys under different wire arc directed energy deposition sequences. *Int. J. Extrem. Manuf.* **7**, 015003.
[186] Liu L Q, Wang D, Wang T Y, Han C J, Li Y, Tan H, Zhou W, Yan X C, Lei L M and Yang Y Q. 2025. Laser additive manufacturing of multimaterials with hierarchical interlocking interface via a flexible scraper-based method. *Int. J. Mach. Tools Manuf.* **205**, 104236.
[187] Squires L, Roberts E and Bandyopadhyay A. 2023. Radial bimetallic structures via wire arc directed energy deposition-based additive manufacturing. *Nat. Commun.* **14**, 3544.
[188] Wei C, Liu L C, Gu Y C, Huang Y H, Chen Q, Li Z Q and Li L. 2022. Multi-material additive-manufacturing of tungsten—copper alloy bimetallic structure with a stainless-steel interlayer and associated bonding mechanisms. *Addit. Manuf.* **50**, 102574.
[189] Jing Y D, Fang X W, Geng Y L, Duan Y S and Huang K. 2023. Simultaneous strength and ductility enhancement of wire-arc directed energy deposited Al-Cu alloy by interlayer laser shock peening. *Mater. Sci. Eng. A* **887**, 145699.
[190] Chang T X, Zhang H W, Fang X W, Ma M H, Zheng S M, Lu B H and Huang K. 2025. Tailoring interface properties in wire-arc directed energy deposited dissimilar aluminum alloys through interlayer laser shock peening. *Virtual Phys. Prototyp.* **20**, e2469155.
[191] Ma Z Y et al. 2024. Additive manufacturing of functional gradient materials: a review of research progress and challenges. *J. Alloys Compd.* **971**, 172642.
[192] Liu L Q et al. 2024. Additive manufacturing of multi-materials with interfacial component gradient by in-situ powder mixing and laser powder bed fusion. *J. Alloys Compd.* **978**, 173508.
[193] Chen J, Zhang M K, Zhao D K, Bi G J, Bai Y C, Xiao Y M and Wang D. 2024. The impact of interfacial characteristics on the interfacial properties of 316 L/CuSn10 multi-material manufactured by laser powder bed fusion. *Mater. Charact.* **211**, 113862.
[194] Chen K Y, Wang C, Hong Q F, Wen S F, Zhou Y, Yan C Z and Shi Y S. 2020. Selective laser melting 316L/CuSn10 multi-materials: processing optimization, interfacial characterization and mechanical property. *J. Mater. Process. Technol.* **283**, 116701.
[195] Oel M, Rossmann J, Bode B, Meyer I, Ehlers T, Hackl C M and Lachmayer R. 2023. Multi-material laser powder bed fusion additive manufacturing of concentrated wound stator teeth. *Addit. Manuf. Lett.* **7**, 100165.
[196] Wang D et al. 2025. Recent advances on additive manufacturing of heterogeneous/gradient metallic materials via laser powder bed fusion. *Int. J. Extrem. Manuf.* **7**, 062007.
[197] Li X S, Pan Z H, Smolej L, Karthik Nadimpalli V and Moshiri M. 2024. Towards manufacturing intra-layer multi-material mould tools with vertical interfaces using laser-based powder bed fusion. *Mater. Des.* **243**, 113056.
[198] Bai Y C, Zhao C L, Zhang Y and Wang H. 2021. Microstructure and mechanical properties of additively manufactured multi-material component with maraging steel on CrMn steel. *Mater. Sci. Eng. A* **802**, 140630.
[199] Guo H W, Liu D Y, Xu M C, Dong Z C and Zhang L J. 2024. Preparation, characterization and composition optimization design of laser powder bed fusion continuously graded Invar36/316L stainless steel alloys. *Mater. Charact.* **209**, 113709.
[200] Pan Z H, Nadimpalli V K, Funch C V, Andersen S A, Zhou L C, Kjer M B, Christiansen T L and Zhang Y B. 2024. Microstructural evolution of multilayered AISI 316L-440C steel composites manufactured by laser powder bed fusion. *Mater. Charact.* **211**, 113907.
[201] Griffis J C, Shahed K, Meinert K, Yilmaz B, Lear M and Manogharan G. 2025. Multi-material laser powder bed fusion: effects of build orientation on defects, material structure and mechanical properties. *npj Adv. Manuf.* **2**, 5.
[202] Li L, Shi Q M and Yang S F. 2025. In-situ bonding of horizontal bimetallic interface by laser offset during laser powder bed fusion of copper/nickel multi-material structures and underlying thermodynamic mechanisms. *J. Mater. Process. Technol.* **339**, 118831.
[203] Knörlein J, Franke M M, Schloffer M and Körner C. 2022. In-situ aluminum control for titanium aluminide via electron beam powder bed fusion to realize a dual microstructure. *Addit. Manuf.* **59**, 103132.
[204] Knörlein J, Franke M M, Schloffer M, Berger T and Körner C. 2023. Microstructure and mechanical properties of additively manufactured γ-TiAl with dual microstructure. *Intermetallics* **161**, 107978.
[205] Bartolomeu F, Costa M M, Alves N, Miranda G and Silva F S. 2020. Additive manufacturing of NiTi-Ti6Al4V multi-material cellular structures targeting orthopedic implants. *Opt. Lasers Eng.* **134**, 106208.
[206] Chen J, Yang Y Q, Song C H, Zhang M K, Wu S B and Wang D. 2019. Interfacial microstructure and mechanical properties of 316L /CuSn10 multi-material bimetallic structure fabricated by selective laser melting. *Mater. Sci. Eng. A* **752**, 75–85.
[207] Mao S L, Zhang D Z, Ren Z H, Fu G and Ma X Y. 2022. Effects of process parameters on interfacial characterization and mechanical properties of 316L/CuCrZr functionally graded material by selective laser melting. *J. Alloys Compd.* **899**, 163256.
[208] Kuai Z Z, Li Z H, Liu B, Chen Y L, Li H D and Bai P K. 2023. Microstructure and mechanical properties of CuCrZr/316L hybrid components manufactured using selective laser melting. *J. Alloys Compd.* **955**, 170103.
[209] Deillon L, Abando Beldarrain N, Li X and Bambach M. 2024. Coupling hot isostatic pressing and laser powder bed fusion: a new strategy to manufacture defect-free

CuCrZr-316L steel multi-material structures. *Mater. Des.* **241**, 112914.
[210] Martendal C P, Esteves P D B, Deillon L, Malamud F, Jamili A M, Löffler J F and Bambach M. 2024. Effects of beam shaping on copper-steel interfaces in multi-material laser beam powder bed fusion. *J. Mater. Process. Technol.* **327**, 118344.
[211] Liu Z H, Zhang D Q, Sing S L, Chua C K and Loh L E. 2014. Interfacial characterization of SLM parts in multi-material processing: metallurgical diffusion between 316L stainless steel and C18400 copper alloy. *Mater. Charact.* **94**, 116–125.
[212] Bai Y C, Zhang J Y, Zhao C L, Li C J and Wang H. 2020. Dual interfacial characterization and property in multi-material selective laser melting of 316L stainless steel and C52400 copper alloy. *Mater. Charact.* **167**, 110489.
[213] Tan C L, Chew Y, Bi G J, Wang D, Ma W Y, Yang Y Q and Zhou K S. 2021. Additive manufacturing of steel–copper functionally graded material with ultrahigh bonding strength. *J. Mater. Sci. Technol.* **72**, 217–222.
[214] Wei C, Gu H, Li Q, Sun Z, Chueh Y H, Liu Z and Li L. 2021. Understanding of process and material behaviours in additive manufacturing of Invar36/Cu10Sn multiple material components via laser-based powder bed fusion. *Addit. Manuf.* **37**, 101683.
[215] Hinojos A, Mireles J, Reichardt A, Frigola P, Hosemann P, Murr L E and Wicker R B. 2016. Joining of Inconel 718 and 316 Stainless Steel using electron beam melting additive manufacturing technology. *Mater. Des.* **94**, 17–27.
[216] Mei X L, Wang X Y, Peng Y B, Gu H Y, Zhong G Y and Yang S F. 2019. Interfacial characterization and mechanical properties of 316L stainless steel/inconel 718 manufactured by selective laser melting. *Mater. Sci. Eng. A* **758**, 185–191.
[217] Chen W Y, Zhang X, Li M M, Xu R Q, Zhao C and Sun T. 2020. Laser powder bed fusion of Inconel 718 on 316 stainless steel. *Addit. Manuf.* **36**, 101500.
[218] Yusuf S M, Zhao X, Yang S F and Gao N. 2021. Interfacial characterisation of multi-material 316L stainless steel/Inconel 718 fabricated by laser powder bed fusion. *Mater. Lett.* **284**, 128928.
[219] Wits W W and Amsterdam E. 2021. Graded structures by multi-material mixing in laser powder bed fusion. *CIRP Ann.* **70**, 159–162.
[220] Duval-Chaneac M S, Gao N, Khan R H U, Giles M, Georgilas K, Zhao X and Reed P A S. 2021. Fatigue crack growth in IN718/316L multi-materials layered structures fabricated by laser powder bed fusion. *Int. J. Fatigue* **152**, 106454.
[221] Wen Y J, Gao J B, Narayan R L, Wang P, Zhang L J, Zhang B C, Ramamurty U and Qu X H. 2023. Microstructure-property correlations in as-built and heat-treated compositionally graded stainless steel 316L-Inconel 718 alloy fabricated by laser powder bed fusion. *Mater. Sci. Eng. A* **862**, 144515.
[222] Errico V, Posa P, Fusco A, Angelastro A and Campanelli S L. 2023. Intralayer multi-material structure stainless-steel/nickel-superalloy fabricated via laser-powder bed fusion process. *Manuf. Lett.* **35**, 11–15.
[223] Ghanavati R, Saboori A, Gadalińska E, Bagherifard S and Iuliano L. 2025. Laser powder bed fusion of SS316L-IN718 functionally graded materials: processing, microstructure, and properties. *Mater. Sci. Eng. A* **934**, 148341.
[224] Rankouhi B, Islam Z, Pfefferkorn F E and Thoma D J. 2022. Characterization of multi-material 316L-Hastelloy X fabricated via laser powder-bed fusion. *Mater. Sci. Eng. A* **837**, 142749.
[225] Hengsbach F et al. 2018. Inline additively manufactured functionally graded multi-materials: microstructural and mechanical characterization of 316L parts with H13 layers. *Prog. Addit. Manuf.* **3**, 221–231.
[226] Shakerin S, Sanjari M, Amirkhiz B S and Mohammadi M. 2020. Interface engineering of additively manufactured maraging steel-H13 bimetallic structures. *Mater. Charact.* **170**, 110728.
[227] Demir A G, Kim J, Caltanissetta F, Hart A J, Tasan C C, Previtali B and Colosimo B M. 2022. Enabling multi-material gradient structure in laser powder bed fusion. *J. Mater. Process. Technol.* **301**, 117439.
[228] McDonnell B, Errico V, Posa P, Angelastro A, Furman A, O'Hara E, Campanelli S L and Harrison N. 2024. Bi-metallic lattice structures manufactured via an intralayer multi-material powder bed fusion method. *Addit. Manuf.* **89**, 104301.
[229] Chen C Y, Gu D D, Dai D H, Du L, Wang R, Ma C L and Xia M J. 2019. Laser additive manufacturing of layered TiB_2/Ti6Al4V multi-material parts: understanding thermal behavior evolution. *Opt. Laser Technol.* **119**, 105666.
[230] Polozov I, Gracheva A and Popovich A. 2022. Interface characterization of bimetallic Ti-6Al-4V/Ti2AlNb structures prepared by selective laser melting. *Materials* **15**, 8528.
[231] Shi X Z, Wang Z, Li Z H, Pavlenko P and Li P F. 2024. Eliminating cracks in Ti–47Al–2Cr–2Nb/Ti–6Al–4V micro-laminated composites fabricated by dual-material laser powder bed fusion. *J. Mater. Res. Technol.* **30**, 8599–8607.
[232] Sing S L, Lam L P, Zhang D Q, Liu Z H and Chua C K. 2015. Interfacial characterization of SLM parts in multi-material processing: intermetallic phase formation between AlSi10Mg and C18400 copper alloy. *Mater. Charact.* **107**, 220–227.
[233] Demir A G and Previtali B. 2017. Multi-material selective laser melting of Fe/Al-12Si components. *Manuf. Lett.* **11**, 8–11.
[234] Wu X P, Zhang D Y, Yi D H, Hu S T, Huang G L, Poprawe R and Schleifenbaum J H. 2022. Interfacial characterization and reaction mechanism of Ti/Al multi-material structure during laser powder bed fusion process. *Mater. Charact.* **192**, 112195.
[235] Daram P, Singh A, Hiroto T, Kitashima T and Watanabe M. 2024. Compositionally graded titanium to aluminum processed by laser powder bed fusion process: microstructure evolution and mechanical properties. *Mater. Sci. Eng. A* **903**, 146638.
[236] Miao H, Yusof F, Ab Karim M S, Wu B, Raja S, Ibrahim M Z, Aziz I and Chen D L. 2023. Interfacial microstructure, element diffusion, mechanical properties and metallurgical bonding mechanism of 316L-AlSi10Mg multi-material parts fabricated by laser powder bed fusion. *J. Mater. Res. Technol.* **26**, 8351–8365.
[237] Zhou Y, Duan L C, Li F, Chen K Y and Wen S F. 2022. Effect of heat treatment on the microstructure and mechanical property of W/316L multi-material fabricated by selective laser melting. *J. Alloys Compd.* **890**, 161841.
[238] Wu Q L, Wang X Q, Li K F, Zhou Y, Wen S F and Shi Y S. 2024. Microstructure and mechanical properties of Ti6Al4V/W bimetallic structure via selective laser melting. *Int. J. Refract. Met. Hard Mater.* **121**, 106683.
[239] Xie Z R, Zhou Y, Wang X Q, Chen K Y, Wang R F, Wen S F, Che Y S, Shi Y S and He J L. 2024. Interfacial characterization and bonding mechanism of W/ODS-316 L steel multi-material structure fabricated by laser powder bed fusion. *Mater. Charact.* **216**, 114242.
[240] Han C J, Li Y, Wang Q, Cai D S, Wei Q S, Yang L, Wen S F, Liu J and Shi Y S. 2018. Titanium/hydroxyapatite (Ti/HA) gradient materials with quasi-continuous ratios fabricated by SLM: material interface and fracture toughness. *Mater. Des.* **141**, 256–266.

[241] Zhang X J, Chueh Y H, Wei C, Sun Z, Yan J W and Li L. 2020. Additive manufacturing of three-dimensional metal-glass functionally gradient material components by laser powder bed fusion with *in situ* powder mixing. *Addit. Manuf.* **33**, 101113.
[242] Rock C, Lara-Curzio E, Ellis B, Ledford C, Leonard D N, Kannan R, Kirka M and Horn T. 2020. Additive manufacturing of pure Mo and Mo + TiC MMC alloy by electron beam powder bed fusion. *JOM* **72**, 4202–4213.
[243] Tey C F, Tan X P, Sing S L and Yeong W Y. 2020. Additive manufacturing of multiple materials by selective laser melting: ti-alloy to stainless steel via a Cu-alloy interlayer. *Addit. Manuf.* **31**, 100970.
[244] Ekoi E J, Degli-Alessandrini G, Zeeshan Mughal M, Vijayaraghavan R K, Obeidi M A, Groarke R, Kraev I, Krishnamurthy S and Brabazon D. 2022. Investigation of the microstructure and phase evolution across multi-material $Ni_{50.83}Ti_{49.17}$-AISI 316L alloy interface fabricated using laser powder bed fusion (L-PBF). *Mater. Des.* **221**, 110947.
[245] Xu D M, Yang W X, Behera M P, Singamneni S, Hodgson M A and Cao P. 2024. Creating heterostructures via laser powder bed fusion using titanium and stainless steel mixtures. *Mater. Sci. Eng. A* **915**, 147260.
[246] Scaramuccia M G, Demir A G, Caprio L, Tassa O and Previtali B. 2020. Development of processing strategies for multigraded selective laser melting of Ti6Al4V and IN718. *Powder Technol.* **367**, 376–389.
[247] Wei C et al. 2022. Cu10Sn to Ti6Al4V bonding mechanisms in laser-based powder bed fusion multiple material additive manufacturing with different build strategies. *Addit. Manuf.* **51**, 102588.
[248] Daram P, Hiroto T and Watanabe M. 2023. Microstructure and phase evolution of functionally graded multi-materials of Ni–Ti alloy fabricated by laser powder bed fusion process. *J. Mater. Res. Technol.* **23**, 5559–5572.
[249] Lubkowitz V, Fischmann P, Schulze V and Zanger F. 2022. Influence of initial powder layer thickness and focus deviation on the properties of hybrid manufactured parts by Laser Powder Bed Fusion. *Proc. CIRP* **111**, 87–91.
[250] Wu Z H, Wilson-Heid A E, Griffiths R J and Elton E S. 2023. A review on experimentally observed mechanical and microstructural characteristics of interfaces in multi-material laser powder bed fusion. *Front. Mech. Eng.* **9**, 1087021.
[251] Svetlizky D, Zheng B L, Vyatskikh A, Das M, Bose S, Bandyopadhyay A, Schoenung J M, Lavernia E J and Eliaz N. 2022. Laser-based directed energy deposition (DED-LB) of advanced materials. *Mater. Sci. Eng. A* **840**, 142967.
[252] Ur Rahman N, Capuano L, Cabeza S, Feinaeugle M, Garcia-Junceda A, de Rooij M B, Matthews D T A, Walmag G, Gibson I and Römer G R B E. 2019. Directed energy deposition and characterization of high-carbon high speed steels. *Addit. Manuf.* **30**, 100838.
[253] Khorasani M, Ghasemi A, Leary M, Cordova L, Sharabian E, Farabi E, Gibson I, Brandt M and Rolfe B. 2022. A comprehensive study on meltpool depth in laser-based powder bed fusion of Inconel 718. *Int. J. Adv. Manuf. Technol.* **120**, 2345–2362.
[254] Khorasani A, Gibson I, Veetil J K and Ghasemi A H. 2020. A review of technological improvements in laser-based powder bed fusion of metal printers. *Int. J. Adv. Manuf. Technol.* **108**, 191–209.
[255] Li W, Kishore M N, Zhang R Y, Bian N, Lu H B, Li Y Y, Qian D and Zhang X C. 2023. Comprehensive studies of SS316L/IN718 functionally gradient material fabricated with directed energy deposition: multi-physics & multi-materials modelling and experimental validation. *Addit. Manuf.* **61**, 103358.
[256] Wang J B, Zhou X L, Li J H, Zhu J L and Zhang M N. 2022. A comparative study of Cu–15Ni–8Sn alloy prepared by L-DED and L-PBF: microstructure and properties. *Mater. Sci. Eng. A* **840**, 142934.
[257] Yan L, Chen X Y, Li W, Newkirk J and Liou F. 2016. Direct laser deposition of Ti-6Al-4V from elemental powder blends. *Rapid Prototyp. J.* **22**, 810–816.
[258] Keicher D M and Miller W D. 1998. LENS^{TM} moves beyond RP to direct fabrication. *Met. Powder Rep.* **53**, 26–28.
[259] Eom Y S, Kim K T, Jung S H, Yu J H, Yang D Y, Choe J, Sim C Y and An S J. 2020. Investigation on interfacial microstructures of stainless steel/inconel bonded by directed energy deposition of alloy powders. *J. Korean Powder Metall. Inst.* **27**, 219–225.
[260] Chen M, Simonelli M, Van Petegem S, Tse Y Y, Chang C S T, Makowska M G, Sanchez D F and Moens-Van Swygenhoven H. 2023. A quantitative study of thermal cycling along the build direction of Ti-6Al-4V produced by laser powder bed fusion. *Mater. Des.* **225**, 111458.
[261] Myers A J, Quirarte G, Beuth J L and Malen J A. 2023. Two-color thermal imaging of the melt pool in powder-blown laser-directed energy deposition. *Addit. Manuf.* **78**, 103855.
[262] Costello S C A, Cunningham C R, Xu F D, Shokrani A, Dhokia V and Newman S T. 2023. The state-of-the-art of wire arc directed energy deposition (WA-DED) as an additive manufacturing process for large metallic component manufacture. *Int. J. Comput. Integr. Manuf.* **36**, 469–510.
[263] Karayagiz K et al. 2020. Finite interface dissipation phase field modeling of Ni–Nb under additive manufacturing conditions. *Acta Mater.* **185**, 320–339.
[264] Li S H, Kumar P, Chandra S and Ramamurty U. 2023. Directed energy deposition of metals: processing, microstructures, and mechanical properties. *Int. Mater. Rev.* **68**, 605–647.
[265] DebRoy T, Wei H L, Zuback J S, Mukherjee T, Elmer J W, Milewski J O, Beese A M, Wilson-Heid A, De A and Zhang W. 2018. Additive manufacturing of metallic components—process, structure and properties. *Prog. Mater. Sci.* **92**, 112–224.
[266] Xiao X Y, Roh B M and Hamilton C. 2022. Porosity management and control in powder bed fusion process through process-quality interactions. *CIRP J. Manuf. Sci. Technol.* **38**, 120–128.
[267] Chouhan A, Aggarwal A and Kumar A. 2020. A computational study of porosity formation mechanism, flow characteristics and solidification microstructure in the L-DED process. *Appl. Phys. A* **126**, 833.
[268] Khanna N, Salvi H, Karaş B, Fairoz I and Shokrani A. 2024. Cost modelling for powder bed fusion and directed energy deposition additive manufacturing. *J. Manuf. Mater. Process.* **8**, 142.
[269] Malej S, Godec M, Donik Č, Balazic M, Zettler R, Lienert T and Pambaguian L. 2023. Hybrid additive manufacturing of Ti6Al4V with powder-bed fusion and direct-energy deposition. *Mater. Sci. Eng. A* **878**, 145229.
[270] Piscopo G, Salmi A and Atzeni E. 2024. Investigation of dimensional and geometrical tolerances of laser powder directed energy deposition process. *Precis. Eng.* **85**, 217–225.
[271] Kannan R, Pierce D, Nayir S, Ahsan R U, Kim D, Unocic K A, Lee Y, Jadhav S, Karim A and Nandwana P. 2024. Wire directed energy deposition of steel-aluminum structures using cold metal transfer process. *J. Mater. Res. Technol.* **29**, 4537–4546.
[272] Mao S L, Yang B Q, Liu G, Liu G S and Zhang Z W. 2023. Temperature distribution and residual stress evolution at the interface of CuCrZr/316 L multi-material by laser powder bed fusion. *Opt. Laser Technol.* **163**, 109355.

[273] Liu L Q, Wang D, Deng G W, Yang Y Q, Chen J, Tang J R, Wang Y G, Liu Y, Yang X S and Zhang Y C. 2022. Interfacial characteristics and formation mechanisms of copper–steel multimaterial structures fabricated via laser powder bed fusion using different building strategies. *Chin. J. Mech. Eng. Addit. Manuf. Front.* **1**, 100045.
[274] Yang S W, Yoon J, Lee H and Shim D S. 2022. Defect of functionally graded material of inconel 718 and STS 316L fabricated by directed energy deposition and its effect on mechanical properties. *J. Mater. Res. Technol.* **17**, 478–497.
[275] Dzogbewu T C and de Beer D. 2023. Powder bed fusion of multimaterials. *J. Manuf. Mater. Process.* **7**, 15.
[276] Knapp W, Paillard P, Couturier L and Aubignat E. 2020. Joining steel and aluminum parts combing additive manufacturing process and laser welding. *Proc. SPIE* **112730F**.
[277] Bettencourt C J and Kouraytem N. 2025. Bonding SS316L and IN625 through laser powder bed fusion and directed energy deposition: a comparative tensile analysis. *npj Adv. Manuf.* **2**, 30.
[278] Wang M J, Zhao S X, Wang W J, Li Q and Luo G N. 2019. Preliminary results of CuCrZr/316L tube-to-tube junctions fabricated with rotary friction welding. *Fusion Eng. Des.* **148**, 111275.
[279] Zhang W Y, Lu X F, Coban A, Cervera M, Chiumenti M, Sasnauskas A, Huang C J, Yin S, Babu R P and Lupoi R. 2024. Powder sheet additive manufacturing of multi-material structures: experimental and computational characterizations. *Composites B* **272**, 111203.
[280] Shunmugesh K, Mathew S, Raphel A, Kumar R, Ramachandran T, Goyal A and Bhowmik A. 2025. Investigation of wire arc additive manufacturing of cylindrical components by using cold metal transfer arc welding process. *Sci. Rep.* **15**, 21599.
[281] Caiazzo F and Alfieri V. 2018. Laser-aided directed energy deposition of steel powder over flat surfaces and edges. *Materials* **11**, 435.
[282] Schwarz N, Lammers M, Hermsdorf J, Kaierle S, Ahlers H and Lachmayer R. 2023. Material efficient production of functionally graded materials using coaxial laser double-wire directed energy deposition. *Proc. SPIE* **124140E**.
[283] Müller M, Labisch C C, Gerdt L, Bach L, Riede M, Kaspar J, López E, Brueckner F, Zimmermann M and Leyens C. 2023. Multimaterial direct energy deposition: from three-dimensionally graded components to rapid alloy development for advanced materials. *J. Laser Appl.* **35**, 012006.
[284] Wei C, Zhang Z Z, Cheng D X, Sun Z, Zhu M H and Li L. 2021. An overview of laser-based multiple metallic material additive manufacturing: from macro- to micro-scales. *Int. J. Extrem. Manuf.* **3**, 012003.
[285] Hasanov S, Alkunte S, Rajeshirke M, Gupta A, Huseynov O, Fidan I, Alifui-Segbaya F and Rennie A. 2022. Review on additive manufacturing of multi-material parts: progress and challenges. *J. Manuf. Mater. Process.* **6**, 4.
[286] Kuang F, Zhou Q J, Pan Y, Yue L S, Yu A H and Lu X. 2025. Unveiling microstructural heterogeneity and strain redistribution mechanisms in hybrid-manufactured Ti6Al4V. *Mater. Sci. Eng. A* **927**, 148023.
[287] Tan C L, Wang D, Ma W Y and Zhou K S. 2021. Ultra-strong bond interface in additively manufactured iron-based multi-materials. *Mater. Sci. Eng. A* **802**, 140642.
[288] Yang Z N, Sun H, Shang S L, Liu Z K and Beese A M. 2024. Effect of heat treatment on functionally graded 304L stainless steel to Inconel 625 fabricated by directed energy deposition. *Materialia* **34**, 102067.
[289] Wei C, Zhao Z, Tang J G, Shen X F, Wang G W, Yang J L, Qin Y, Sun M Y and Yang Y. 2023. Effect of interface-layer process parameters on forming quality of 316L/CuSn10 bimetals fabricated via laser powder bed fusion. *Mater. Lett.* **336**, 133896.
[290] Kremer R, Etzkorn J, Palkowski H and Foadian F. 2022. Corrosion resistance of 316L/CuSn10 multi-material manufactured by powder bed fusion. *Materials* **15**, 8373.
[291] Yang X, Zou G S, Wang Z, He X Z, Zhang M N and Xu J Y. 2025. Interfacial characteristics and mechanical performance of IN718/CuSn10 fabricated by laser powder bed fusion. *Crystals* **15**, 344.
[292] Basak S, Baumers M, Holweg M, Hague R and Tuck C. 2022. Reducing production losses in additive manufacturing using overall equipment effectiveness. *Addit. Manuf.* **56**, 102904.
[293] Abdulmenova E V, Buyakova S P and Kulkov S N. 2022. Electrochemical hydrogenation of Ti–Ni powder mechanochemically alloyed with titanium. *Intermetallics* **151**, 107739.
[294] Patel M. 2025. A comprehensive review of functionally graded materials and their ballistic impact performance: current status and future challenges. *Next Mater.* **8**, 100704.
[295] Haribaskar R and Kumar T S. 2024. Defects in metal additive manufacturing: formation, process parameters, postprocessing, challenges, economic aspects, and future research directions. *3D Print. Addit. Manuf.* **11**, e1629–e1655.
[296] Tian X X, Zhao Z, Wang H B, Liu X M and Song X Y. 2023. Progresses on the additive manufacturing of functionally graded metallic materials. *J. Alloys Compd.* **960**, 170687.
[297] Chen H X, He Y X, Dash S S and Zou Y. 2024. Additive manufacturing of metals and alloys to achieve heterogeneous microstructures for exceptional mechanical properties. *Mater. Res. Lett.* **12**, 149–171.
[298] Gradl P R, Protz C, Fikes J, Ellis D, Evans L, Clark A, Miller S and Hudson T. 2020. Lightweight thrust chamber assemblies using multi-alloy additive manufacturing and composite overwrap. *In AIAA Propulsion and Energy 2020 Forum* (AIAA). 10.2514/6.2020-3787.
[299] Anil Kumar V, Gupta R K, Prasad M J N V and Narayana Murty S V S. 2021. Recent advances in processing of titanium alloys and titanium aluminides for space applications: a review. *J. Mater.Res.* **36**, 689–716.
[300] Gradl P, Tinker D C, Park A, Mireles O R, Garcia M, Wilkerson R and Mckinney C. 2022. Robust metal additive manufacturing process selection and development for aerospace components. *J. Mater. Eng. Perform.* **31**, 6013–6044.
[301] Seidel C. 2022. Multi-material metal parts by powder bed fusion: new application opportunities. (available at: www.metal-am.com/articles/multi-material-metal-parts-by-powder-bed-fusion-new-application-opportunities/).
[302] Hofmann D C, Kolodziejska J, Roberts S, Otis R, Dillon R P, Suh J O, Liu Z K and Borgonia J P. 2014. Compositionally graded metals: a new frontier of additive manufacturing. *J. Mater. Res.* **29**, 1899–1910.
[303] Zhai W G, Wang P, Ng F L, Zhou W, Nai S M L and Wei J. 2021. Hybrid manufacturing of γ-TiAl and Ti–6Al–4V bimetal component with enhanced strength using electron beam melting. *Composites B* **207**, 108587.
[304] Hofmann D C, Roberts S, Otis R, Kolodziejska J, Dillon R P, Suh J O, Shapiro A A, Liu Z K and Borgonia J P. 2014. Developing gradient metal alloys through radial deposition additive manufacturing. *Sci. Rep.* **4**, 5357.
[305] Eckes T K. Multi material 3D printing by Aerosint's selective powder deposition. (Aerosint). (available at: https://aerosint.com/heat-exchanger/).
[306] Li X. 2023. No title. *Case study_ Multi-material heat Sink Dev by Addit Manuf using Aerosint Technol Met AM* vol 9, 183–188.
[307] Chen L Y, Qin P, Zhang L N and Zhang L C. 2024. An overview of additively manufactured metal matrix composites: preparation, performance, and challenge. *Int. J. Extrem. Manuf.* **6**, 052006.

[308] Marques A, Cunha A, Gasik M, Carvalho O, Silva F S and Bartolomeu F. 2024. 3D multi-material laser powder bed fusion: ti6Al4V–CuNi2SiCr parts for aerospace applications. *Prog. Addit. Manuf.* **9**, 391–400.
[309] Wei C, Sun Z, Chen Q, Liu Z and Li L. 2019. Additive manufacturing of horizontal and 3D functionally graded 316L/Cu10Sn components via multiple material selective laser melting. *J. Manuf. Sci. Eng.* **141**, 081014.
[310] Netherlands Aerospace Centre. Netherlands Aerospace Centre (NLR) (available at: www.nlr.org/news/additive-manufacturing-of-two-metals-in-one-product/).
[311] U.S. Department of Defense. 2025. *Technology Readiness Assessment Guidebook* (Office of the Under Secretary of Defense for Research and Engineering, Washington).
[312] Ni J et al. 2019. Three-dimensional printing of metals for biomedical applications. *Mater. Today Bio* **3**, 100024.
[313] Han D and Lee H. 2020. Recent advances in multi-material additive manufacturing: methods and applications. *Curr. Opin. Chem. Eng.* **28**, 158–166.
[314] Bandyopadhyay A, Mitra I, Goodman S B, Kumar M and Bose S. 2023. Improving biocompatibility for next generation of metallic implants. *Prog. Mater. Sci.* **133**, 101053.
[315] Lima D D et al. 2017. Laser additive processing of a functionally graded internal fracture fixation plate. *Mater. Des.* **130**, 8–15.
[316] Wu Y C, Kuo C N, Shie M Y, Su Y L, Wei L J, Chen S Y and Huang J C. 2018. Structural design and mechanical response of gradient porous Ti-6Al-4V fabricated by electron beam additive manufacturing. *Mater. Des.* **158**, 256–265.
[317] Li Y et al. 2020. A review on functionally graded materials and structures via additive manufacturing: from multi-scale design to versatile functional properties. *Adv. Mater. Technol.* **5**, 1900981.
[318] Boldea I. 2017. Electric generators and motors: an overview. *CES Trans. Electr. Mach. Syst.* **1**, 3–14.
[319] 3D-printed electric motor made, developed utilizing a computational engineering model authored by LEAP 71. (available at: https://leap71.com/).
[320] Vedder C, Wollgarten S, Gradmann R, Stollenwerk J, Wissenbach K and Eberstein M. 2017. Laser-based functionalization of electronic multi-material-layers for embedded sensors. *J. Laser Appl.* **29**, 022603.
[321] Töppel T, Lausch H, Brand M, Hensel E, Arnold M and Rotsch C. 2018. Structural integration of sensors/actuators by laser beam melting for tailored smart components. *JOM* **70**, 321–327.
[322] Wei C, Sun Z, Huang Y H and Li L. 2018. Embedding anti-counterfeiting features in metallic components via multiple material additive manufacturing. *Addit. Manuf.* **24**, 1–12.
[323] Zhang M K, Yang Y Q, Wang D, Song C H and Chen J. 2019. Microstructure and mechanical properties of CuSn/18Ni300 bimetallic porous structures manufactured by selective laser melting. *Mater. Des.* **165**, 107583.
[324] Chopde R S, Gadewar S P, Khond M P and Rathod M J. 2017. Study on laser beam welding of copper and aluminum joint. *In 6th National Conference RDME 2017* (M.E.S. College of Engineering, Pune, India). pp 65–74.
[325] Mandolini M, Sartini M, Favi C and Germani M. 2023. An analytical cost model for laser-directed energy deposition (L-DED). *Advances on Mechanics, Design Engineering and Manufacturing IV* (eds Gerbino S, Lanzotti A, Martorelli M, Mirálbes Buil R, Rizzi C and Roucoules L) (Springer, Cham) pp 993–1004.